2024-05-14

Investigation of electrical properties of perovskite-type metal oxides

Selvakumar, Bhavadharini

UNIVERSITY OF CALGARY

Investigation of electrical properties of perovskite-type metal oxides

by

Bhavadharini Selvakumar

A THESIS

SUBMITTED TO THE FACULTY OF GRADUATE STUDIES

IN PARTIAL FULFILMENT OF THE REQUIREMENTS FOR THE

DEGREE OF MASTER OF SCIENCE

GRADUATE PROGRAM IN CHEMISTRY

CALGARY, ALBERTA

MAY, 2024

Abstract

Materials development has led to the growth of several technologies to reduce carbon footprints and to develop a sustainable environment. These strategies have led to the advancement of several renewable energy storage and conversion systems like fuel cells, batteries, solar cells, and capacitors that have been beneficial and environmentally benign. Moving towards clean energy includes using renewable energy sources and safe and sustainable materials for energy applications. However, the existing issues with materials development are the use of expensive and scarcely available raw materials, complex and multiple steps in material processing, and not exploring new family of materials.

This thesis addresses the use of studying the electrical properties of a family of materials known as perovskite-type oxides. The thesis focuses on the solid-state synthesis of transition metal doped double perovskite-type $Ba_2Ca_{0.67}Nb_{1.33-x}Cu_xO_{6-\delta}$ (x = 0, 0.05, 0.13 and 0.26) $Ba_2Ca_{0.67-x}Cu_xNb_{1.33}O_{6-\delta}$ (x = 0 and 0.13) and $BaY_{0.5}Nb_{0.5}O_3$ (BYN). The study includes the morphology of these materials, investigation of the electrical and dielectric properties of the above materials in different atmospheres, and their chemical stability in CO_2 and moisture containing environments. Among the compositions studied, $Ba_2Ca_{0.67}Nb_{1.2}Cu_{0.13}O_{6-\delta}$ shows the highest conductivity of 4.6 $\times 10^{-4}$ Scm^{-1} in dry air at 600 ˚C. The dielectric studies were also conducted among the investigated samples, the highest dielectric constant exhibited by $Ba_2Ca_{0.67}Nb_{1.2}Cu_{0.13}O_{6-\delta}$ (x = 0.13) was 587 and dielectric loss of 2 at 10^6 Hz at 500 ˚C in air. In general, $Ba_2Ca_{0.67}Nb_{1.2}Cu_{0.13}O_{6-\delta}$ (x = 0.13) shows highest dielectric constant values in the range of ~100 – 600 and lowest dielectric loss exhibited by $Ba_2Ca_{0.67}Nb_{1.28}Cu_{0.05}O_{6-\delta}$ (x = 0.05) was ~0.3 – 0.6 at 500 ˚C in various atmospheres.

The second part of the thesis focuses on the synthesis of multi-element doped $BaY_{0.5}Nb_{0.5}O_3$ (BYN) perovskite oxides, where alkaline earth and rare earth elements were doped in the A- and B-site of BYN. Synthesis and structural optimizations were also carried out to come up with pure single-phase materials. Out of all the compositions synthesized, $(Ba_{1-x}A'_x)(Y_{1/2}Nb_{1/2-y-z}M'_yM''_z)O_{3-\delta}$ (A' = Sr, Ca; M' = Mg and M'' = Ni) (x = 0, 0.5; y = 0, 0.1; z = 0, 0.05, 0.1), the PXRD pattern reveals the crystallization of only $BaY_{0.5}Nb_{0.5}O_3$ and $Ba_{0.5}Sr_{0.5}Y_{0.5}Nb_{0.4}Mg_{0.1}O_{3-\delta}$ in a cubic crystal system with $Pm\bar{3}m$ space group. Although, the crystal formation was successful for these compositions, several attempts were made to modify and optimize the synthesis and sintering conditions. The surface morphology of the pellet samples shows $BaY_{0.5}Nb_{0.5}O_3$ containing more pores and grain boundaries than that of $Ba_{0.5}Sr_{0.5}Y_{0.5}Nb_{0.4}Mg_{0.1}O_{3-\delta}$, emphasizing better particles formed in doped BYN. The chemical stability of these compositions in CO_2- and moisture-containing environment shows their potential to be used in devices for energy applications that are present in such operating conditions.

Acknowledgement

I would like to thank the following individuals, who have supported me throughout my research work and writing process.

My supervisor, Dr. Venkataraman Thangadurai, who provided me with invaluable support and feedback through the entire research project.

The members of my thesis committee, Dr. Michelle Dolgos, and Dr. George Shimizu, who took their valuable time to review and provide feedback on my work and experimental work. I would like to thank Dr. Todd Sutherland for accepting to evaluate my examination.

I am grateful to the Natural Sciences and Engineering Research Council of Canada (NSERC) for funding my research work and providing the resources to complete my MSc work.

All the previous and current group members who supported and gave me suggestions throughout my entire project, especially the SOFC team, Amanda Ndubuisi, Aroosa Javed, and Daniel Sikstorm for tolerating my non-stop questions and thankful to Thilini Boteju and Abinaya Sivakumaran for the sessions on research and much more. I would also like to thank past group members Dr. Alfred Samson, Dr. Sanoop Kammampata, Dr. Akhil M Abrahm, Bowen Chen, Afshana Bristi, and Anne Nguyen for their friendship and useful suggestions. They also helped me in communicating better and improved my presentation skills.

I am also thankful to Dr. Arthi Gopalakrishnan and Prathap Iyapazham Vaigunda Suba for carrying out characterization methods (PXRD and SEM) and for their insights round the clock. I would also like to thank other group members, Dr. Chengtian Zhou, Dr. Muhammed Shoaib, Dr. Vishnu Surendran, Dr. Monika Singh, Hirbod Salari, Temi, and Subhajit Sarkar for their help with

experiments, writing the thesis, and so many memories. Our discussions for solving assignments, coursework finals, 601/603 talks were filled with so much fun and knowledge sharing.

I would also like to acknowledge the current and past group members of Dr. Viola Birss group for being there in several situations. I would also like to thank the Department of Chemistry faculties for supporting me in my academic coursework to learn more and think better. I would also like to thank the teaching coordinators, Dr. Vivian Mozol, Dr. Erin Sullivan, and Dr. Carpenter.

My family, who provided me with emotional support throughout my academic journey, especially my younger brother and my friends back in India staying with me over internet, especially during my thesis writing.

My friends in Calgary who provided me with motivation and encouragement during my tough times and whenever I faced challenges.

Thank you all for your contributions, support, and encouragement.

Dedication

To Almighty, who stood by me the entire time and for his eternal love. To my parents, my younger brother, my cousins, and friends, for their love and support throughout my education.

Contents

List of tables

List of figures

List of symbols

Symbol	Definition	Unit
σ	Conductivity	S/cm
Ea	Activation energy	eV
ε_r	Relative dielectric permittivity	N/A
tanδ	Dielectric loss	N/A
Z’	Real impedance	Ω cm
Z”	Imaginary impedance	Ω cm
ω	Angular frequency	Hz
M”	Elastic modulus	Ω

List of abbreviations

LED	Light emitting diodes
SOFC	Solid oxide fuel cell
YSZ	Yttria stabilized zirconia
CGO	Gadolinium doped ceria
LSG	Strontium doped lanthanum gallates
MIEC	Mixed ionic and electronic conductors
pO_2	Oxygen partial pressure
ZrO_2	Zirconia
PXRD	Powder X-ray diffraction
SEM	Scanning electron microscope
FTIR	Fourier transform infrared
EIS	Electrochemical impedance spectroscopy
AC	Alternating current
GB	Grain boundary
BLM	Brick layer model
Au electrodes	Gold electrodes
s.g.	Space group
D_2O	Deuterium water
$V_O^{\bullet\bullet}$	Oxygen vacancy
O_O^{x}	Lattice oxygen
$h^{\bullet}$	Electronic hole

Chapter 1 Introduction

1.1 Motivation

The need for developing feasible materials for energy applications has led the research community to explore several metals and mixed metal oxides to find application among various energy storage and conversion devices[1] (**Figure 1.1**). The implementation and utilization of these technologies have undesirable impacts on environment, human race, and society. For example, electric vehicles require more materials than conventional combustion engines[2,3]; and LED bulbs are far more material-intensive than conventional incandescent bulbs[4].

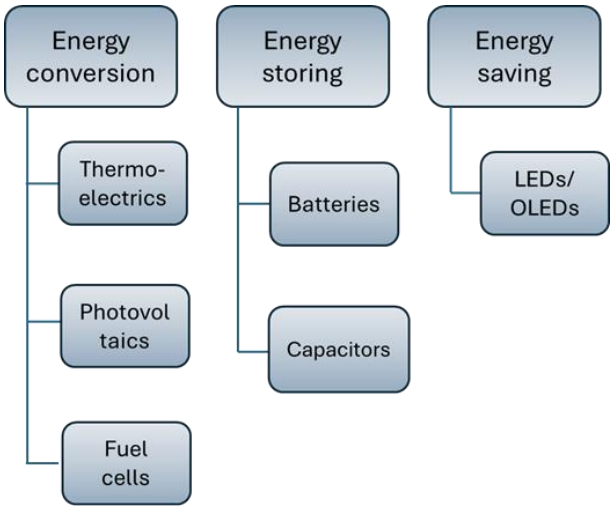

Figure 1.1 Flowchart of devices for energy applications, [LEDs: Light emitting diodes, OLEDs: Organic light emitting diodes].

These increased material mass corresponds to increase in material processing like extraction, refining, processing, and synthesis of raw materials; and can thereby increase the cost of maintenance[2,4]. Noble metals like Pt and Pd being used as catalysts have extraordinary catalytic properties, however, are limited due to cost and scarcity. Mixed metals, named as “alloys” has more complex processing, with 5 – 10 elements in equimolar ratio[5,6]. The situation becomes more

complicated when the materials are chemically toxic, which makes the recycling and recovering of these noble metals are difficult[7]. Some of the elements used for designing these devices are cobalt, nickel, lithium, neodymium, dysprosium, rhenium, tantalum, noble metals like platinum, palladium, are considered "critical" and "rare"[8]. This conceptual schematic is described in **Figure 1.2**.

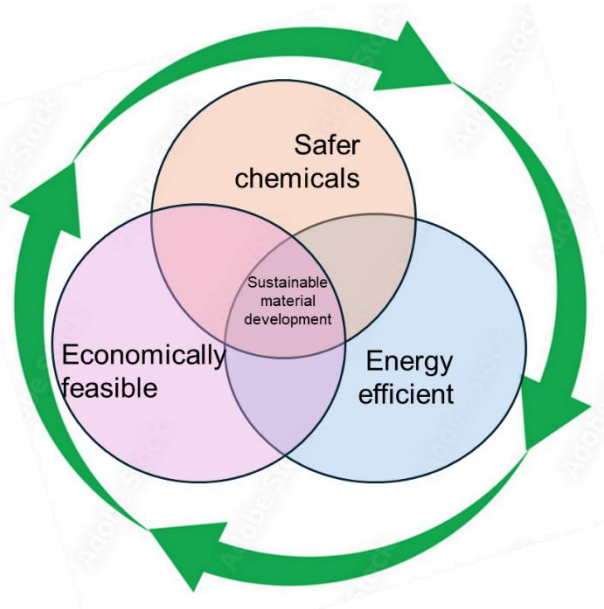

Figure 1.2 Schematic of the concept of sustainable development of materials. Incorporated with the concepts of use of safer chemicals, economically safe, and energy efficient.

Other than metals and mixed metals, some of the materials explored for energy application devices include, carbon materials, metal oxides, mixed metal oxides, composites, ceramics, and metal organic frameworks/zeolitic imidazolate frameworks (MOFs/ZIFs). Among these, transition-metal oxides like MnO_2, NiO, Fe_3O_4, Co_3O_4, Cr_2O_3, and TiO_2, are of great interest due to their multiple oxidation states, partially/ fully filled 3d orbitals for positive metallic cations, which makes them a good candidate for catalytic activity[9]. Simple combination of two or several low-cost transition-metal oxides (TMOs) forms spinel-like structures that leads to the formation of mixed transition-metal oxides (MTMOs) with the general formula $A_xB_{3-x}O_4$ (A and B = transition metals). These

MTMOs are emerging as promising catalysts for metal-ion batteries and electrochemical capacitors for energy storage applications. Their performance was typically 2–3 times higher than those of graphite/ carbon-based electrode materials. One of the properties of transition metals is their multiple oxidation states that makes them allure for electrocatalytic applications. However, some of the drawbacks that limits the commercialization of these oxides in energy technology is their complex processing methods and conditions, fabrication costs, long-term stability in operating conditions and corrosion resistance[10]. Fluorite oxides are widely used for various applications including solid conductors, and catalysts[11,12]. Some of the commonly used fluorite oxides are based on zirconia (ZrO_2) (doped with yttrium), hafnia (HfO_2), or ceria (CeO_2) and/ or various oxides like MgO, CaO, etc. This category of oxides possesses high oxygen conductivities, low thermal conduction, sturdiness, and high melting temperatures. Examples include rare earth doped zirconia and ceria are of great interest due to their high ionic or mixed conductivities and low thermal conductivity. However, their tendency to degrade over time is one of biggest challenges; for more mol % of yttrium-doped in zirconia leads to structural instability[13]. To overcome the limitations of fluorite-type oxides, another class perovskite oxides are being studied for their structural and physical properties that are interesting candidates for energy technologies, especially replacing the expensive noble metal catalysts. Some of the notable properties of perovskites are high crystalline quality, simple preparation technique, excellent catalytic properties, enhanced electrical and ionic conductivity which is useful in several electrochemical applications[14]. Some of the common applications of perovskite oxides are batteries, capacitors, solar cells, fuel cells and electrolysers, nuclear power plants, thermoelectric, carbon capture and storage, piezoelectric, turbines, and heat exchangers[15].

Apart from the perovskite oxides, there are several derived perovskite oxides - layered perovskite oxides that are still in the budding stages to be studied and explored for their structural and physical properties that are useful in several energy application devices. One of the major drawbacks of perovskite oxides is their tendency to react with CO_2 and moisture present in the atmosphere to form their respective carbonates and hydroxides which deteriorates the performance of these materials over prolonged period. Therefore, it is crucial to develop and explore doping strategies in these materials. Thus, the current thesis lays its focus on exploring perovskite-type oxides for understanding their structural and electrical properties without compromising their chemical stability.

1.2 Thesis objectives

The main objective of the current work is to explore the structural and chemical properties of perovskite-type oxide for its use as chemically stable proton-conducting electrolyte for SOFC applications. This thesis focuses on the following:

- Understanding the structural and electrical properties of transition metal-doped double perovskite-type $Ba_2Ca_{0.67}Nb_{1.33-x}Cu_xO_{6-\delta}$ (x = 0, 0.05, 0.13 and 0.26) oxides.
- Investigation of influence of B-site doping in the dielectric properties of double perovskite-type $Ba_2Ca_{0.67}Nb_{1.33-x}Cu_xO_{6-\delta}$ (x = 0, 0.05, 0.13 and 0.26) oxides.
- Investigation of synthesis conditions and structural characterization of ternary perovskite $Ba(M'_{1/2}M''_{1/2})O_3$ oxides.

1.3 Thesis organization

The present thesis is organized into 7 chapters. **Chapter 1** describes the introduction and motivation of the current thesis along with the structure and organization of the thesis chapters. **Chapter 2** provides the literature review on the discussed topics, which includes the current studies

on electrical properties of perovskite oxides. This chapter also addresses the performance of reported perovskite oxides and their challenges. **Chapter 3** outlines the material synthesis and characterization methods adopted for all samples.

Chapter 4 reports the synthesis and structural characterization of Cu-doped $Ba_2Ca_{0.67}Nb_{1.33}O_6$ perovskite oxides, along with the evaluation of their electrical properties in various atmospheres and their chemical stability in CO_2 and moisture containing environment. The dielectric properties of the above materials were also studied and presented in **Chapter 5**. This chapter outlines the variation of dielectric constant and dielectric loss at different atmospheres, the relation between electrical conductivity and dielectric constant is also drawn in this chapter.

Chapter 6 provides the structural and electrical properties of $(Ba_{1-x}A'_x)(Y_{1/2}Nb_{1/2-y-z}M'_yM''_z)O_{3-\delta}$ (A' = Sr, Ca; M' = Mg and M'' = Ni) (x = 0, 0.5; y = 0, 0.1; z = 0, 0.05, 0.1) simple perovskite oxide. Multiple elements were doped in the respective A- and B-sites of the parent sample $BaY_{0.5}Nb_{0.5}O_3$ simple perovskite oxides and their chemical stability were also evaluated.

Chapter 7 summarises the conclusion and future work of this thesis.

Chapter 2 Background

2.1 Perovskite and perovskite-type oxides: origin and progress

Perovskites are named for mineral made up of calcium, titanium, and oxygen with the formula $CaTiO_3$, first revealed by Russian mineralogist Gustav Rose in the Ural Mounts of Russia. The name Perovskite came after Lev Perovski who first discovered the mineral in 1839 and named after Russian mineralogist lev Perovski (1792-1856)[16]. ABX_3 is the general formula for all perovskite compounds, where A and B ions are cations and X is anion which forms octahedron with B-ions, which is mostly oxygen and sometimes halides, sulfides, and nitrides[17] (**Figure 2.1**).

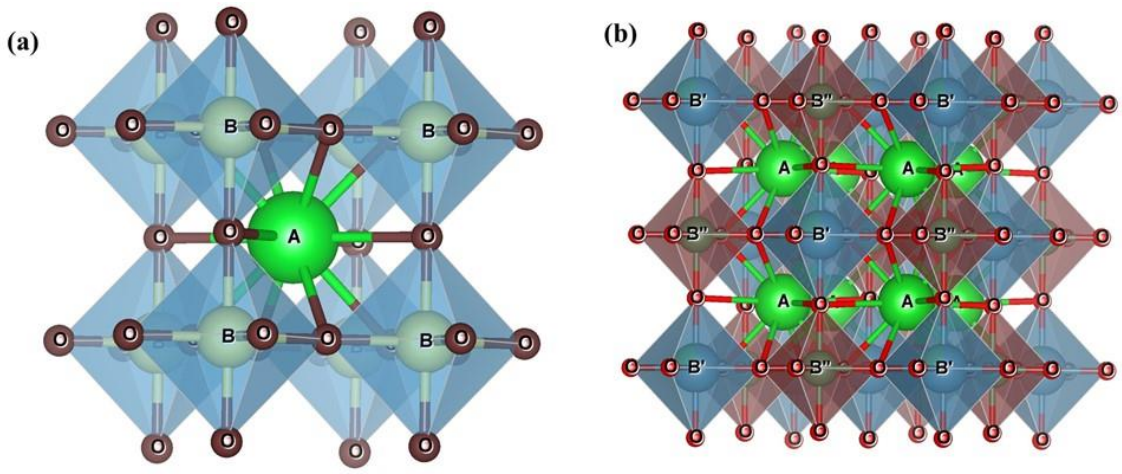

Figure 2.1 Crystal structure of an ideal (a) ABO_3 type simple perovskite, and (b) $A_2B'B''O_6$ type double perovskite.

The term perovskite or perovskite-type oxides are used interchangeably. Perovskite oxides are crucial functional materials with exceptional physical and chemical properties, which are widely studied in ferroelectric, piezoelectric, dielectric, energy conversion and storage applications, and so on[18]. Besides his contribution to lithium-ion batteries, Prof Goodenough's research insights have been in studying perovskite materials for their application in energy conversion and storage devices. Among various metal oxide catalysts, perovskite oxides with formula ABO_3 and $A_2BB'O_6$

with distinct combinations of A and B cations have gained attention due to their variable structural and different functional properties[19]. The diverse application of this class of oxides including superconductivity, ionic conduction characteristics, ferroelectricity and dielectric properties is due to their ability to accommodate almost all elements from the periodic table[20]. These perovskite oxides also have significant role in fields such as electrical ceramics, refractories, geophysics, material sciences, astrophysics, particle accelerators[21], fission-fusion reactors[20], heterogeneous catalysis[22], and environmental science[23]. The ability of perovskites to retain its structure even after accepting foreign atoms in their cationic sites (A-/B-)[24], enables the chemical modification of electrical, magnetic, and microstructural properties[23,25]. Several studies have expanded the application of these materials in sensors and actuators, microwave devices[26], piezoelectric devices[27], transducers, wireless communications[28], and capacitors[29].

2.1.1 Processing and applications

Synthesis method highly influences the structure and properties of perovskite oxides. Conventional solid-state reaction methods which involve high temperature synthesis methods are one of the commonly used routes for synthesising perovskite oxides[30]. One among the traditional route involved few drawbacks which is due to repeated grinding and calcining that leads to loss of certain volatile metal ions[31] and inhomogeneity of the resultant product. Some of these drawbacks are in the form of presence of defects that interferes with incorporation of chemical impurities during repeated grinding which makes the particles coarse that makes them unsuitable for coatings and thin films[32]. Over few years later, wet chemical methods were proposed to synthesize ceramic powders of pure quality, better grain characteristics with great surface area leading to better performance and properties. This route also solved the biggest drawback of solid-state reactions, which was to lower the sintering conditions. Some of these wet chemical methods includes co-

precipitation method[33] that involves the precipitation of the metal salts after the addition of a chemical reagent (e.g.: ammonia, ammonium oxalate, urea, and ammonium carbonate) that decreases the solubility limit. Another method, where the precursors are suspended in aqueous solutions at high temperature and pressure, is the hydrothermal method[34]. However, due to the instability of the precursor system it is difficult to control the chemical composition of complex oxides which limits the application of this synthesis method. In solid-state reactions, perovskites are synthesized by using carbonates, nitrates, and oxides of the A- and B-site metal ions in certain proportion, and by regulating the temperature and grinding conditions[35,36]. All the precursors at exact ratios are grinded in ball mill jars using isopropanol/acetone and are treated to high temperatures to obtain the final perovskite powders[37]. Researchers have figured out yet another synthetic synthesis method in solid state chemistry, which offers energy and time savings compared to other synthesis method. The usage of microwave irradiation is an alternative heat source for perovskite synthesis[38]. There are two methods of microwave synthesis: microwave-assisted hydrothermal synthesis and solid-state microwave. The second method involves the synthesis of simple perovskites, whereas the first method that involves the combination of microwave with other methods like combustion, hydrothermal or sol-gel has enhanced the stoichiometric control of complex phases[39]. This combination method results in unique morphology and metastable phases. The speed and simplicity of this method has become attractive for the synthesis of lead-containing perovskites as it reduces the loss of lead[38]. Few other improved synthesis methods also include low temperature solution combustion method, gas phase preparations, pechini method, laser ablation and wet chemical method.

Application of perovskites and perovskite-type oxides

Perovskite oxides have wide applications due to its stable structure, varied properties and has large number of compounds[21]. In that aspect, inorganic perovskite oxides have attractive applications as nanomaterials in catalysis. It is considered that the activity of these materials proves to be much better than that of transition metals and precious metal oxides. The catalytic activity of perovskite oxides has proven to be a great substitute for the traditional metal and metal oxide catalysts. Their surface and morphological properties, suitable solid-surface and chemical manufacturing makes them a better catalyst for various chemical reactions like hydrogen evolution, reduction reactions, and oxygen evolution[40,41]. Recent studies have shown the efficient use of these materials in electrochemical sensing of alcohols, acetone, glucose, amino acids, H_2O_2 due to their excellent sensitivity and selectivity, reproducibility, unique long-term stability, and anti-interference ability[42]. The suitable electronic structure of perovskite oxides makes them an excellent candidate for gas sensing applications[43]. Other perovskite materials that consist of cobaltite's, titanates, and ferrites are being used as gas sensors for detecting CO, NO_2, methanol and ethanol, and hydrocarbons[44]. The enzymes are being used in glucose sensors are limited by their instability and performance due to temperature, humidity, poisonous chemicals from external environment. Inorganic perovskite oxides are known for their stable, sensitive, simple, and selective nature for application as non-enzymatic glucose sensors[45]. Considering the electrical conductance property of perovskites, they are extensively used as electrocatalytic materials in energy conversion devices like fuel cells[20,33] and solar cells. It is interesting to know that solar cells these days are built using silicon, lead based halides which are expensive and harmful to the environment thereby making the installation and utilization of solar cells difficult in various fields[46]. Looking at the use of perovskites in solar cells, which possesses suitable band gap, excellent stability, longer diffusion

lengths, higher charge-carrier mobility and transport, lower processing temperature and easier processing steps, makes them an excellent candidate for being used in solar cells[47]. Depending on the type of perovskite oxides and their distinct properties makes them allure for several applications including thin film capacitors, non-volatile memory films, photo-electrochemical cells, recorders, spintronics devices, laser applications, protection from infra-red radiation, sensors, actuators and transducers, drug delivery, ultrasonic and underwater devices (**Table 2.1**).

Table 2.1 Summary of list of important properties, applications, and their respective examples of perovskite oxides[48].

Properties	**Applications**	**Examples**
Dielectrics	Ceramic capacitors, resistors, microwave devices, barrier layer capacitors	(Sr/Ba)TiO_3
Proton conduction	Electrolyte in protonic solid fuel cells, hydrogen sensors	Doped-$BaCeO_3$, $BaZrO_3$
Oxide-ion conduction	Electrolyte in solid oxide fuel cells	Doped-$LaGaO_3$, $BaIn_2O_5$
Mixed conduction	Cathode in solid fuel cells	(La,Sr)BO_3 (B = Mn, Fe, Co)
Optical	Gas and chemical sensors, thermal electric batteries	$K(Ta_{0.65}Nb_{0.35})O_3$, $BaTiO_3$, $SrTiO_3$
Piezoelectricity/ Ferroelectricity	Transducers and actuators, ferroelectric memories. Optoelectronic devices	Pb(Zr,Ti)O_3, $(K_{0.5}Na_{0.5})NbO_3$, $Na_{0.5}Bi_{0.5}TiO_3$
Magnetic/ Ferromagnetism	Electrode material in epitaxial ferroelectric thin films, magnetic field detectors	(La,A)MnO_3 (A = Ca, Sr, Ba), $BiFeO_3$
Catalytic activity	Oxidation of hydrocarbons, photo assisted water splitting, oxygen separation/permeation membrane	(La,Sr)BO_3 (B = Mn, Fe, Co), $SrTiO_3$

2.1.2 Structural aspects of perovskites and perovskite-type oxides

A typical perovskite structure is as cubic unit cell (**Figure 2.1(a)**) with the general structure (ABO_3) where the 12-fold coordinated A-site cations reside in the centre, whereas 6-fold coordinated B-site cations reside on the corners of the unit cell, and the oxygen is placed at the middle of the edges of the BO_6 octahedra. A-site cations are usually with smaller ionic radii which can fit alkaline, alkaline-earth and rare-earth metals and the B-site cations are bigger size transition metals[49]. These different compositions alter their crystal and electronic structure and accommodate multiple cations in their A- and/or B-site of the structure paving way for ordering effects and non-stoichiometry that opens to various physical properties. The structure of perovskites can be varied based on the ionic radii of the cations; this can be expressed through Goldschmidt tolerance factor (t) in 1926[50]:

$$t = \frac{r_A + r_O}{\sqrt{2}(r_B + r_O)} \tag{2.1}$$

where, r_A, r_B, and r_O are ionic radii of A-, B-site cations and anion, respectively. Usually, value of t lies in the range of 0.9 – 1.0 for cubic perovskite structure. If t > 1, hexagonal type structure the symmetry is greater than that of cubic structure. When, t is in the range of 0.71 – 0.9, the structure distorts to octahedral polyhedron whose symmetry is smaller than cubic structure[51–53] (**Table 2.2**).

Table 2.2 Summary of crystal structure of perovskite and perovskite-type oxides based on Goldschmidt's tolerance factor[54].

Goldschmidt tolerance factor (t)	**Crystal structure**	**Example**
>1	Hexagonal or tetragonal	$BaNiO_3$
0.9 - 1	Cubic	$SrTiO_3$
0.71 – 0.9	Orthorhombic or rhombohedral	$GdFeO_3$

The perovskites structure generally offers total charge of A and B cations as +6, A and B cation valency is usually 2+ and 4+ respectively; and/ or it can be 3+ on each cation. However, structural constraints are caused by difference in ionic radii of B-site ions, and the structure becomes distorted due to formation of oxygen/ cationic vacancies. This distortion in perovskites can influence the properties of the materials by partial substitution/ replacement of A- and/or B-site cations ($A_{1-x}A'_xBO_3$; $AB_{1-x}B'_xO_3$; and $A_{1-x}A'_xB_{1-y}B'_yO_3$). The partial substitution of A-site cation (or B-site cation) with acceptor cations results in the formation of oxygen vacancies and increases ionic conductivity than that of undoped perovskite materials. There are some cases where the charge- and ionic radii difference of the host and substituted ions tends to induce ordering of ions which leads to the formation of ordered perovskites. The structure is generally represented as a 3-D network of BO_6 octahedra, and the distortion of the structure is usually indicated by the proportion of ionic size of A- and B-site cations. Perovskite exhibits two structural distortions; one is the tilting of the BO_6 octahedral which relates to the displacive phase transition, and the other is the off-centering of B ion in the octahedral which refers to phase transition that is order-disorder[55].

Flexibility of these materials to accommodate broad range of cations has given rise to diverse perovskite-based compositions with varied physical properties. The perovskite oxides are classified broadly based on the anion (oxygen and halides) depicted in the flowchart[18]:

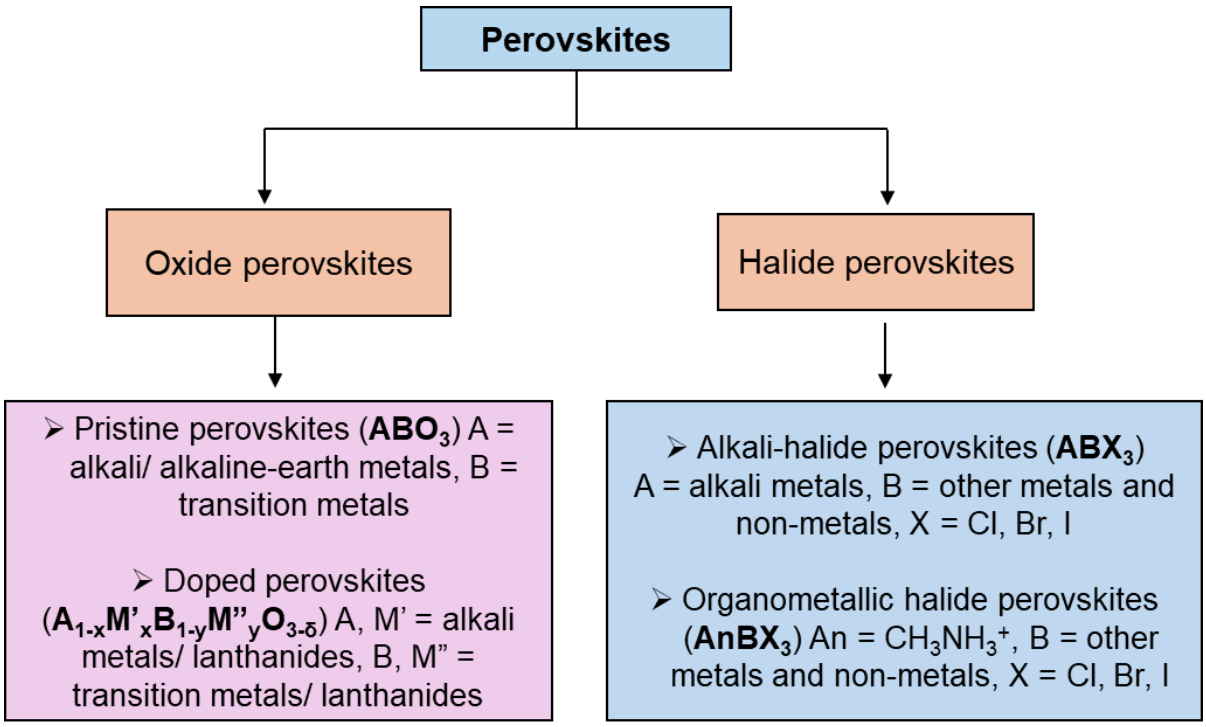

Figure 2.2 Classification of perovskites.

In ternary ABO_3-type oxides the valence variation of A-site causes buckling of $(AO_3)^{4-}$ layers which leads to distortion of B-site octahedra. To compensate for the distortion, B-site cations are usually transition metal elements due to their multi-valency and the *3d* and *4d* electron configurations.

Compounds of complex perovskite $(AB'_xB"_y)O_3$ can be divided into 4 subgroups:

(a) Compounds with oxygen deficient phases, $A(B'_xB"_y)\ O_{3-z}$.

(b) Equal amounts of B-site elements, $A(B'_{0.5}B"_{0.5})O_3$.

(c) Contains high valence element are twice in value than the lower valence element, $A(B'_{0.33}B''_{0.67})O_3$ and/or $A(B'_{0.67}B''_{0.33})O_3$[30].

Recent research on perovskite materials is extended to double perovskites and derived perovskites like Ruddlesden-Popper (layered oxides). Double perovskite oxides with general formula $A_2B_2O_6$ are generally achieved by replacing ions in the A- and B-site; this substitution of multiple ions at each sites induces more oxygen vacancies and makes these perovskites an excellent solid electrolyte for fuel cells. The B-O-B angle and B-O bond length influences the structural properties of the double perovskites, with preferred angle of 180˚ and shorted bond length is tuned by substituting more than one B-site ions. The crystal and functional properties of these perovskites are controlled by the synthesis methods[14].

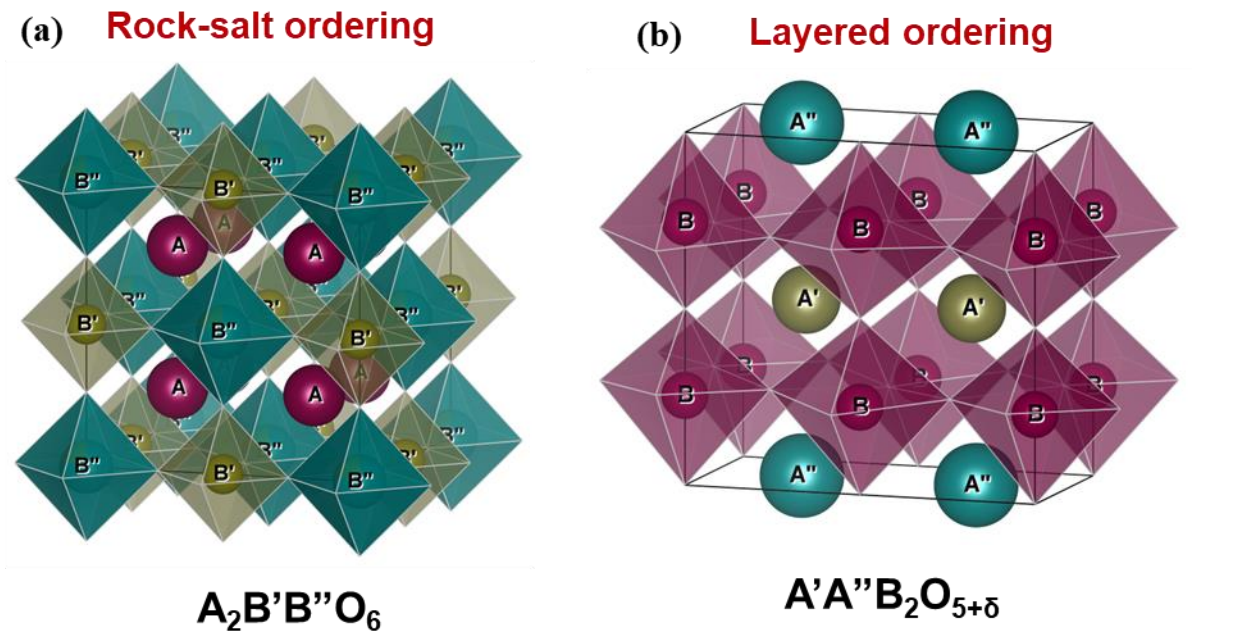

Figure 2.3 Crystal structure of rock salt ordering (B-site) and layered ordering (A-site).

The presence of multiple ions in A- and B-sites leads to cation ordering, which can vary upon different ways in which they order. In majority of double perovskites, the B and B' cations are

ordered in rock-salt type structure. In general, when the oxidation states of B and B' is less than two, a disordered arrangement (e.g. La_2CrFeO_6), whereas, when the difference is more than two favours ordered arrangement (e.g. Sr_2NiWO_6), and when the difference is exactly two, disordered (e.g. Sr_2FeRuO_6), partially ordered (e.g. Sr_2AlTaO_6), or fully ordered (e.g. Sr_2YNbO_6) arrangements can be formed, based on the size differences in ion size and/or bonding preference of the B and B' cations[56,57]. There are three different patterns of ordering for either A- or B-site cations. The symmetric one is rock salt ordering with 0D because of the pattern of B and B' (or A and A') cations equivalent to the anion and cation in rock salt structure. Columnar ordering corresponds to 1D ordering and layered ordering relates to 2D connectivity of the octahedrons. A-site cation ordering is less common than B-site cation ordering, which is because of the difference in size and oxidation state of B-site ions. A-site cation ordering favours layered ordering which is stabilised by large A/A' size mismatch with anion vacancies, and B-site cations favours rock-salt ordered structure stabilised by the size and oxidation state difference between the B/B' cations[58] (**Figure 2.3**).

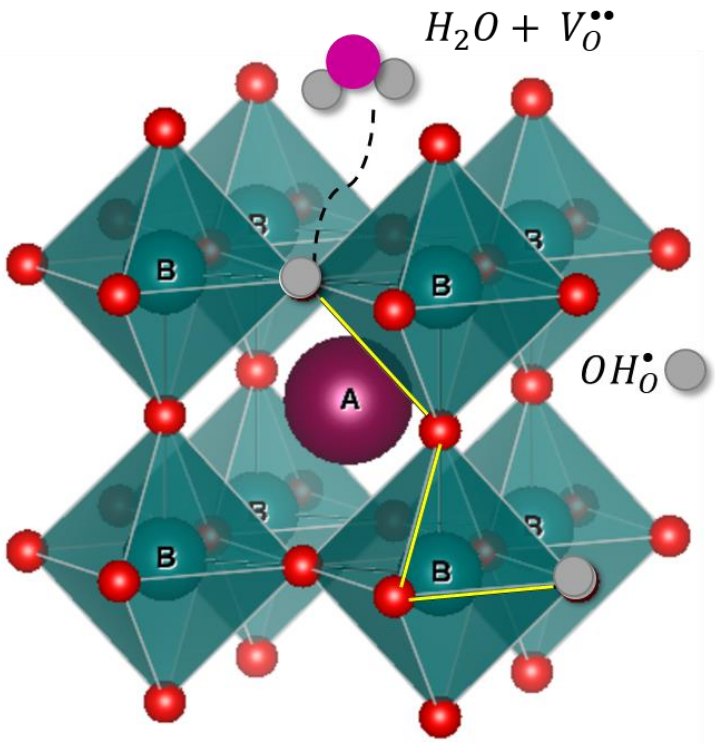

Figure 2.4 Schematic illustration of vacancy formation and migration of vacancies in perovskite oxide.

2.2 Electrical conductivity of perovskite and perovskite-type oxides

In the current thesis, the electrical properties of certain class of perovskite materials are being investigated to understand their electrical conductivity in different ambience. Studying the electrical properties of perovskites helps in understanding the type of charge carriers that contributes to the conductivity and their applications in devices for energy storage and conversion. Apart from determining the ordering of these double perovskites, the ionic size difference of the cations in these double perovskites, determines the formation of anionic vacancies. While the electrical conductivity is related to the valence change of B-site cation, ionic conductivity is related to the oxygen vacancy migration/ transport (**Figure 2.4**). The vacancy defects present in these oxides favour oxide ion conductivity and mixed ionic and electronic conductivity. Point defects in

perovskite oxides can be expressed using the Kroger-Vink notation. The possible occupants at A-site can be A_A^x, V_A''', and M_A', while the ones in the B-site are B_B^x, B_B', V_B''' and $B_B^\bullet$. Where B_B^x, represents majority of B cations with valence of 3+, B_B' represent B cations with 2+ valency, and $B_B^\bullet$ represents B cations with 4+ valency. The oxygen site usually has two occupants, $V_O^{\bullet\bullet}$ and V_O^x. The formation of oxygen vacancies in perovskite oxides is by substituting B-cations with different oxidation states. Under reducing conditions (low oxygen partial pressure), the material loses oxygen and leads to the formation of oxygen vacancy ($V_O^{\bullet\bullet}$) and electrons (e') given by the following equation,

$$O_O^x = \frac{1}{2}O_2(g) + V_O^{\bullet\bullet} + 2e' \quad (2.2)$$

And under oxidising conditions (high oxygen partial pressure), the oxygen vacancy picks up oxygen from the environment which results in the formation of oxide ions (O_O^x) and holes ($h^\bullet$),

$$\frac{1}{2}O_2(g) + V_O^{\bullet\bullet} = O_O^x + 2h^\bullet \quad (2.3)$$

However, for proton conductivity, when the material is exposed to humidity, the oxygen vacancy in the crystal structure picks up the water molecule and forms a proton attached to an oxide ion ($OH_O^\bullet$) that is the charge carrier which contributes towards proton conductivity[59,60],

$$H_2O + V_O^{\bullet\bullet} + O_O^x = 2OH_O^\bullet \quad (2.4)$$

Oxide-ion conductors

Oxide-ion conductors have been widely used in fuel cells, oxygen sensors, oxygen pumps and oxygen-permeable membrane catalysts[61–63]. Most of these applications require a high temperature to achieve high oxygen flux for efficient operation. Perovskite is one class of material exhibiting

high oxide-ion conduction[63]. To be an oxide-ion conductor, the essential feature is the presence of oxygen vacancies. When a cation A or B in a perovskite-type oxide ABO_3 is partially replaced by a cation of lower valency, it sometimes gives rise to a substantial number of oxide ion vacancies (equation 2.2) in the lattice to maintain electrical neutrality of the crystal[64]. In such crystals, appreciable oxide-ion conduction may be expected at elevated temperatures since oxide ions can migrate through the crystal lattice with the assistance of the oxide-ion vacancies like the case of stabilized zirconia. Based on this idea, several authors have investigated the ionic conduction in various kinds of perovskite-type oxide solid solutions which are heavily doped by some aliovalent cations to make several oxygen vacancies[65,66]. These oxygen vacancies supply the equivalent sites, allowing the oxygen ions to migrate, thus facilitating ionic conductivity. At a high temperature, due to the lattice vibrations and chemical potential gradient, oxide ions move to the nearby oxygen vacancies. Further, the vacancy created by the movement of one oxide ion will be occupied by another neighbouring oxide ion. This movement is a result of thermally activated hopping of the oxide ions, moving from one crystal lattice site to a neighbouring lattice site, with a superimposed drift in the direction of the electric field. Some of the best-known examples of oxide ion conductivity are yttria-stabilized zirconia (YSZ), gadolinia-doped ceria (CGO) with fluorite oxide type structure and strontium-doped lanthanum gallates (LSG) with perovskite-type structure. The conductivities of oxide-ion conductors like fluorite-type and perovskite-type oxide are depicted in **Figure 2.5** at temperatures between 400 – 750 ˚C, in ambient air. Several other oxide ion conductors like calcium-titanate-based ceramics[66] with orthorhombic crystal structure and shows low ionic conductivity at high temperature than that of fluorite-type oxides. However, 25% Al substitution of Ti in $CaTiO_3$, changes its crystal structure from orthorhombic to cubic and improves the conductivity.

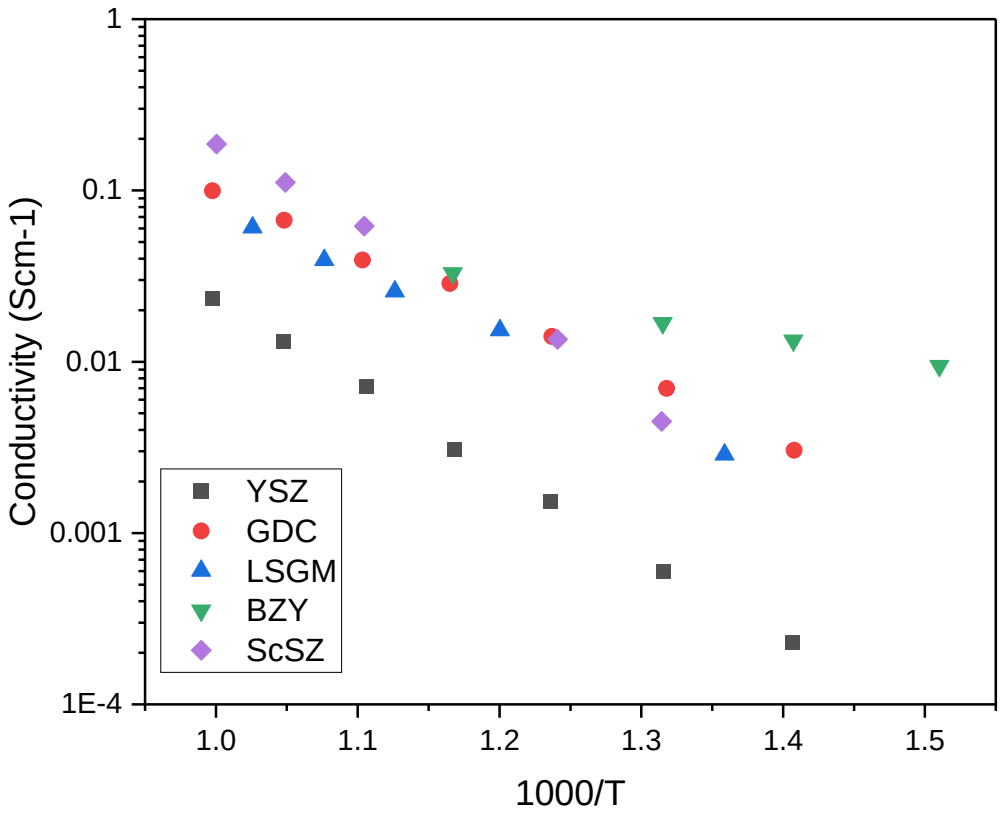

Figure 2.5 Conductivities vs temperature of various oxide ion conducting fluorite-type and perovskite oxides (in air); 8 mol% YSZ[67], 8 mol% scandia stabilized zirconia (ScSZ)[68], GDC[67], LSGM[69], and BZY[70].

In terms of activation energy, mixed conducting materials exhibit lower activation energy (~0.25 eV), whereas oxide-ion conductivity requires higher activation energy (~0.6 – 1.2 eV)[71]. For high oxide ion conductivity, some rules for ionic charge and radii of the cations are given as follows: B-site cations should be large (Ni > Co > Fe > Mn > Cr) and with possibly lowest oxidation state (2+ > 3+ > 4+), which facilitates weak bonding of the oxide ions; similarly, A-site ions should be smaller (Ca < Sr < Ba; Ce < Pr < Gd < La) which gives more space available for oxygen mobility and high electrostatic attraction of oxide ions.

Proton conductors

In 1980s, Iwahara *et al*., first reported proton conductivity in perovskite oxides like, barium and strontium cerates ($BaCeO_3$ and $SrCeO_3$) systems with high proton conduction of 10^{-2} – 10^{-3} S/cm, 600 – 1000 ˚C)[72]. For almost a decade since then, the same group conducted several studies on proton conduction in several zirconate and cerate perovskites and have reported the structure, formation of protons, and their conduction mechanism (**Figure 2.7**). A typical example of one such proton conducting perovskite oxide is $SrCe_{0.95}Yb_{0.05}O_{3-\delta}$, which is solid solution where, 5% of Ce is replaced by Yb and exhibits proton conduction in hydrogen-containing atmosphere at high temperatures. Other perovskite-type oxides where trivalent ions are partially substituted for Ce in $BaCeO_3$ or $SrCeO_3$[72,73], with general formula $SrCe_{1-x}M_xO_{3-\delta}$ or $BaCe_{1-x}M_xO_{3-\delta}$ ($x < 0.2$) where M is a rare earth element. The proton conductivity is in the range of 10^{-2} – 10^{-3} Scm^{-1} at 600 – 1000 ˚C. The proton conductivity experiments are carried out by transport experiments under hydrogen- or water vapour- containing atmosphere at elevated temperatures. After the discovery of $SrCeO_3$-based proton conductors, other perovskite-type oxides $KTaO_3$-[74] were reported to have proton conduction at high temperatures, but comparatively lower than that of other cerate-based perovskites. Other doped zirconates $CaZrO_3$, $SrZrO_3$, or $BaZrO_3$[75,76] also exhibited low proton conductivities compared to other doped cerates. Among all the cerates and zirconates, $BaCeO_3$-based perovskites shows highest proton conductivity, however, the oxide ion conduction starts to appear as the temperature increases[77,78]. Although, zirconates have poor conductivity compared to that of cerates, the former has better chemical and mechanical properties. Later years, Nowick *et al*., started exploring a new proton conductor[79] based on complex perovskites $A_2(B'B'')O_6$ (A ions have 2+ charge and B' has 3+ and B'' has 5+ charge) and $A_3(B'B''_2)O_9$ (A ions have 2+ charge and B' has 2+ and B'' has 5+ charge).

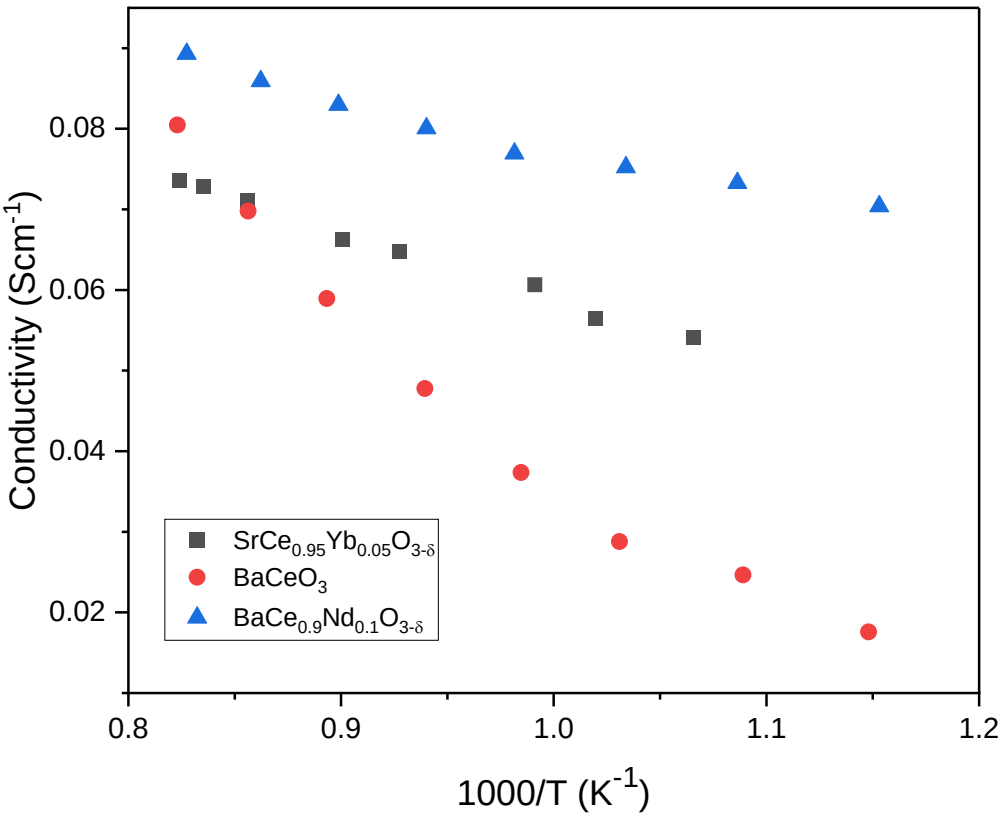

Figure 2.6 Conductivity vs temperature of doped cerates (Ba and Sr analogues) in hydrogen gas atmosphere[72].

In early 1990s, $A_3(B'B''_2)O_9$ type perovskites, where A and B' are alkaline-earth metals and B'' is niobium (Nb) and tantalum (Ta), were found to have interesting mixed proton and oxide-ion conductivity[80]. In contrast to simple perovskites, the properties of complex perovskite oxides are related to microstructural features like ordering of B-site ions. Some of the complex double perovskites, i.e., $Sr_2Sc_{1+x}Nb_{1-x}O_{6-\delta}$ and $Ba_3Ca_{1+x}Nb_{2-x}O_{9-\delta}$ can absorb protons to a certain concentration when off-stoichiometric, which is described by the reaction (2.5) and eventually becomes proton conductors[81]. Their proton conductivities were found to be superior to that of Cerates based perovskites described earlier.

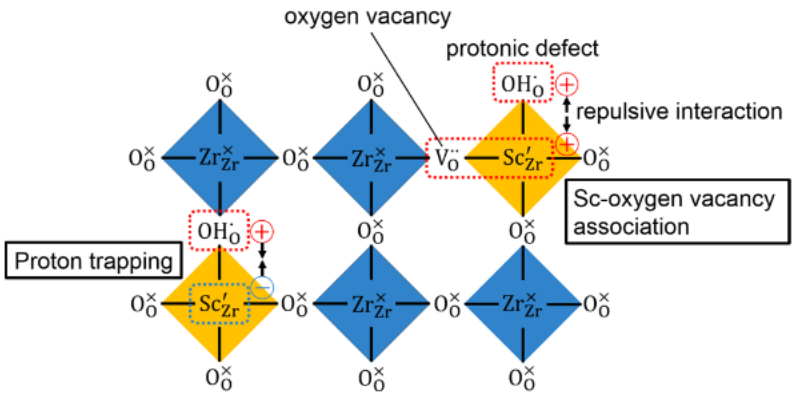

Figure 2.7 Schematic view of the interaction between oxygen vacancies and protonic defects around the acceptor[82].

Mixed ionic and electronic conductors

Another class of materials are which conducts mixture of ionic and electronic species which promotes electrical conductivity. There are materials where the charge transport is mainly due to ionic species, with negligible electronic conduction, which are termed as ionic conductors (oxide ion conductors). Whereas there are electronic semiconductors which influences the charge/vacancy concentrations and the microstructure of the materials. Mixed ionic and electronic conductors (MIECs) have both ionic and electronic conductivity, even though in small amounts, and exhibits their conductivity at finite temperatures, which is in the range of 10^{-4} – 10^{-3} S/cm[83]. MIECs can be generated by several methods, one of which includes incorporation of electronic carriers (like electrons and/or holes) into pure ionic conductors. Although, thermal activation also helps in development of electron-hole pairs, doping and stoichiometry control helps in enhancing electronic conductivity like that of semiconductors. Several MIECs have been reported so far, like Ag_2S and Ag_2Se, which contains silver cations (Ag^+) and electronic carriers (electrons, holes) that can simultaneously migrate[84,85]. Their conductivity can be modified by controlling the

stoichiometry of silver and the chalcogen. An example of undoped semiconductor which is an MIEC is stoichiometric CeO_2 which is an insulator for electrons (or holes) and ions. Yttria or calcia stabilized zirconia (YSZ or CSZ) are like the CaO doped CeO_2, when the stoichiometry varies, $Zr_{1-x}Y_xO_{2-\delta}$ is a good oxide ion conductor at ~1000 ˚C[86,87]. The excess oxygen enters the vacant site and accepts two electrons and forms holes (equation 2.4). Perovskite-type oxides are also being employed as MIECs in several energy application systems. Among them, $(La,Sr)(Co,Fe)O_{3-\delta}$ referred to as LSCF, is a well-known MIEC at elevated temperatures (> 700 ˚C)[88]. In this material, the Sr on the La site works as an acceptor which introduces electronic holes and oxygen vacancies for oxide-ion migration, which varies at different oxygen partial pressures (pO_2). In case of LSCF, higher the pO_2, higher the electronic conductivity. It was found that Fe-doped $CaTiO_3$ ceramics are oxide-ion and electron hole mixed conductors and are stable under reducing atmosphere at high temperatures[65]. For instance, oxide ion conductivity of $CaTi_{0.7}Fe_{0.3}O_{3-\delta}$ is as high as that of calcia-stabilized zirconia but its electronic conductivity in air is twice higher than that of oxide ions at 1000 ˚C. Even though, few doped $BaCeO_3$-based ceramics shows pure proton conduction in hydrogen atmosphere at high temperature, they exhibit mixed ionic conductors of proton and oxide-ion under fuel cell conditions[89].

Double perovskite-type $Ba_2Ca_{2/3}Nb_{4/3}O_6$ oxides

In this thesis, transition metal doped perovskite-type $Ba_2Ca_{0.67}Nb_{1.33}O_6$ (BCN) was studied for their structural and electrical properties, and their chemical stability. Structural aspects of $A_3(B'B''_2)O_9$ perovskites varies from that of simple ABO_3 perovskites due to the presence of mixture of pentavalent and divalent ions in the B-site. Due to the large valence difference, the B-site ions are usually ordered; the ratio of these host cations can be varied to create effective negative charges that produces structural defects in the system.

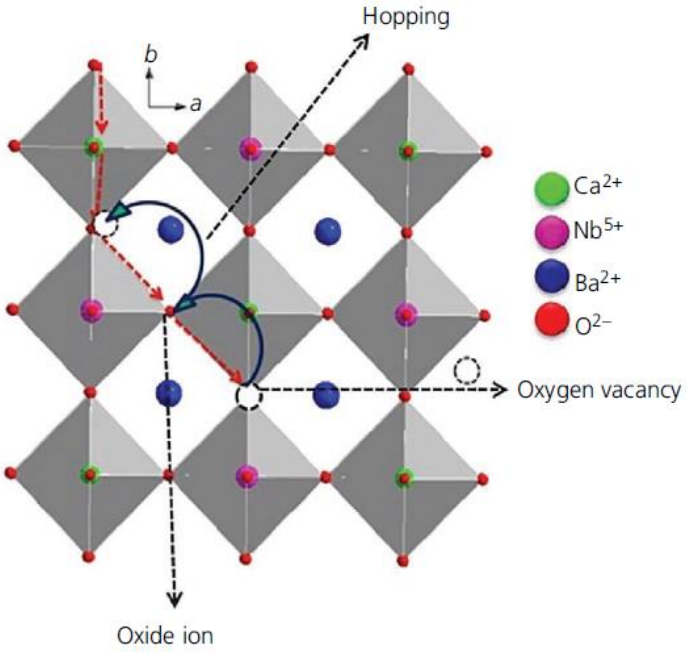

Figure 2.8 Oxide ion conduction in non-stoichiometric double perovskite-type $Ba_3Ca_{1.18}Nb_{1.82}O_{9-\delta}$ (BCN)[87].

Among different types of proton-conducting ceramics, cerates like $BaCeO_3$ oxides were found to exhibit highest proton conductivity of 1.0×10^{-2} S/cm[90,91]. However, the disadvantage with cerates is that they are instable in carbon dioxide or humid atmospheres. To overcome the instability issue, Ce was partially replaced with Zr ions which proved to improve their stability, however, their total conductivity was lowered[92,93]. The proton uptake in $A_3Ca_{1+x}Nb_{2-x}O_{9-\delta}$ (A = Ba, Sr) has proven to be more pronounced than that in Ce-based perovskites[94–96]. In $A_3(B'B''_2)O_9$, two types of B-site ordering have been observed, 1:1 and 1:2 ordering. The unit cell in 1:2 ordered structure consists of B ions distributed on consecutive (111) plane in the sequence of -B''-B'-B''- with trigonal symmetry. Whereas, in 1:1 ordered structure, B ions are in alternate (111) planes like that of NaCl-type cubic symmetry. The non-stoichiometric $Ba_3Zn_{1+x}Nb_{2-x}O_{9-\delta}$ observed that the compound tends to promote 1:1 ordering when it is Zn-rich ($x > 0$) and is 1:2 ordering when $x < 0$[97]. Also, it must be noted that $Ba_3ZnTa_2O_9$, has the 1:2 ordered trigonal structure is deformed by addition of a small amount of Zr^{4+} ions which replaces Ta^{5+} ions[98]. These results shows that type of structural

ordering highly depends on the chemical modifications of the B-site like dopants and synthesis conditions. However, when the compound $A_3B'B''_2O_9$ is initially 1:2 ordered will become 1:1 ordering when the ratio of B'/B" increases and this transition is still under investigation. It is interesting to note that $A_2(Ca_{1+x}Nb_{2-x})O_{9-\delta}$ (A = alkaline earth metals) exhibits high oxide-ion conductivity in dry atmospheres (> 400 ˚C, at high temperatures) and proton conductivity in hydrated atmospheres (< 400 ˚C, at lower temperatures)[80,81,94].

In such aspect, non-stoichiometric $Ba_3Ca_{1.18}Nb_{1.82}O_{9-\delta}$ (BCN18) exhibits proton conductivity of ~ 0.1 S/cm in humid atmosphere and exhibits high structural and chemical stability against carbon dioxide and humidified atmosphere. $Ba_3Ca_{1.18}Nb_{1.82}O_{9-\delta}$ was originally derived from $Ba_3CaNb_2O_9$ which is a 1:2-ordered perovskite-type and is an insulator with no lattice vacancies as the B-site ordering blocks the movement of ionic defects. By making the Ca^{2+} ion off-stoichiometry, oxygen vacancies are created which facilitates proton/oxide ion conductivity. Several research was conducted on studying the electrical properties of BCN18, which reveals that dopants in the Nb-site could improve the conductivity without compromising the chemical stability[99].

Several elements such as tantalum (Ta), titanium (Ti), iron (Fe), manganese (Mn), cobalt (Co), and potassium (K) are doped in the BCN perovskites to enhance the number of oxygen vacancies and maintains chemical stability[101–104]. The effect of potassium substitution on electrical properties of 1:1-ordered BCN proton conductors was found to have better conductivity and chemical stability can be achieved when 25% of the Ba-ions are replaced by potassium ions. Similarly, effects of cerium (Ce) and yttrium (Y) doping in the calcium and niobium ions in BCN perovskites for proton conductivity was also studied[105]. Such doping strategies have paved way for understanding the influence of B-site ions in dopant-property relationship. The doped BCN compositions and their conductivity values are listed in **Table 2.3**.

Table 2.3 Conductivities of doped BCN at specific temperature and medium[100].

Compositions	Conductivity (S/cm)
$Ba_3Ca_{1+x}Nb_{2-x}O_{9-\delta}$	5.5×10^{-4} , at 600 ˚C (air)
$Ba_2(Ca_{0.9}Nb_{0.66}Ta_{0.55})O_{6-\delta}$	5.0×10^{-4} , at 400 ˚C (wet)
$Ba_3Ca_{1.18}Nb_{1.82}Ti_{0.25}O_{8.605}$	3.5×10^{-4} , at 400 ˚C (wet)
$Ba_2(Ca_{0.79}Co_{0.5}Nb_{0.71})O_{6-\delta}$	3.7×10^{-2} , at 816 ˚C (air)
$Ba_2(Ca_{0.79}Mn_{0.5}Nb_{0.71})O_{5.09}$	7.74×10^{-4} , at 600 ˚C (air)
$Ba_2(Ca_{0.67}Fe_{0.33}Nb)O_{5.66}$	7.82×10^{-4} , at 600 ˚C (air)
$Ba_{1.75}K_{1.25}CaNb_2O_{9-\delta}$	1.0×10^{-3} , at 700 ˚C (dry H_2)
$Ba_4K_4Ca_4Nb_4O_{20}$	3.79×10^{-5} , at 800 ˚C (air)
$Ba_3Ca_{1.18}Nb_{1.77}Ni_{0.05}O_{9-\delta}$	2.6×10^{-3} , at 700 ˚C (wet air)
$Ba_3Ca_{1.18}Nb_{1.52}Y_{0.3}O_{9-\delta}$	5.3×10^{-3} , at 600 ˚C (wet air)
$Ba_3Ca_{1.18}Nb_{1.62}Ce_{0.2}O_{9-\delta}$	2.69×10^{-3} , at 550 ˚C (wet H_2 gas)

Simple perovskite-type $Ba(M'_{1/2}M''_{1/2})O_3$ oxides

Exploring the use of rare earth metals were dated back to 1960s, where Geller *et al*.,[106] reported rare earth ferrates, chromates, and aluminates for ABO_3 type of perovskites (A = rare earth, B = Fe, Cr, Al), which crystallises in orthorhombic or rhombohedral crystal system. The introduction of Ba^{2+} or Sr^{2+} ions of bigger ionic radii in the structure, forced the structure into octahedral coordinated B-sites. Compounds such as $A^{2+}(B_1)_{0.5}(B_2)_{0.5}O_3$ (B_1 can be rare earth ions like Tb, Dy, Ho, Er, Tm, Yb, Lu, Y with 3+ oxidation state, and B_2 can be transition metal ions with 5+ oxidation state). However, several metal ions were not suitable due to the tolerance factor that limits the formation of appropriate crystal structure that is not favourable for studying the electrical

properties. Brixner *et al.,* reported a series of $Ba(RE)_{0.5}Nb_{0.5}O_3$ perovskites (RE = Sc, Y, La, Ce, Pr, Nd, Sm, Eu, Gd, Tb, Dy, Ho, Er, Tm, Yb, Lu) for their structural stability and their dielectric properties[107]. Following years explored different dopants in the perovskite oxide $A(B'_{1/2}B''_{1/2})O_3$ where A = Ca, Sr, Ba; and B' = Fe^{3+} [108–111], Al^{3+} [112,113], Bi^{3+} [114], Ni^{3+} [115] , In^{3+} [116]. The structural analysis of $BaY_{0.5}Nb_{0.5}O_3$ (BYN) was first reported by Brixner *et al*.,[107] , found to be crystallising in cubic system with a $Pm\bar{3}m$ space group. The microwave dielectric properties of BYN were reported by Khalam *et al*[117] for its application as dielectric resonators in wireless communication system. Another group evaluated the crystal structure and phonon modes of BYN[118]. Prasad *et al*., reported the electrical properties of $BaY_{0.5}Nb_{0.5}O_3$ for the first time, and explained their charge transport mechanism and low dielectric constant and dielectric loss seems to make these compounds a better candidate in dielectric resonators[119]. These rare earth metals doped perovskites are of great interest due to their disordering in B-site which induces symmetry lowering, this structural variation is also influenced by various wet and dry chemical methods. These materials were studied by various researchers to understand their crystal structure as a function of chemical substitution; also, these perovskites are sensitive to their processing conditions which is related to their performance in desired applications[120]. Previous works on $Ba(Y_{1/2}Nb_{1/2})O_3$ showed structural ordering with tetragonal crystal structure when adopted with solid-state conventional synthesis sintered at ~1600 ˚C. However, the heating effects on the crystal structure when sintered over a varied temperature range are unknown. Followed by which, the same authors studied the crystal structure of these perovskites when adopted hydrothermal synthesis method with synthesis conditions (sintering between 600 – 1400 ˚C). These studies prove to be useful for applications in microwave-induced reactors and dielectrics. However, their crystal structure also influences the formation of oxygen vacancies upon aliovalent doping, whose potential were not studied

extensively[121]. In the current thesis (chapter – 6) explores the structural and electrical properties of several multi-element doped in the Ba- and Nb-sites of $BaY_{0.5}Nb_{0.5}O_3$.

2.3 Dielectric studies of perovskite oxides

Among the versatile properties of perovskite oxides, dielectric behaviour refers to how the material responds to an applied electric field, providing insights into its electrical conductivity and more electrical properties. These dielectric materials find applications in several energy storage devices[122–124], microwave dielectric resonators[125] and ferroelectrics[126,127]. The origin of dielectric behaviour in complex perovskite oxides is due to the displacement of metal ions that creates polarization when an external electric field is applied. Such polarization is favoured by structural instability that causes lattice deformation/ distortion[128]. Metal ions containing d^0 electronic configuration in the perovskites are known to exhibit distorted metal-oxygen polyhedral due to Jahn-teller distortion which is unique for several physio-chemical properties. The fundamentals of dielectrics are usually described by the energy storage capacitance property, described by the following equation:

$$C = \frac{\varepsilon_O \varepsilon_r A}{d} \tag{2.5}$$

where ε_O is the dielectric permittivity in vacuum (~8.85×10^{-12} F/m), ε_r is the dielectric constant (or relative dielectric permittivity) of the dielectric layer, A is the area of the two electrodes, and d is the thickness of the dielectric layer. The capacitance of a capacitor depends on the geometry of the capacitor and permittivity of the dielectric layer[129]. For high performance, these materials should present high dielectric constant (ε'), low dielectric loss (tan δ) to improve their selective application in microwave frequency region. The values of dielectric constant and dielectric loss of some known dielectric materials[130] are given in **Table 2.4**.

Table 2.4 Dielectric parameters (ε') and tan δ of known materials[130].

Dielectric medium/material	Dielectric constant	Dielectric loss
Dry air	1.0059	0
Nylon	3.4	0.0083
Polymers	1-6 – 4.0	0.0001 – 0.1
Glass	3.8 – 14.5	0.006 – 0.025
Alumina	9.0	0.0002 – 0.01
Distilled water	~80	0.04
$SrTiO_3$	233	< 0.02
$BaTiO_3$	1200	0.0001 – 0.02

The dielectric loss (tan δ) is highly dependent on the intrinsic properties (e.g., ionic polarization, crystalline structure) and extrinsic properties (e.g. vacancies, grain boundaries)[131]. The variation of dielectric constant and dielectric loss as a function of frequency can be used to distinguish the bulk, grain boundary and electrode effects[132–134]. The dielectric and ferroelectric properties of $BiFeO_3$ are improved by addition of $BaTiO_3$, whereas it drastically reduces the dielectric loss. Yadav *et al*., has reported that addition of glass to ceramics have improved the dielectric properties and have also retained their structural properties[135]. They have also reported that the addition of nucleation agent La_2O_3 enhances the value of dielectric constant, however addition of dopants like Nb_2O_5, and Ta_2O_5 decreases the values of dielectric constant. The dielectric properties were also

known to improve by the addition of La_2O_3, Bi_2O_3, CoO, Nb_2O_5, and K_2O in $SrTiO_3$[135]. Notably, the complex perovskites with chemical formula $A_3B'B''_2O_9$ (with B'^{2+} and B''^{5+}) beholds all the properties mentioned above, along with structural ordering from simple cubic to one of the superstructures. When completely ordered, the B'^{2+} and B''^{5+} ions are randomly distributed into the B-site of the cubic $Ba(B',B'')O_3$ perovskite oxide. Tantalum-based ceramics, like $Ba_3B'Ta_2O_9$ (B' = Mg, Zn), exhibits attractive dielectric properties at relatively higher frequencies (9 – 10 GHz)[136]. Complex Ta-based perovskites tends to exhibit smaller dielectric constant (ε') and small dielectric loss (tan δ) than other corresponding niobium analogues. Particularly, $BaM'_{1/3}Ta_{2/3}O_3$ (M' = Mg, Zn) based perovskites exhibit low dielectric loss and low temperature coefficient. This makes them preferred for fabricating dielectric resonators. Young Kim *et al*., explored the structural and dielectric properties of Mg/Ta complex perovskites $ALaMgTaO_6$ (A = Ca, Sr, Ba) and $La_2Mg(Mg_{1/3}Ta_{2/3})O_6$. Out of the explored materials, $BaLaMgTaO_6$ have high dielectric constant (ε' = 19) and is temperature independent[137]. However, high cost of tantalum oxide increases the price of the devices, therefore, the substitution of tantalum by niobium is an excellent choice, as both Ta^{5+} and Nb^{5+} have similar ionic radii. For the past decade, several authors have reported the structural ordering and their physical properties of niobium-based perovskites. Khalyavin *et al*.,[138] have reported the dielectric properties of Ba_2MWO_6 (M = Mg, Ni, Zn) compounds. Further studies were done by Zhao *et al.*[139], by tuning a series of tungsten based double perovskites A_2BWO_6 (A = Sr, Ba; B = Co, Ni, Zn). Here, the Ni-doped compounds shows higher ordering on B-site ions than that of Zn- and Co- analogues.

Chapter 3 Experimental methods

This chapter overviews about the experimental methods that were used throughout this thesis.

3.1 Preparation of perovskite oxides

3.1.1 Synthesis of $Ba_2Ca_{0.67}Nb_{1.33-x}Cu_xO_{6-\delta}$ (x = 0, 0.05, 0.13 and 0.26) and $Ba_2Ca_{0.67-x}Cu_xNb_{1.33}O_{6-\delta}$ (x = 0, 0.13).

The double perovskite oxide powders were synthesized by conventional solid-state ball milling technique by using stoichiometric amounts of precursors of high purity, $Ba(NO_3)_2$ (99% Alfa Aesar), $CaCO_3$ (99% Sigma-Aldrich), Nb_2O_5 (99% Alfa Aesar), and CuO (99% Alfa Aesar). The stoichiometric amounts of precursor powders were mixed with 2-propanol was ball milled (Pulverisette, Fritsch, Germany) for 6 h at 200 RPM using ZrO_2 balls with rotation in alternate direction to ensure proper mixing. The solvent was evaporated, and the powders were calcined at 900 ˚C for 15 h in an alumina crucible to remove the nitrates and carbonates. The resultant powders were re-milled again for another 6 hours using ZrO_2 balls in 2-propanol with similar procedure. The dried powders were pressed into cylindrical pellets (~2 mm diameter, ~ 1mm thick) using isostatic pressure and the pellets were sintered in air at 1200 ºC for 12 h at 5-8 ºC min^{-1} ramp rate.

3.1.2 Synthesis of $BaY_{0.5}Nb_{0.5}O_3$, $Ba_{0.5}Sr_{0.5}Y_{0.5}Nb_{0.4}Mg_{0.1}O_{3-\delta}$ and $Ba_{0.5}Sr_{0.5}Y_{0.5}Nb_{0.4-x}Mg_{0.1}Ni_xO_{3-\delta}$ (x = 0.1 and 0.2).

Stoichiometric amounts of $Ba(NO_3)_2$ (99% Alfa Aesar), $Sr(NO_3)_2$ (99% Sigma-Aldrich), Y_2O_3 (99% Alfa Aesar), Nb_2O_5 (99% Alfa Aesar), $Mg(NO_3)_2.6H_2O$ (99% Sigma-Aldrich) and NiO (99% Sigma-Aldrich) were ball milled (Pulverisette, Fritsch, Germany) for 6 h at 200 RPM using ZrO_2 balls with rotation in alternate direction to ensure proper mixing. The solvent was evaporated, and the powders were calcined at 900 ˚C for 12 - 15 h in an alumina crucible to remove the nitrates and carbonates. The resultant powders were re-milled again for another 6 hours under similar

procedure. The dried powders were pressed into cylindrical pellets (~2 mm diameter, ~ 1mm thick) using isostatic pressure and the pellets were sintered in air at 1300 - 1400 ºC for 15 – 22 h at 5 - 8 ºC min^{-1} ramp rate.

3.2 Phase and morphology characterization

3.2.1 Powder X-ray diffraction (PXRD)

Powder X-ray diffraction (PXRD) is the most extensively used technique to identify the crystalline phases and to determine crystal structures among the other techniques such as electron diffraction, TEM, neutron diffraction. The principle of XRD technique is based on scattering of X-rays by a crystal consisting of well-defined array of atoms, ions, and molecules. The inter-planar spacing (or distances) is of the same magnitude as the wavelength of X-rays (0.5 - 2 Å) and hence, crystal planes act as diffraction gratings. Interaction of X-rays reflected by a set of parallel planes satisfying Bragg's condition (**equation 3.1, Figure 3.1**) led to constructive interference only at a particular angle. The Bragg condition for the occurrence of such diffraction can be written as:

$$n\lambda = 2d \sin\theta \quad (3.1)$$

where, λ is wavelength of X-rays, θ is the glancing angle (called as Bragg's angle), d is inter-planar separations, and n is the order of diffraction. Room temperature PXRD measurements were carried out using a Bruker D8 Advance powder X-ray diffractometer (Cu Kα, λ = 1.54 Å, 40 kV, 40 mA) measured from 2θ = 10˚ to 80˚ at a count rate of 6 s per step with an increment of 0.02˚ at ambient air. The PXRD results were refined by Rietveld refinement method using GSAS II[140] software and the cell parameters and atomic positions were obtained.

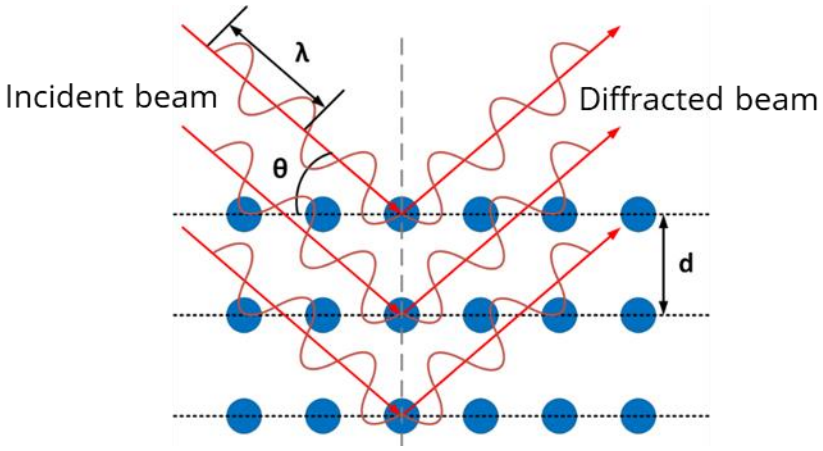

Figure 3.1 Schematic of X-ray diffraction illustrated using Bragg's law.

For compositions in Chapter-6, PXRD patterns were obtained with a 0.01˚ step size and a counting time of 3 s per step in ambient air from 10˚ to 80˚.

3.2.2 Scanning electron microscopy/ Elemental identification (SEM/EDX)

In SEM technique, the electrons from a finely focused beam are bombarded onto and reflected from the surface of the sample. These electrons interact with the sample and generate, X-rays, backscattered and secondary electrons. These secondary electrons are detected to give a map of the surface topography of the sample. It is useful for looking at particle size, crystal morphology, magnetic domains, and surface defects. Samples with poor conductivity were covered with a noble metal layer (Au) to avoid charge buildup, which causes accumulation of electric field and resulting in poor imaging. In electron microscopy, the elements present in the sample also emit characteristic X-rays whose energy can be scanned to result in energy dispersive X-ray analysis (EDX), to give both qualitative and quantitative analysis of the elements present in the sample. In the current thesis, samples (in chapters 4 and 6) were studied with SEM/EDX for their surface features, identification, and quantification of elements by using ThermoFisher Scientific Phenom G6 Pro operated at an accelerating voltage of 15 kV.

3.2.3 Fourier transform infrared (FTIR) spectroscopy

FTIR spectra was recorded using Agilent Cary 630 FT-IR Spectrometer to look-up for the peaks denoting the presence of carbonate (at ca. 1500 cm^{-1}) and hydroxide (at ca. 3000 cm^{-1}) peaks. FT-IR technique was used for post-treatment characterization.

3.2.4 Chemical stability measurements under CO_2 and boiling water

Ex-situ chemical stability of the ceramic samples under boiling water was performed by hanging the powdered samples exposed to boiling water (~ 100 ˚C) for 72 h. *Ex-site* chemical stability under CO_2 was carried out by flowing pure CO_2 at 600 ˚C for 72 h to powdered samples inside quartz tube.

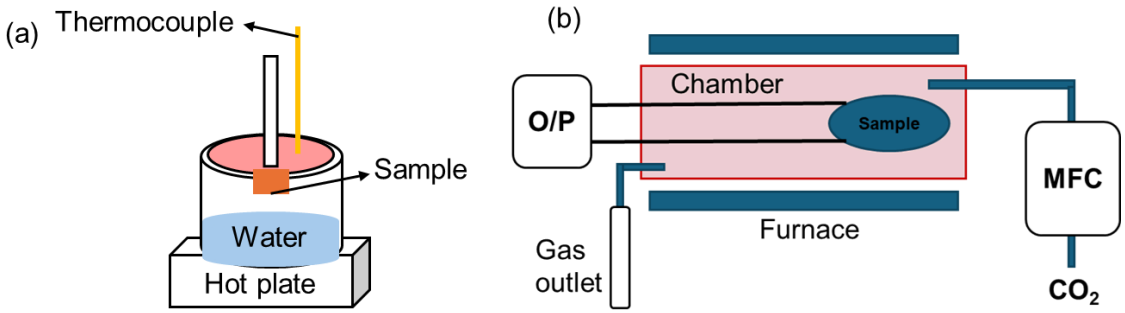

Figure 3.2 Schematic representation of chemical stability tests under (a) boiling water (~100 ºC) for 72 h, and (b) ex-situ CO_2 at 600 ºC for 72 h.

3.3 Electrochemical impedance spectroscopy (EIS)

EIS technique, also known as AC impedance spectroscopy, can be used for measuring the electrical properties of crystalline ionic conducting samples in which a wide range of frequency is applied that helps in distinguishing the impedance due to bulk and grain boundary (GB) contributions. Fig. x shows the Brick-layer model (BLM) which is commonly used for calculating the bulk (σ_{bulk}) and GB (σ_{gb}) conductivities of polycrystalline ceramics[141]. A typical BLM is a material with a

dimension (A/l = 1 cm) and permittivity of ca. 10 should have a capacitance of 10^{-12} F, from the following equation,

$$C = \varepsilon \varepsilon 0 \frac{A}{l} \quad (3.2)$$

Where, ε, ε_0, A and l is medium of permittivity, permittivity of free space (8.854×10^{-14} Fcm^{-1}), area and length, respectively.

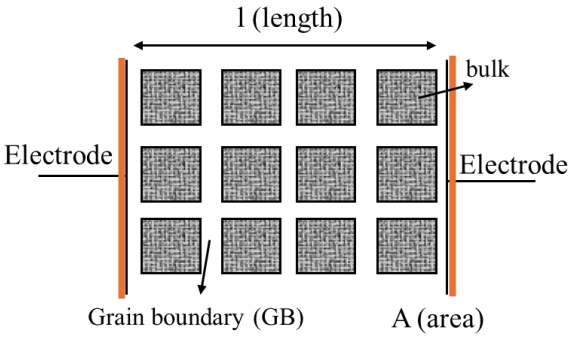

Figure 3.3 Schematic of brick-layer model of bulk and grain-boundary region in a ceramic placed between metal electrodes[141].

Table 3.1 Capacitance values and their respective phenomenon[141].

Capacitance (F)	Phenomenon
10^{-12}	Bulk, major phase
10^{-11}	Bulk, minor/secondary phase
10^{-11} – 10^{-9}	Grain-boundary
10^{-9} – 10^{-7}	Surface layer
10^{-7} – 10^{-5}	Sample-electrode interface
10^{-4}	Electrochemical reaction(s)

EIS data are represented in the form of Nyquist plot, where the imaginary part, Z'' (capacitive) is plotted against real part, Z' (resistive) (**Figure 3.4**). An ideal Nyquist plot consists of three

semicircles, first one at high frequency, second one at intermediate frequency and the third one at low frequency. The x-axis intercept (Z') gives the R values, and the C values can be obtained from equation x, which is further assigned based on the magnitude of the capacitance value suggested by Irvine *et al.*[141]. The high frequency semicircle has lower capacitance value, and its R is attributed to the bulk properties of the sample; the intermediate frequency semicircle is due to grain-boundary contribution and the lower frequency semicircle is due to sample-electrode interface or electrochemical reaction based on the capacitance value (**Table 3.1**).

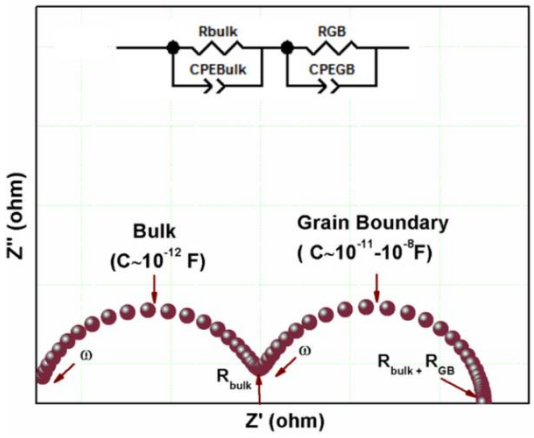

Figure 3.4 Typical simulated Nyquist plot showing bulk and GB contribution; (inset) electrical circuit[141].

Conductivities can be calculated using the following formula,

$$\sigma = \frac{1}{R}\frac{l}{A} \tag{3.3}$$

where, l, A and R are the thickness, area of the sample and resistance associated with the respective contributions. Although, BLM assumes that there is a uniform distribution of grain boundaries with identical properties considering that all grains will have different shapes and sizes and irregular contact between two grains and that different types of grain boundary might be present[141]. The temperature dependent conductivity is also calculated using the following Arrhenius equation,

$$\sigma = A \exp \frac{-Ea}{RT} \quad (3.4)$$

where, A is the pre-exponential factor, Ea is activation energy, R is the gas constant and T is the respective temperature. For the conductivity measurements, powdered samples were pressed into thin pellets of ~1 cm diameter and ~0.1 cm thickness and brush painted with Au paste (company name) on both sides acting as electrodes and heated at 700 ˚C for 1 h to remove the organic binders. Electrical conductivity measurements were performed in the temperature range of 300 – 750 ˚C in air, dry N_2, 3% H_2O+N_2 and 3% D_2O+N_2 medium using AC impedance analyser (Solartron 1260) over the frequency range of 10^{-1} to 10^6 Hz with an AC potential of 100 mV. Electrical measurements were performed by loading the pelletized sample in a spring-loaded contact inside a sealed quartz tube and a tubular furnace was used to conduct temperature-controlled conductivity measurements. N_2 gas was bubbled through H_2O and D_2O at 25 ˚C to determine if H^+ is the major charge carriers in humid medium leading to proton conductivity. The samples were equilibrated for 2 h at each temperature before taking measurements. Zview® modelling software (Scribner Associates, Inc.) was used to analyse the AC impedance spectra.

3.4 Dielectric studies using AC impedance spectroscopy

The dielectric parameters are usually measured by assuming the dielectrics based on sandwich of metal-dielectric-metal schematic. The dielectric constant (ε') is defined as the ratio of stored capacitance of the cell with the vacuum (when a certain potential is applied). The dielectric loss is the loss of energy involved in heating a dielectric material under a certain electric field. It is measured in terms of loss tangent (tan δ), which is a dimensionless quantity. The dielectric constant (ε') is calculated using the following equation (**equation 3.5**):

$$\varepsilon' = \frac{Z''^2}{Z'^2+Z''^2} * \frac{1}{2*3.14*f} * \frac{t}{area * \varepsilon_0} \quad (3.5)$$

where, Z" is the imaginary impedance (kΩ cm), Z' is the real impedance (kΩcm), f is the frequency, t is the thickness of the dielectric layer, area is the area of the dielectric layer, ε_0 is the dielectric of permittivity of free space (8.854 x 10^{-12} F/m). Similarly, the dielectric loss is defined by the following equation (**equation 3.6**):

$$\tan\delta = \frac{Z'}{Z''} \tag{3.6}$$

The relationship between the impedance and frequency can be explained by the following expression:

$$Z = \frac{1}{Q*(j*\omega)^n} \tag{3.7}$$

where, $\omega = 2\pi f$ (f is the frequency), Q is the pseudo-capacitance, j is $\sqrt{-1}$ and n is the empirical constant (arbitrary value between 0 and 1).

3.5 Error considerations

The current section of the thesis discusses the possible error sources with PXRD, SEM, and EIS measurements that might have impact on the results discussed in the chapters.

- Multiple batches of samples were prepared for compositions discussed in chapters 4 -6 to ensure reproducibility of the synthesis method.
- The temperature of the muffle furnace might fluctuate ± 5 ˚C, which meant the perovskite samples might not be sintered at exactly the set temperature.
- The precursor materials used in the perovskite synthesis were not 100% pure.
- Error in PXRD measurements due to sample placement is avoided by levelling the surface of powder in the sample holder with a glass slide.

- The CO_2 gas used for chemical stability is not 100 % pure and might contain few ppm of other gases.
- Dummy cell (1.9 - 9.3 kΩ) is used for calibrating the frequency response analyser (Solartron 1260) and they may have a 0.1% error in the resistance measurement.
- The tubular furnace has a temperature fluctuation of +/- 3 ˚C. To track any changes in the conductivity and electrochemical performance of ceramics due to high temperatures, all measurements were done in both heating and cooling cycles.
- The dimension of the pellets used for electrical characterization was measured by using a digital calliper that has an associated (±0.03 mm) error from the manufacturer (VWR® Digital Callipers).
- The accurate flow of dry N_2 and $N_2 + H_2O$ (25 ˚C) was maintained by using mass flow controllers during conductivity and electrochemical measurements (Chapters 4, 5).

Chapter 4 Transition metal-doped double perovskite-type electrolyte $Ba_2Ca_{0.67}Nb_{1.33-x}M_xO_{6-\delta}$ (x = 0, 0.05, 0.13 and 0.26) and $Ba_2Ca_{0.67-x}M_xNb_{1.33}O_{6-\delta}$ (x = 0 and 0.13)

4.1 Introduction

Amongst various perovskites, $BaCe_{1-x}M_xO_{3-\delta}$ shows high proton conduction compared to their Sr or Ca analogues[142,143]. One of the main concerns for these materials is their structural stability under operating conditions[144–147]. For instance, $BaCeO_3$ perovskites tends to react with CO_2 and H_2O at high temperatures and forms $BaCO_3$ and $Ba(OH)_2$, respectively,

$$BaCeO_{3(s)} + H_2O_{(g)} \rightarrow Ba(OH)_{2(s)} + CeO_{2(s)}$$

$$BaCeO_{3(s)} + CO_{2(g)} \rightarrow BaCO_{3(s)} + CeO_{2(s)}$$ [142,143,147–150]

The formation of these compounds over a period, reduces the performance of the material by acting as an impurity that disrupts the structural and physical properties of the desired perovskites. Various elements were substituted for Ba and/or Ce sites to address the chemical stability issue without compromising the proton conductivity[151–154]. Previous studies on $Ba_3CaNb_2O_9$ shows that these class of double perovskite oxides have exceptional chemical stability in CO_2 and exhibits better proton conduction[155–159]. However, they are less explored due to their complex structure due to the different phases and crystal structure because of controlled site ordering. Nowick *et al.*,[160–162] and several others[163–168] explored the proton conductivity in non-stoichiometric double perovskite-type $Ba_2Ca_{2/3}Nb_{4/3}O_6$ (BCN). Several authors have studied the influence of transition metal doping in B-site of the double perovskite oxides which has led to fruitful studies that improved the proton conductivity without compromising their chemical stability. Upon understanding the electrical conductivity of these double perovskites by various transition-metal dopants, it is of interest to investigate the doping of Cu^{2+} (r_{Cu2+} = 0.73 Å), whose ionic radii is

appreciably closer to that of Nb^{5+} (r_{Nb5+} = 0.64 Å) which is expected to favour ordered double perovskite structures and is well-known for their exceptional electrical conductivity. In this chapter, we have explored the structural, physical, and electrical properties of Cu-doped double perovskite-type $Ba_2Ca_{2/3}Nb_{4/3}O_6$ (BCN) and their chemical stability in CO_2- and moisture-containing environments.

4.2 Results and discussion

4.2.1 Structural and surface characterization

The detailed synthesis method for double perovskite-type $Ba_2Ca_{0.67}Nb_{1.33-x}Cu_xO_{6-\delta}$ (x = 0, 0.05, 0.13 and 0.26) and $Ba_2Ca_{0.67-x}Cu_xNb_{1.33}O_{6-\delta}$ (x = 0 and 0.13) oxides were presented in **section 3.1.1**. The parent phase $Ba_3CaNb_2O_9$ (BCN) was found to crystallize with a *P3̄m1* space group (trigonal structure)[161,162], with a *Fm3̄m* space group (cubic structure)[162], and with a *Pm3̄m* space group (cubic structure)[169].

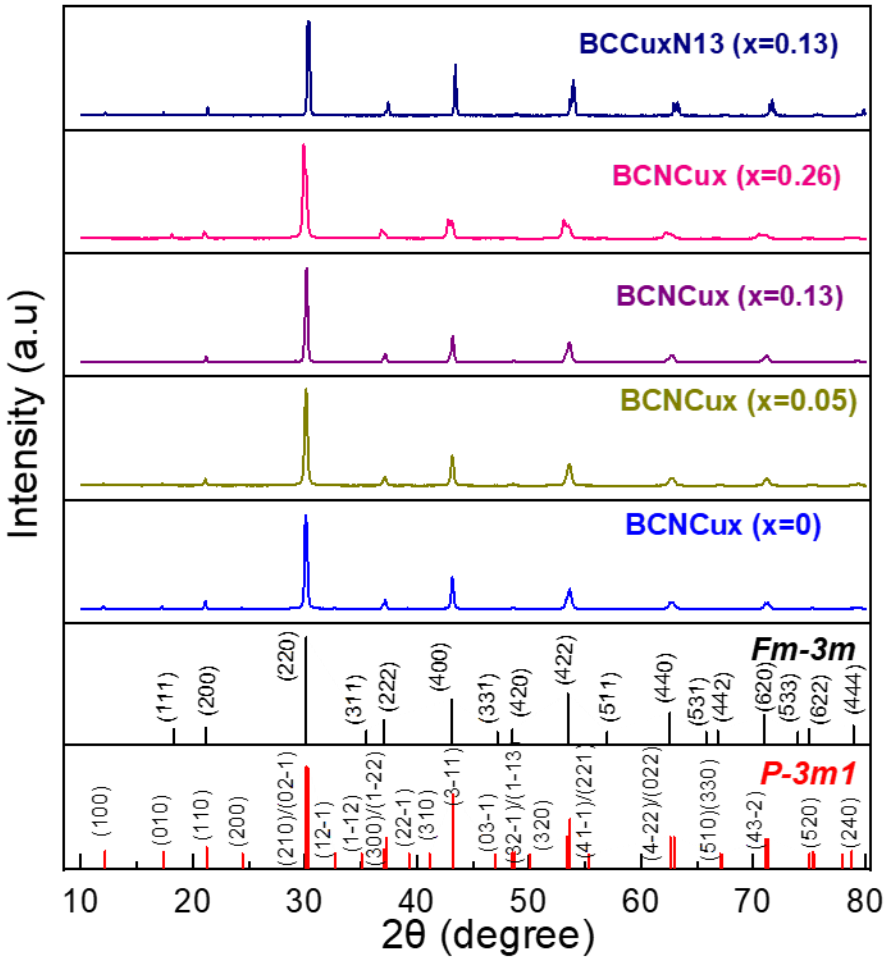

Figure 4.1 The PXRD patterns of $Ba_2Ca_{0.67}Nb_{1.33-x}Cu_xO_{6-\delta}$ (x = 0, 0.05, 0.13 and 0.26) and $Ba_2Ca_{0.67-x}Cu_xNb_{1.33}O_{6-\delta}$ (x = 0 and 0.13) after sintering at 1200 ˚C for 12 h in air, indexed with phases P3̄m1 (ICSD no. 162758)[170] and Fm3̄m (ICSD no. 93400)[171].

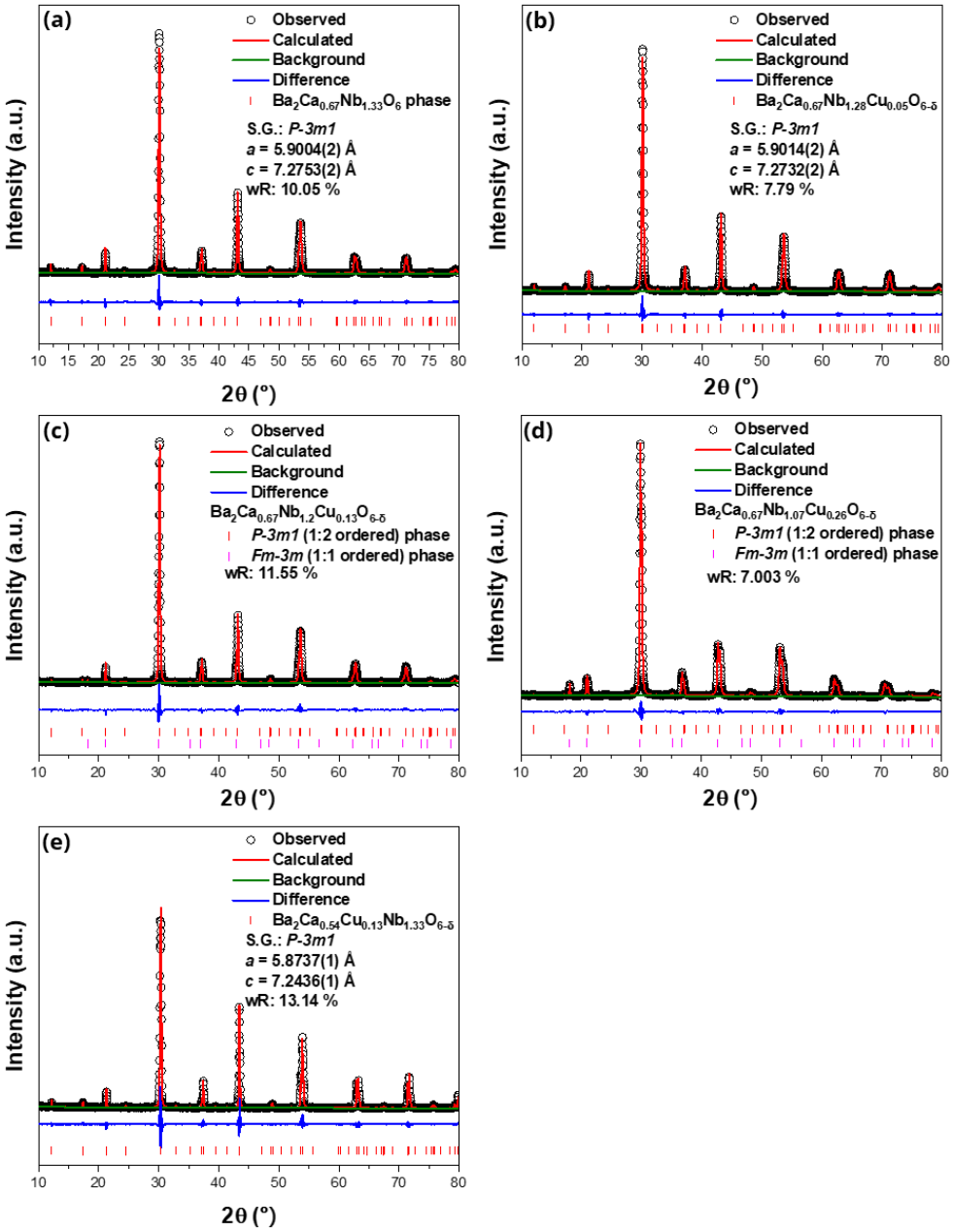

Figure 4.2 PXRD Rietveld refinement of (a) $Ba_2Ca_{0.67}Nb_{1.33}O_6$, (b) $Ba_2Ca_{0.67}Nb_{1.28}Cu_{0.05}O_{6-\delta}$, (c) $Ba_2Ca_{0.67}Nb_{1.2}Cu_{0.13}O_{6-\delta}$, (d) $Ba_2Ca_{0.67}Nb_{1.07}Cu_{0.26}O_{6-\delta}$, and (e) $Ba_2Ca_{0.54}Cu_{0.13}Nb_{1.33}O_{6-\delta}$ indexed with phases in a $P\bar{3}m1$ (ICSD no. 162758) and a $Fm\bar{3}m$ (ICSD no. 93400) sintered in air at 1200 ºC for 12 h.

Figure 4.1 represents the X-ray diffraction (XRD) patterns of as-prepared $Ba_2Ca_{0.67}Nb_{1.33-x}Cu_xO_{6-\delta}$ (x = 0, 0.05, 0.13 and 0.26) and $Ba_2Ca_{0.67-x}Cu_xNb_{1.33}O_{6-\delta}$ (x = 0 and 0.13) after sintering at 1200 ˚C, indexed to reference pattern of phases $P\bar{3}m1$[170] and $Fm\bar{3}m$[171]. The parent phase $Ba_2Ca_{0.67}Nb_{1.33}O_6$ (BCN) and $Ba_2Ca_{0.67}Nb_{1.33-x}Cu_xO_{6-\delta}$ (x = 0.05) were found to exhibit trigonal $P\bar{3}m1$ (ICSD no. 162758) (**Figures 4.2(a) and 4.2(b)**) with 1:2 ordering on the B-sites (*1b* and *2d*) [172]. $Ba_2Ca_{0.67}Nb_{1.33-x}Cu_xO_{6-\delta}$ (x = 0.13 and 0.26) exhibited a coexistence of 1:2 B-site ordered $P\bar{3}m1$ and 1:1 B-site ordered cubic $Fm\bar{3}m$ (ICSD no. 93400) phases. Previous work on transition-metal doped BCN reported the formation of trigonal B-site 1:2 ordered perovskite phase ($P\bar{3}m1$) at a sintering temperature of ca. 1200 °C and a transition to the B-site 1:1 ordered perovskite phase ($Fm\bar{3}m$) above ca. 1300 °C[173]. In addition, the formation of the $Fm\bar{3}m$ phase was observed with the Cu-BCN compositions as the Ca/Nb ratio increased. The intensity of one of the most characteristic peaks for $Fm\bar{3}m$ ((111) diffraction peak at ca. 2θ = 18.1°) increased as x in $Ba_2Ca_{0.67}Nb_{1.33-x}Cu_xO_{6-\delta}$ increased from x = 0.13 to 0.26 (**Figures 4.2(c) and 4.2(d)**). On the other hand, incorporating Cu in the Ca site in $Ba_2Ca_{0.67-x}Cu_xNb_{1.33}O_{6-\delta}$ (x = 0.13) results in the formation of the trigonal $P\bar{3}m1$ phase. The structural parameters of the Cu-BCN were further analysed by Rietveld refinement and are summarized in **Tables 4.1 and 4.2**. The refinement was first considered for one phase of trigonal crystal structure with $P\bar{3}m1$ space group, which resulted in additional undefined diffraction peaks for the compositions $Ba_2Ca_{0.67}Nb_{1.2}Cu_{0.13}O_{6-\delta}$ and $Ba_2Ca_{0.67}Nb_{1.07}Cu_{0.26}O_{6-\delta}$. Secondary phase with cubic crystal structure and space group $Fm\bar{3}m$ where the Nb atoms at 4*b* site intercalate with a mixture of Ca and Nb at 4*a* site, which is in great agreement with the literature[158,174]. The refined U_{iso} values for all atoms (Ba, Nb, Cu, O) are in the range of 0.01 – 0.06 Å^2 except for Ca atom in certain compositions $Ba_2Ca_{0.67}Nb_{1.29}Cu_{0.05}O_{6-\delta}$, $Ba_2Ca_{0.67}Nb_{1.2}Cu_{0.13}O_{6-\delta}$ and $Ba_2Ca_{0.67}Nb_{1.07}Cu_{0.26}O_{6-\delta}$ (in $P\bar{3}m1$ space group) could not be refined

accurately. Thus, known literature U_{iso} value (0.003 $Å^2$)[174] was used for refining the thermal parameters for Ca atoms. Although, more detailed studies of the structural analysis are limited in the current method, several attempts and models were made to obtain the refinement parameters that almost matches with the experimental data. The proposed structural models were supported by good fits (wR) on the refinements. However, higher than expected wR values were obtained because of the presence of some unknown minor impurities in the diffraction patterns.

Table 4.1 Structural parameters of $Ba_2Ca_{0.67}Nb_{1.33-x}Cu_xO_{6-\delta}$ (x = 0 and 0.05) and $Ba_2Ca_{0.67-x}Cu_xNb_{1.33}O_{6-\delta}$ (x = 0.13) with single phase in $P\bar{3}m1$ space group obtained from PXRD Rietveld refinement analysis.

Atom	**$Ba_2Ca_{0.67}Nb_{1.33}O_6$** ***$P\bar{3}m1$***	**$Ba_2Ca_{0.67}Nb_{1.28}Cu_{0.05}O_{6-\delta}$** ***$P\bar{3}m1$***	**$Ba_2Ca_{0.54}Cu_{0.13}Nb_{1.33}O_{6-\delta}$** ***$P\bar{3}m1$***
Lattice parameters	a = 5.9004(2) Å, 7.2753(2) Å,	*a* = 5.9014(2) Å, *c* = 7.2732(2) Å,	*a* = 5.8737(1) Å, *c* = 7.2436(1) Å
Ba1	**1*a***	**1*a***	**1*a***
x	0	0	0
y	0	0	0
z	0	0	0
fraction	1	1	1
U_{iso} ($Å^2$)	0.0372(12)	0.0352(11)	0.0110(15)
Ba2	**2*d***	**2*d***	**2*d***
x	0.3333	0.3333	0.3333
y	0.6667	0.6667	0.6667

z	0.6698(5)	0.6718(4)	0.6702(7)
fraction	1	1	1
U_{iso} (Å^2)	0.0335(7)	0.0309(7)	0.0132(10)
Ca1	**1*b***	**1*b***	**1*b***
x	0	0	0
y	0	0	0
z	0.5	0.5	0.5
fraction	1	1	0.9
U_{iso} (Å^2)	0.0138(31)	0.003	0.003(4)
Nb1	**2*d***	**2*d***	**2*d***
x	0.3333	0.3333	0.3333
y	0.6667	0.6667	0.6667
z	0.1690(6)	0.1685(6)	0.1683(9)
fraction	1	0.96	1
U_{iso} (Å^2)	0.0296(10)	0.0297(6)	0.0041(12)
Cu1	**-**	**2*d***	**1*b***
x	-	0.3333	0
y	-	0.6667	0
z	-	0.1685(6)	0.5
fraction	-	0.04	0.1
U_{iso} (Å^2)	-	0.0297(6)	0.003(4)
O1	**6*i***	**6*i***	**6*i***
x	0.1679(7)	0.1676(6)	0.1710(12)

y	0.8319(7)	0.8322(6)	0.8288(12)
z	0.3296(12)	0.3300(10)	0.3184(18)
fraction	1	1	1
U_{iso} (Å^2)	0.0444(30)	0.0475(31)	0.017(4)
O2	***3e***	***3e***	***3e***
x	0.5	0.5	0.5
y	0	0	0
z	0	0	0
fraction	1	0.9824	1
U_{iso} (Å^2)	0.063(6)	0.042(5)	0.020(8)
wR	10.05 %	7.79 %	13.14 %

Table 4.2 Structural parameters of $Ba_2Ca_{0.67}Nb_{1.33-x}Cu_xO_{6-\delta}$ (x = 0.13 and 0.26) with mixed phases in $P\bar{3}m1$ and $Fm\bar{3}m$ space group obtained from PXRD Rietveld refinement analysis.

Atom	**$Ba_2Ca_{0.67}Nb_{1.2}Cu_{0.13}O_{6-\delta}$**		**$Ba_2Ca_{0.67}Nb_{1.07}Cu_{0.26}O_{6-\delta}$**	
	$P\bar{3}m1$	***$Fm\bar{3}m$***	***$P\bar{3}m1$***	***$Fm\bar{3}m$***
Lattice parameters	*a* = 5.9105(3) Å, *c* = 7.2696(3) Å (f*rac.* = 93%)	*a* = 8.4174(4) Å (f*rac.* = 7%)	*a* = 5.9277(5) Å, *c* = 7.2284(4) Å (f*rac.* = 63.4%)	*a* = 8.4315(2) Å (f*rac.* = 36.6%)
Ba1	**1*a***	**8*c***	**1*a***	**8*c***
x	0	0.25	0	0.25
y	0	0.25	0	0.25

z	0	0.25	0	0.25
fraction	1	1	1	1
U_{iso} (Å^2)	0.0329(18)	0.0311(21)	0.050(3)	0.0388(7)
Ba2	**2*d***	**-**	**2*d***	**-**
x	0.3333	-	0.3333	-
y	0.6667	-	0.6667	-
z	0.6666(6)	-	0.6668(12)	-
fraction	1	-	1	-
U_{iso} (Å^2)	0.0213(10)	-	0.0293(17)	-
Ca1	**1*b***	**4*a***	**1*b***	**4*a***
x	0	0	0	0
y	0	0	0	0
z	0.5	0	0.5	0
fraction	1	0.785	1	0.785
U_{iso} (Å^2)	0.003	0.0190(28)	0.003	0.0233(8)
Nb1	**2*d***	**4*b***	**2*d***	**4*b***
x	0.3333	0.5	0.3333	0.5
y	0.6667	0.5	0.6667	0.5
z	0.1687(9)	0.5	0.1697(30)	0.5
fraction	0.9	0.9	0.93	0.85
U_{iso} (Å^2)	0.0191(9)	0.0190(28)	0.030(3)	0.0233(8)
Nb2	**-**	**4*a***	**-**	**4*a***
x	-	0	-	0

y	-	0	-	0
z	-	0	-	0
fraction	-	0.215	-	0.215
U_{iso} (Å^2)	-	0.0190(28)	-	0.0233(8)
Cu1	**2*d***	**4*b***	**2*d***	**4*b***
x	0.3333	0.5	0.3333	0.5
y	0.6667	0.5	0.6667	0.5
z	0.1687(9)	0.5	0.06(5)	0.5
fraction	0.1	0.1	0.07	0.15
U_{iso} (Å^2)	0.0191(9)	0.0190(28)	0.03(3)	0.0233(8)
O1	**6*i***	**24*e***	**6*i***	**24*e***
x	0.1564(9)	0.2590(20)	0.1491(15)	0.2656(6)
y	0.8434(9)	0	0.8507(15)	0
z	0.3400(16)	0	0.3447(26)	0
fraction	1.0272	1	1.0071	0.9696
U_{iso} (Å^2)	0.027(4)	0.074(9)	0.018(6)	0.0493(21)
O2	**3*e***	**-**	**3*e***	**-**
x	0.5	-	0.5	-
y	0	-	0	-
z	0	-	0	-
fraction	0.9667	-	0.9333	-
U_{iso} (Å^2)	0.064(10)	-	0.128(21)	-
wR	12.365 %		7.003 %	

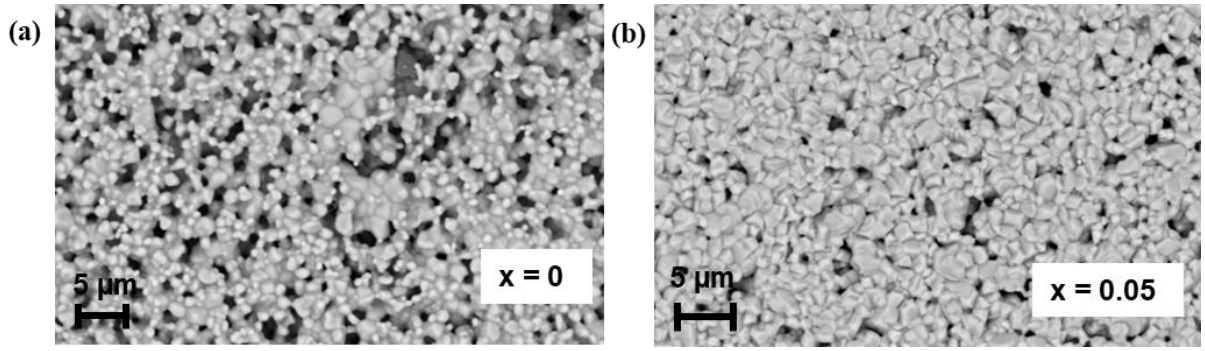

Figure 4.3(a) and (b) Scanning electron microscopy images of $Ba_2Ca_{0.67}Nb_{1.33}O_6$ (x = 0) and $Ba_2Ca_{0.67}Nb_{1.28}Cu_{0.05}O_{6-\delta}$ (x = 0.05) which shows porous morphology.

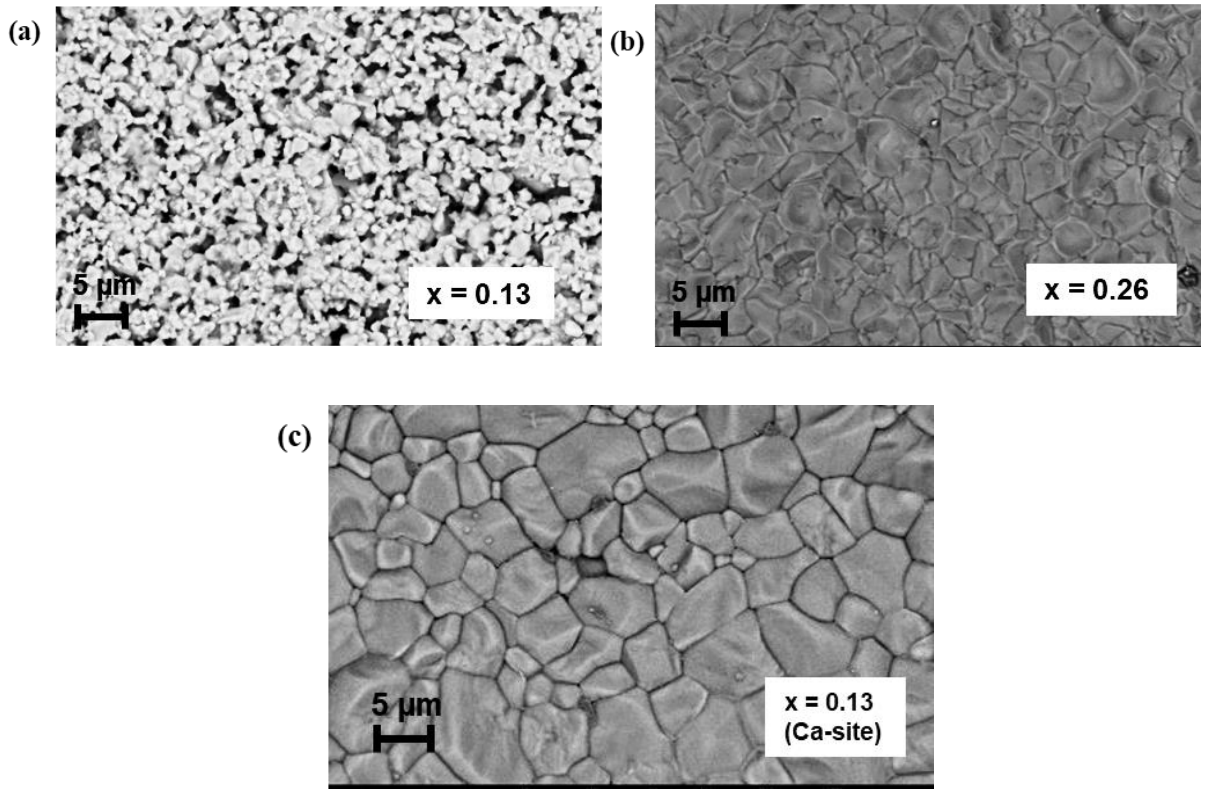

Figure 4.4(a-c) Scanning electron microscopy images of $Ba_2Ca_{0.67}Nb_{1.2}Cu_{0.13}O_{6-\delta}$ (x = 0.13), $Ba_2Ca_{0.67}Nb_{1.07}Cu_{0.26}O_{6-\delta}$ (x = 0.26), and $Ba_2Ca_{0.54}Cu_{0.13}Nb_{1.33}O_{6-\delta}$ (x = 0.13, Ca-site). These compositions were well sintered with less grain boundaries compared to other compositions.

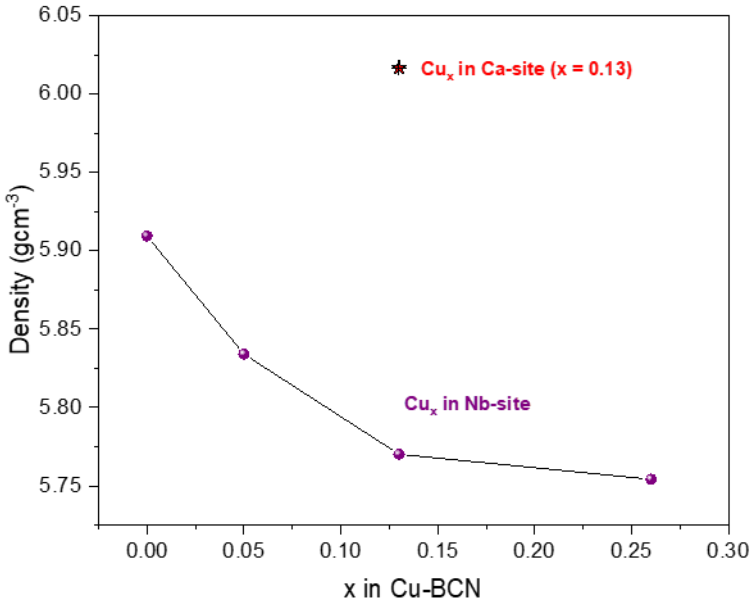

Figure 4.5 Densities of $Ba_2Ca_{0.67}Nb_{1.33-x}Cu_xO_{6-\delta}$ (x = 0, 0.05, 0.13 and 0.26) (denoted in purple dots) and $Ba_2Ca_{0.67-x}Cu_xNb_{1.33}O_{6-\delta}$ (x = 0.13) (in red star) double perovskite oxides, calculated from Rietveld refinement. x = 0.13 (in Ca-site) has highest density, which can be related with the corresponding SEM morphology.

The morphology of $Ba_2Ca_{0.67}Nb_{1.33-x}Cu_xO_{6-\delta}$ (x = 0, 0.05, 0.13 and 0.26) and $Ba_2Ca_{0.67-x}Cu_xNb_{1.33}O_{6-\delta}$ (x = 0.13) is depicted in **Figures 4.2 and 4.3**. The double perovskite compositions $Ba_2Ca_{0.67}Nb_{1.07}Cu_{0.26}O_{6-\delta}$ and $Ba_2Ca_{0.54}$ $Cu_{0.13}Nb_{1.33}O_{6-\delta}$ exhibits well sintered samples with less grain boundary, whereas $Ba_2Ca_{0.67}Nb_{1.33}O_6$, $Ba_2Ca_{0.67}Nb_{1.28}Cu_{0.05}O_{6-\delta}$ and $Ba_2Ca_{0.67}Nb_{1.2}Cu_{0.13}O_{6-\delta}$ displays visible grain boundary with porous morphology that shows distinct grains and grain boundary within the examined region. Samples that show distinct particles with pores have more resistance between the grains due to charge transfer, which is absent for samples with denser grains with less/ no pores. This is in agreement with the density of the sample *vs* Cu doping in BCN **Figure 4.5** calculated from the Rietveld refinement analysis, where the density is low for samples with Cu-doping in Nb-site than the Cu-doped in Ca-site. For comparison purposes, the average density for x = 0.13 and x = 0.26 (in Nb-site) in both phases was used. The presence of multiples phases in increased Cu content (in Nb-site) has influenced the porosity, morphology of the samples

and their respective density. These findings provide beneficial information for their correlation with physical properties of the BCN perovskite.

4.2.2 Chemical stability

The chemical stability of the double perovskites was studied in pure CO_2 at 600 ˚C for 72 h and in moisture content from boiling water (~100 ˚C) for 72 h. PXRD patterns shows no significant structural changes in the pattern after CO_2- (**Figure 4.6(a)**) for all Cu-BCN samples, except for x = 0.26 Cu-doping with an impurity peak (denoted by $) which is due to formation of carbonates noticed only for high Cu-content that is aligned with the presence of mixed phases confirmed by the PXRD patterns shown in **Figures 4.1 and 4.2(d).** However, PXRD patterns of samples treated in moisture from boiling-water denotes no major structural changes that confirms the absence of moisture pickup by the prepared perovskites.

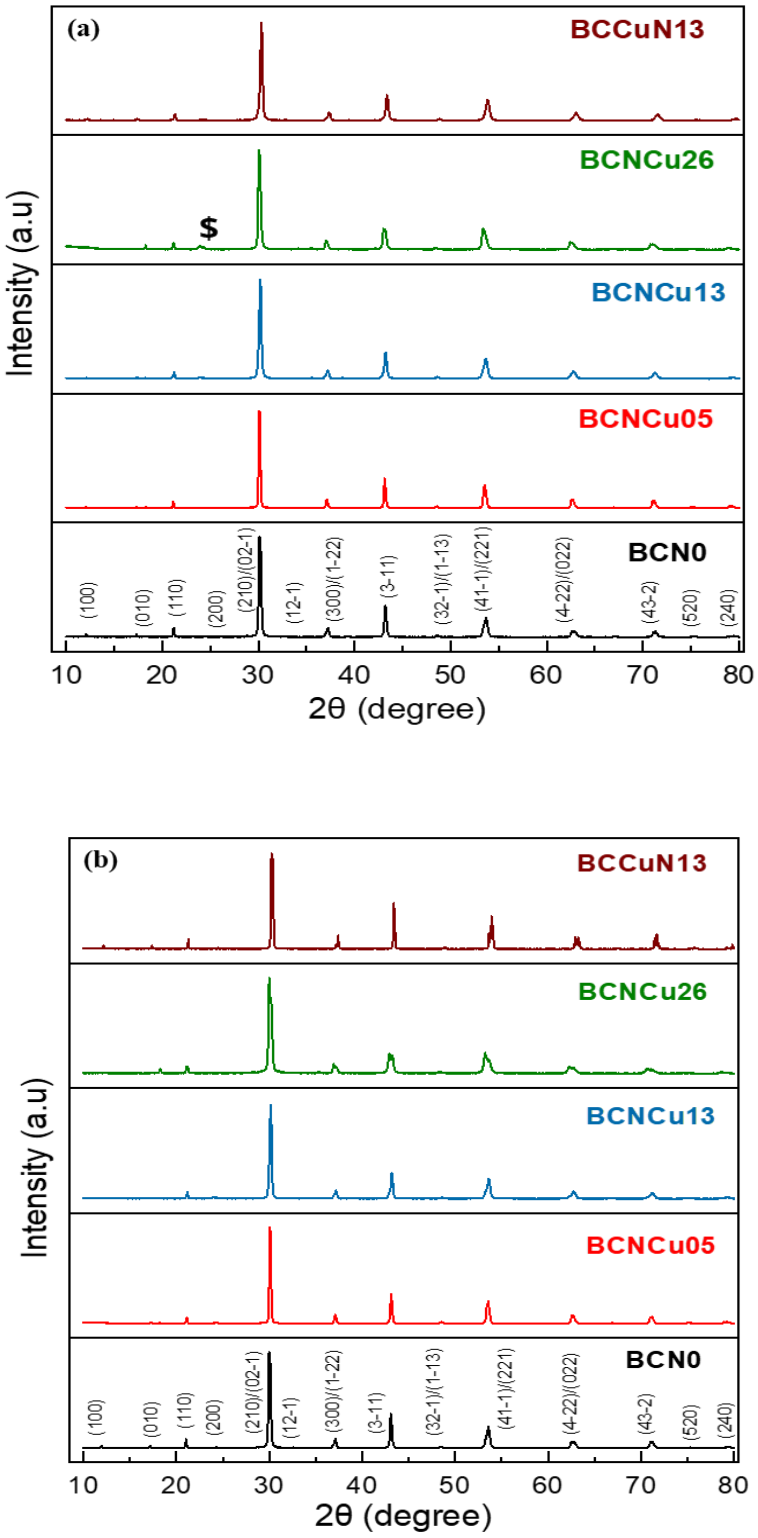

Figure 4.6 PXRD pattern of Cu-BCN samples treated in (a) pure CO_2 at 600 ˚C for 72h, and (b) in moisture from boiling water (~ 100 ˚C) for 72h.

Further analyses were drawn from FTIR spectra to identify the presence of carbonate (CO) and hydroxyl (OH) groups. Literature of several cerates and zirconates with their respective Ba analogues were proven to be reactive with CO_2 and moisture[175]. However, the Ba-containing BCN perovskite oxides supresses the reactivity, which is further improved by substitution of foreign atoms and thereby improving the performance and lifetime of the material composite[176]. **Figure 4.7** shows the FTIR of as-prepared, CO_2- and moisture-treated $Ba_2Ca_{0.67}Nb_{1.33-x}Cu_xO_{6-\delta}$ (x = 0, 0.05, 0.13 and 0.26) and $Ba_2Ca_{0.67-x}Cu_xNb_{1.33}O_{6-\delta}$ (x = 0.13). The FTIR spectrum of almost all compositions irrespective of the sample's treatment, shows small peaks near ~1500 cm^{-1} frequency related to the carbonate group which is due to the pickup of CO_2 from the environment while air-drying the samples prior characterization. From **Figure 4.7(a)**, for x = 0.26 Cu-content, the sharp peak at ~1500 cm^{-1} frequency is related to the carbonate group which is confirmed by the impurity peak from PXRD (Figure 4.6(a)). For samples treated in moisture from boiling water, the FTIR spectra shows no peak due to hydroxyl group at ~3500 cm^{-1} denoting that the Cu-BCN samples doesn't pick up moisture.

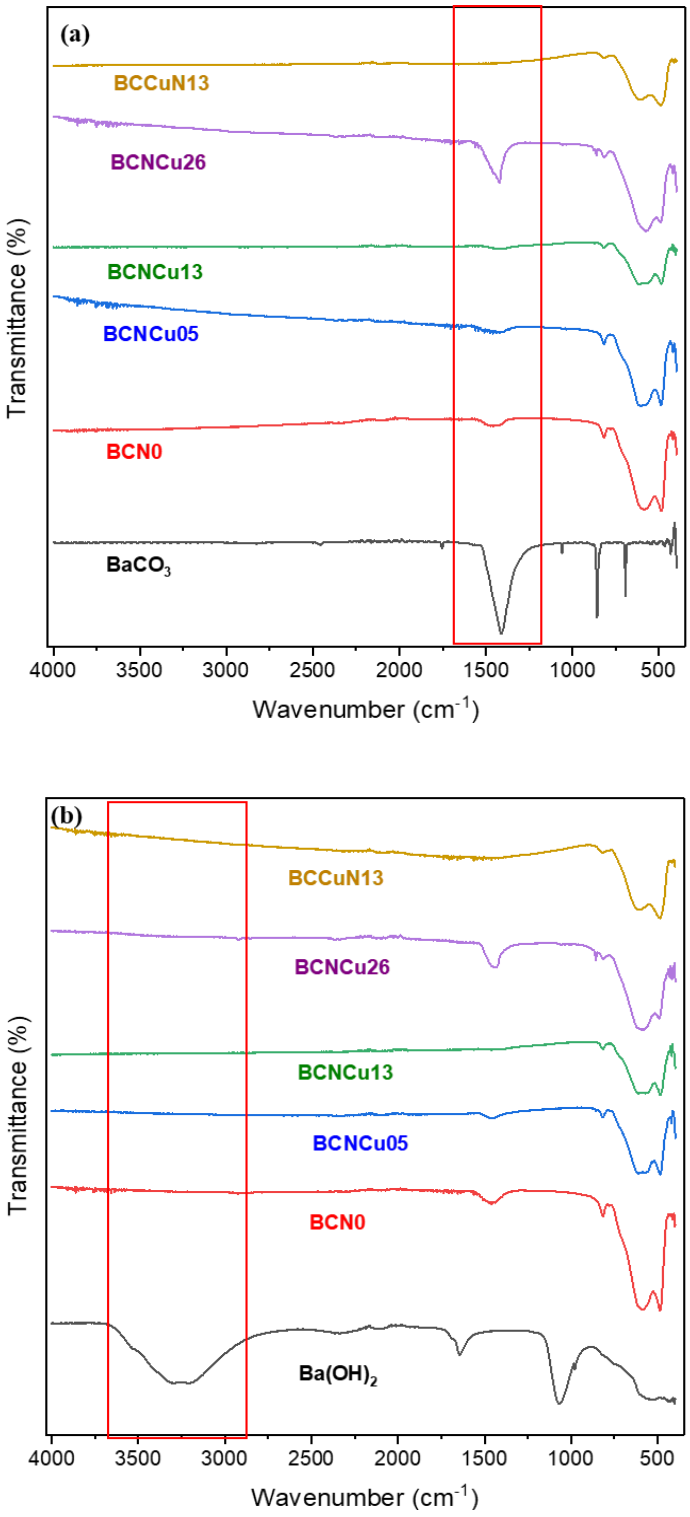

Figure 4.7 FTIR spectra of Cu-BCN samples treated in (a) pure CO_2 at 600 ˚C for 72 h, and (b) in moisture from boiling water (~ 100 ˚C) for 72 h, compared with the FTIR spectra of $BaCO_3$ and $Ba(OH)_2$.

Therefore, it is evident that the Cu-doping retains the chemical stability of the double perovskites, except for high Cu-content (x = 0.26) with mixed phase, unlike the transition metal-doped Ba-analogue perovskites reported in the literature[175,176].

4.2.3 Electrical properties

The electrical properties of the Cu-BCN double perovskites are elaborated in this section. **Figure 4.8** shows the schematic of the pellet sample used for impedance measurements.

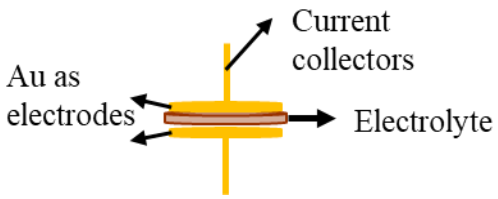

Figure 4.8 Schematic of the pellet sample used for impedance measurements. The two sides of the pellet were painted with gold paste that acts as current collectors. An AC is applied to both sides of the pellet over the frequency range of 10^{6} – 10^{-1} Hz with an amplitude of 100 mV.

The Nyquist plots of $Ba_2Ca_{0.67}Nb_{1.33-x}Cu_xO_{6-\delta}$ (x = 0, 0.05, and 0.13) and $Ba_2Ca_{0.67-x}Cu_xNb_{1.33}O_{6-\delta}$ (x = 0.13) in different medium are shown in **Figures 4.9 – 4.11**. The AC Impedance shows the contribution due to bulk and grain-boundary effects between the frequency range 10^{6} – 10^{-1} Hz. However, these contributions vary depending on the compositions, temperature, and the surrounding mediums, this trend can be seen in **Figures 4.9 – 4.11** that shows the Nyquist plots of $Ba_2Ca_{0.67}Nb_{1.33-x}Cu_xO_{6-\delta}$ (x = 0, 0.05, and 0.13) in different medium dry air and N_2, wetted N_2 with H_2O and D_2O. The isotope effect was studied using wetted N_2 with H_2O and D_2O, which can further explain the absence of proton conduction in the above studied materials:

$$D_2O + V_O^{\bullet\bullet} + O_O^x \rightarrow 2OD_O^{\bullet} \qquad (4.1)$$

where $OD_O^{\bullet}$ represents the deuterium attached to oxygen in the lattice.

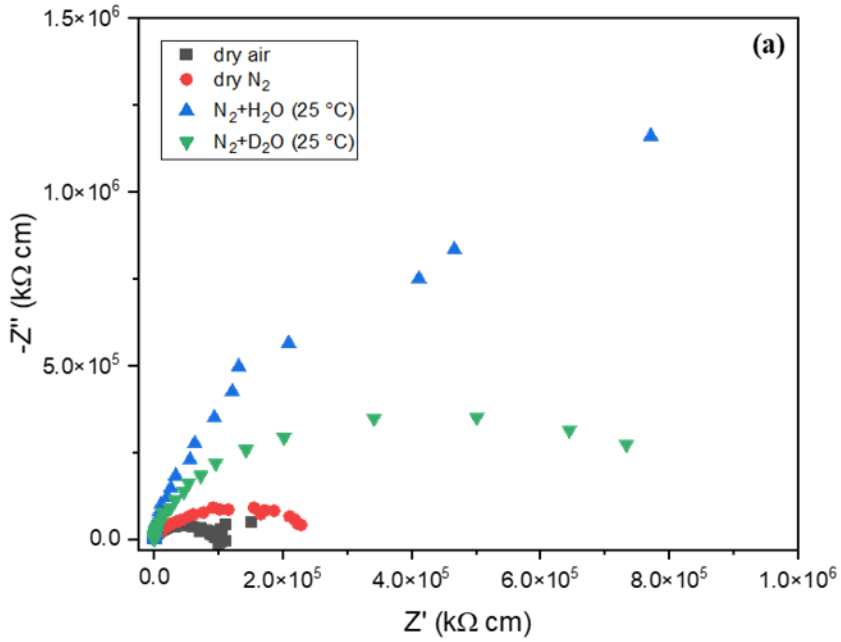

Figure 4.9 Nyquist plots of $Ba_2Ca_{0.67}Nb_{1.33}O_6$ at 600 ˚C, in air, dry N_2, N_2+H_2O (25 ˚C) and N_2+D_2O (25 ˚C), over the frequency range of 10^6 – 10^{-1} Hz and amplitude of 100 mV.

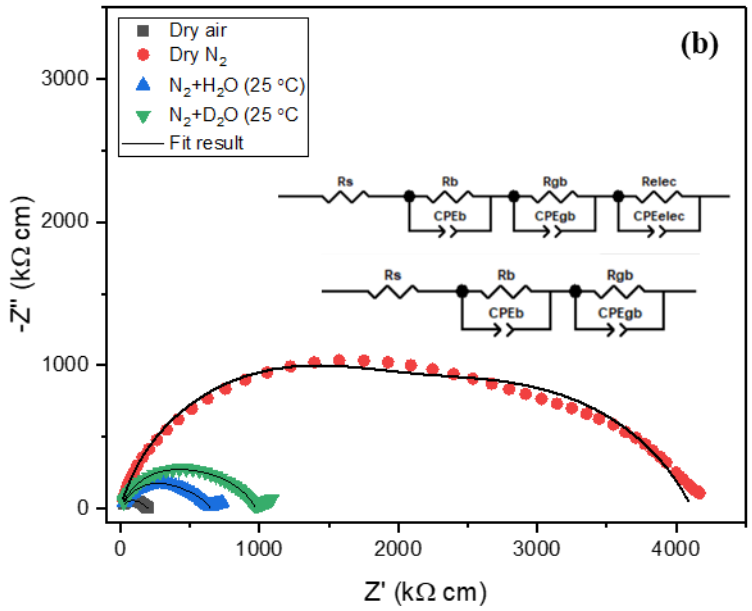

Figure 4.10 Nyquist plots of $Ba_2Ca_{0.67}Nb_{1.28}Cu_{0.05}O_{6-\delta}$ at 600 ˚C, in air, dry N_2, N_2+H_2O (25 ˚C) and N_2+D_2O (25 ˚C), over the frequency range of 10^6 – 10^{-1} Hz and amplitude of 100 mV; the solid black line passing through the Nyquist plot denotes the best fit line; the inset gives the equivalent circuits used for fitting the impedance data.

The absence of x-axis intercept in the Nyquist plot of undoped-BCN (**Figure 4.9**) in certain atmospheres, could be due to the poor contact of the current collectors with the surface of the sample. The impedance spectra of $Ba_2Ca_{0.67}Nb_{1.28}Cu_{0.05}O_{6-\delta}$ (**Figure 4.10**) shows high conductivity in wet N_2 (N_2+ H_2O) compared to that of conductivity in dry N_2, showing possible proton conduction for x = 0.05 Cu-content. However, this contradicts the absence of moisture pickup as shown in FTIR spectrum. Figure 4.10 also shows the fitting of the impedance curves using two different equivalent circuits containing constant phase element (CPE) and resistor (R), like the method in literature[156]. The real capacitance (C) for the semicircle in the fitted graphs were obtained from the resistance (R), pseudo-capacitance (Q), and an additional parameter (n) extracted from the equivalent fitting circuit using the equation[177,178].

$$C = R^{[\frac{1-n}{n}]}Q^{(\frac{1}{n})} \tag{4.2}$$

In these impedance plots, it can be noticed that the single semicircle appearing contains both bulk and grain boundary contributions altogether, which can be verified from the parameters that are summarised in **Table 4.3**, gives the calculated capacitance values for high frequency semicircle in the order of 10^{-11} F, which indicates the bulk conductivity contribution, and that of the second curve fitted is of 10^{-10} - 10^{-9} F indicating the grain boundary contribution. Interestingly, the impedance plot in ambient air, also shows contribution due to electrode response at low frequency range with capacitance value of 10^{-7} F.

Table 4.3 Fitting parameters of impedance plot of $Ba_2Ca_{0.67}Nb_{1.29}Cu_{0.05}O_{6-\delta}$ at 600 C in air, dry N_2, N_2+H_2O (25 ˚C) and N_2+D_2O (25 ˚C).

Medium	**R_b (Ω)**	**C_b (F)**	**n**	**R_{gb} (Ω)**	**C_{gb} (F)**	**n**	**R_{elec} (Ω)**	**C_{elec} (F)**	**n**
Air	8205	8.70×10^{-11}	0.86714	6343	6.21×10^{-10}	0.6807	2199	3.84×10^{-7}	0.35073
Dry N_2	154660	6.29×10^{-11}	0.85463	194630	8.50×10^{-10}	0.70643	-	-	-
N_2+H_2O	32250	8.63×10^{-11}	0.76493	21142	1.02×10^{-9}	0.76493	-	-	-
N_2+D_2O	39754	9.52×10^{-11}	0.78952	41100	5.03×10^{-9}	0.69184	-	-	-

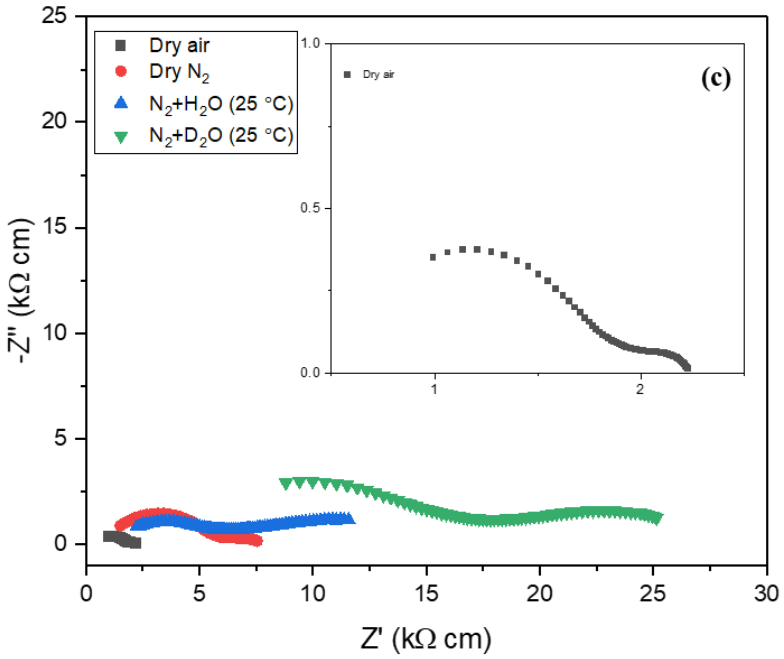

Figure 4.11 Nyquist plots of $Ba_2Ca_{0.67}Nb_{1.2}Cu_{0.13}O_{6-\delta}$ at 600 ˚C, in air, dry N_2, N_2+H_2O (25 ˚C) and N_2+D_2O (25 ˚C), over the frequency range of 10^6 – 10^{-1} Hz and amplitude of 100 mV.

However, the Nyquist plot of x = 0.13 Cu content (**Figure 4.11**), shows highest conductivity in air compared to that in dry N_2, denoting p-type hole conduction. The hole conduction becomes evident for the compositions with mixed phases unlike for x = 0.05 (with pure single phase). However, this hypothesis could be confirmed by further conductivity measurements by varying the pO_2, that could be considered for future studies.

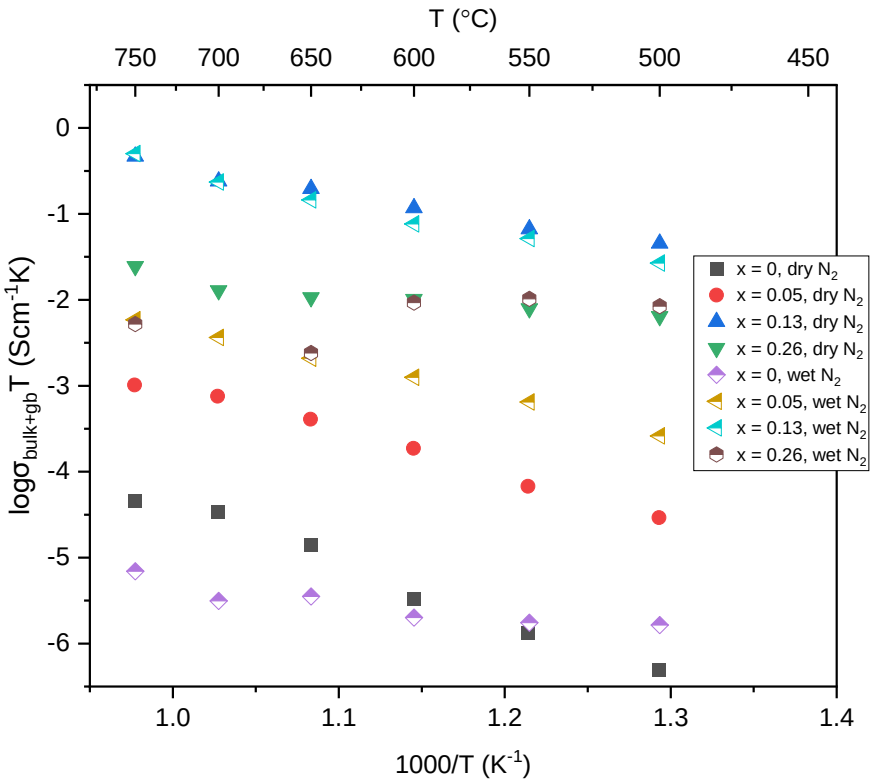

Figure 4.12 Arrhenius plots for bulk and grain boundary electrical conductivity of $Ba_2Ca_{0.67}Nb_{1.33-x}Cu_xO_{6-\delta}$ (x = 0, 0.05, 0.13 and 0.26) in dry N_2 and wet N_2 (N_2+H_2O – 25 ˚C), over the temperature range of 500 – 750 ˚C.

The fitting of the Nyquist plots was not carried out (for other Cu doping except x = 0.05) which shows no distinct semicircle and high values of errors for fitting curves due to the complex impedance spectra in different atmospheres varying for different Cu-contents. Thus, the total resistance ($R_{bulk} + R_{gb}$) for the impedance plots for all Cu-doping in Nb-site was considered for the total conductivity and to plot the Arrhenius curve. The detailed studies of these Nyquist plots are complicated as the spectrum seems to vary with atmosphere and temperature for the same composition, as evident from the morphology of these samples showing more porous and uneven particles that makes it difficult to distinguish the contribution towards the conductivity. It is evident

from literature[179] that proton conduction in the BCN-type double perovskites is seen at intermediate temperature range (400 – 600 ˚C).

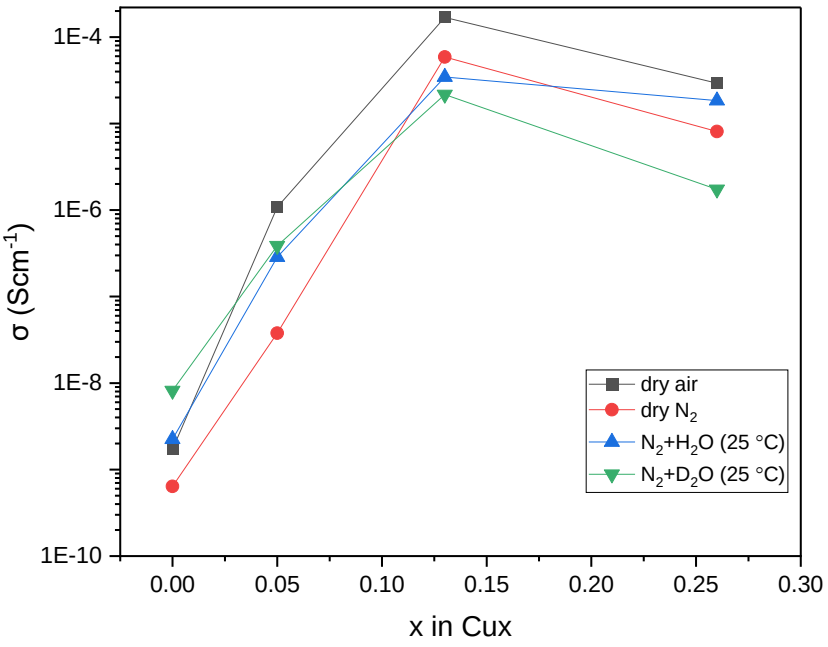

Figure 4.13 The total (bulk + grain boundary) conductivities of $Ba_2Ca_{0.67}Nb_{1.33-x}Cu_xO_{6-\delta}$ (x = 0, 0.05, 0.13 and 0.26) at 600 ˚C in different medium dry air and N_2, wetted N_2 with H_2O (25 ˚C) and D_2O (25 ˚C). The conductivity seems to increase with Cu content, except for x = 0.26 shows deviation from the trend.

Figure 4.13 reveals the highest calculated conductivity of 4.6×10^{-4} Scm^{-1} in dry air at 600 ˚C exhibited by $Ba_2Ca_{0.67}Nb_{1.2}Cu_{0.13}O_{6-\delta}$ (x = 0.13). The Arrhenius plot for x = 0.26 (in air and wet N_2 medium) seems to vary from the trend at higher temperatures (700 – 750 ˚C), which can be attributed to the formation of secondary phases in their crystal structure and can be explained by the formation of carbonates as observed in the FTIR (**Figure 4.6(d)**) after CO_2-treatment, that contributes towards the poor conductivity of the Cu-BCN samples. **Table 4.3** summarises the conductivities (at 600 ˚C) of all compositions in different mediums for all Cu-concentrations.

*Table 4**Error! No text of specified style in document.**..4 Summary of total (bulk + grain boundary) conductivities (at 600 ˚C) of all compositions in dry air, dry N_2, N_2+H_2O (25 ˚C) and N_2+D_2O (25 ˚C).*

x in Cux	Conductivity, $\sigma_{bulk+gb}$ (S/cm)			
	Dry air	**Dry N_2**	**N_2+H_2O**	**N_2+D_2O**
0	1.0×10^{-8}	3.8×10^{-9}	2.4×10^{-9}	1.6×10^{-9}
0.05	4.3×10^{-6}	2.1×10^{-7}	1.2×10^{-6}	9.1×10^{-7}
0.13	4.6×10^{-4}	1.3×10^{-4}	8.8×10^{-5}	4.0×10^{-5}
0.26	5.8×10^{-5}	1.2×10^{-5}	2.1×10^{-5}	1.1×10^{-6}

Considering Cu_x = 0.13 in Nb-site, $Ba_2Ca_{0.67}Nb_{1.2}Cu_{0.13}O_{6-\delta}$ composition, with highest conductivity among all other Cu-doping, a comparison was made with $Ba_2Ca_{0.54}$ $Cu_{0.13}Nb_{1.33}O_{6-\delta}$ (Cu_x = 0.13 in Ca-site), to study the influence of different site doping. The Cu doping in Nb shows still shows highest conductivity irrespective of the medium, compared to that of Cu doping in Ca (**Table 4.5**).

Table 4.5 Summary of structural and electrical properties of Cu-doped in Nb- vs Ca-site in $Ba_2Ca_{0.67}Nb_{1.33}O_6$.

Composition	**Ca/Nb ratio**	**Space group**	**Conductivity, $\sigma_{bulk+gb}$ (S/cm)**	
			Dry air	**N_2+H_2O**
$Ba_2Ca_{0.67}Nb_{1.2}Cu_{0.13}O_{6-\delta}$	0.6	$P\bar{3}m1$	4.6×10^{-4}	8.8×10^{-5}
$Ba_2Ca_{0.54}Cu_{0.13}Nb_{1.33}O_{6-\delta}$	0.41	$Fm\bar{3}m$	3.0×10^{-5}	4.2×10^{-5}

From **Table 4.5**, it can be noted that Cu-doping in Nb-site yields higher conductivity in dry air than in wet N_2, denoting the absence of proton conduction in humid atmosphere. It should also be noted that the doping in different atoms within B-site proves to influence the electrical conductivity and the resistance due to various contributions. Their structural properties also play a major role in determining their respective physical properties, Kan *et al.,*[171] has summarised that change in the Ca/Nb ratio (B-site) proves to influence the structure of the double perovskites, when the Ca/Nb ratio is larger, it favours the formation of double perovskites with $P\bar{3}m1$ space group, and when the ratio is smaller, then double perovskites with $Fm\bar{3}m$ space group is formed (**Table 4.5**). The conductivity of $Ba_2Ca_{0.67}Nb_{1.2}Cu_{0.13}O_{6-\delta}$ in wet medium (N_2+H_2O (25 ˚C)) is compared with other Ba-based perovskite oxides from literature under similar same environment (**Figure 4.14**), which denotes that the current studied materials exhibit proton conduction which is comparable to that of reported literature values[101,103].

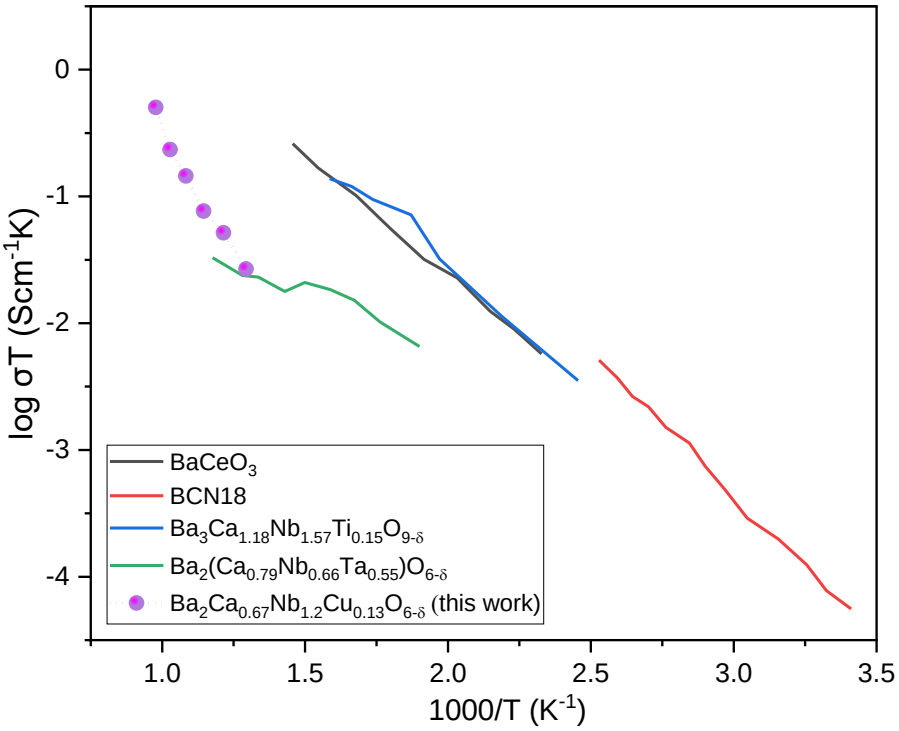

Figure 4.14 Comparison of conductivity of $Ba_2Ca_{0.67}Nb_{1.2}Cu_{0.13}O_{6-\delta}$ (current work) in wet medium (N_2+H_2O (25 ˚C)) with other proton conducting Ba-based perovskite oxides, $BaCeO_3$[180], $Ba_3Ca_{1.18}Nb_{1.82}O_{9-\delta}$ (BCN18)[81], $Ba_3Ca_{1.18}Nb_{1.57}Ti_{0.15}O_{9-\delta}$[103], and $Ba_2(Ca_{0.79}Nb_{0.66}Ta_{0.55})O_{6-\delta}$[101].

4.3 Summary

The PXRD studies of transition metal-doped double perovskite-type $Ba_2Ca_{0.67}Nb_{1.33-x}Cu_xO_{6-\delta}$ (x = 0, 0.05, 0.13 and 0.26) and $Ba_2Ca_{0.67-x}Cu_xNb_{1.33}O_{6-\delta}$ (x = 0.13) indicated that all the prepared compounds crystallize in cubic structure with a $P\bar{3}m1$ space group along with the presence of a secondary phase in a $Fm\bar{3}m$ space group for compositions with high Cu-content. These materials also exhibited good chemical stability in CO_2-treated samples, except for high Cu-doping (x = 0.26) and that for moisture-treated samples shows no moisture pickup. The surface morphology showed the uniform distribution of particles with presence of grain-boundary that supported the conductivity values observed during impedance measurements. Among all the compositions

studied, $Ba_2Ca_{0.67}Nb_{1.2}Cu_{0.13}O_{6-\delta}$ showed highest conductivity of 4.6×10^{-4} Scm^{-1} in dry air than in dry N_2 at 600 ˚C, denoting p-type hole conduction, which consists of holes (electronic charges) as charge carriers contributing towards the conductivity. Further, the same composition had comparable conductivity in humid medium (8.8×10^{-5} Scm^{-1} in wet N_2 at 600 ˚C) is comparable to that with literature $Ba_3Ca_{1.18}Nb_{1.57}Ti_{0.15}O_{9-\delta}$, and $Ba_2(Ca_{0.79}Nb_{0.66}Ta_{0.55})O_{6-\delta}$. For $Ba_2Ca_{0.67}Nb_{1.2}Cu_{0.13}O_{6-\delta}$, the conductivity is higher in wet N_2 than in dry N_2, denoting possible proton conduction (500 – 750 ˚C), which is contradictory to their limiting to moisture pickup.

Chapter 5 Dielectric studies of transition metal-doped double perovskite-type $Ba_2Ca_{0.67}Nb_{1.33-x}Cu_xO_6$ (x = 0, 0.05, 0.13 and 0.26) oxides

5.1 Introduction

In general, it was observed that materials that exhibit poor conductivities show better dielectric properties that are favourable for application in microwave dielectric radiators and energy storage devices like capacitors. Since the conductivity of the studied Cu-doped double perovskite-type $Ba_2Ca_{0.67}Nb_{1.33}O_6$ (BCN) oxides are lower compared to that of other doped perovskites, this opens the possibility of better dielectric properties of these perovskites. Other factors that influence the dielectric properties of these materials are sintering temperature, microstructure of the crystalline pellet sample, experimental conditions, and frequency range. Most of the common dielectric studies reported are carried out with AC impedance between the frequency range of $10^7 – 10^{-1}$ Hz[181,182] at low temperatures. However, few materials are studied at high temperature due to large dielectric losses, and especially to elucidate the bulk, grain boundary and electrode contributions using impedance measurements. In this chapter, the dielectric properties of Cu-doped $Ba_2Ca_{0.67}Nb_{1.33}O_6$ (BCN) are studied using AC impedance spectroscopy. The synthesis and physical characterization of these materials are discussed in Chapter 4, along with their electrical conductivity. This chapter explains the influence of electrical properties (conductivity, σ) over dielectric properties, namely, dielectric constant (ε′), dielectric loss (tan δ), modulus (M”) as a function of frequency (log *f*).

5.2 Results and discussion

5.2.1 Dielectric properties

The electrical and dielectric properties relationship of double perovskite-type $Ba_2Ca_{0.67}Nb_{1.33-x}Cu_xO_6$ (x = 0, 0.05, 0.13 and 0.26) oxides synthesized and characterized in chapter 4 are evaluated in the current chapter. **Figure 5.1** shows typical impedance plots for Cu-BCN in dry air, dry N_2, N_2+H_2O (25 ˚C) and N_2+D_2O (25 ˚C) at 500 ˚C.

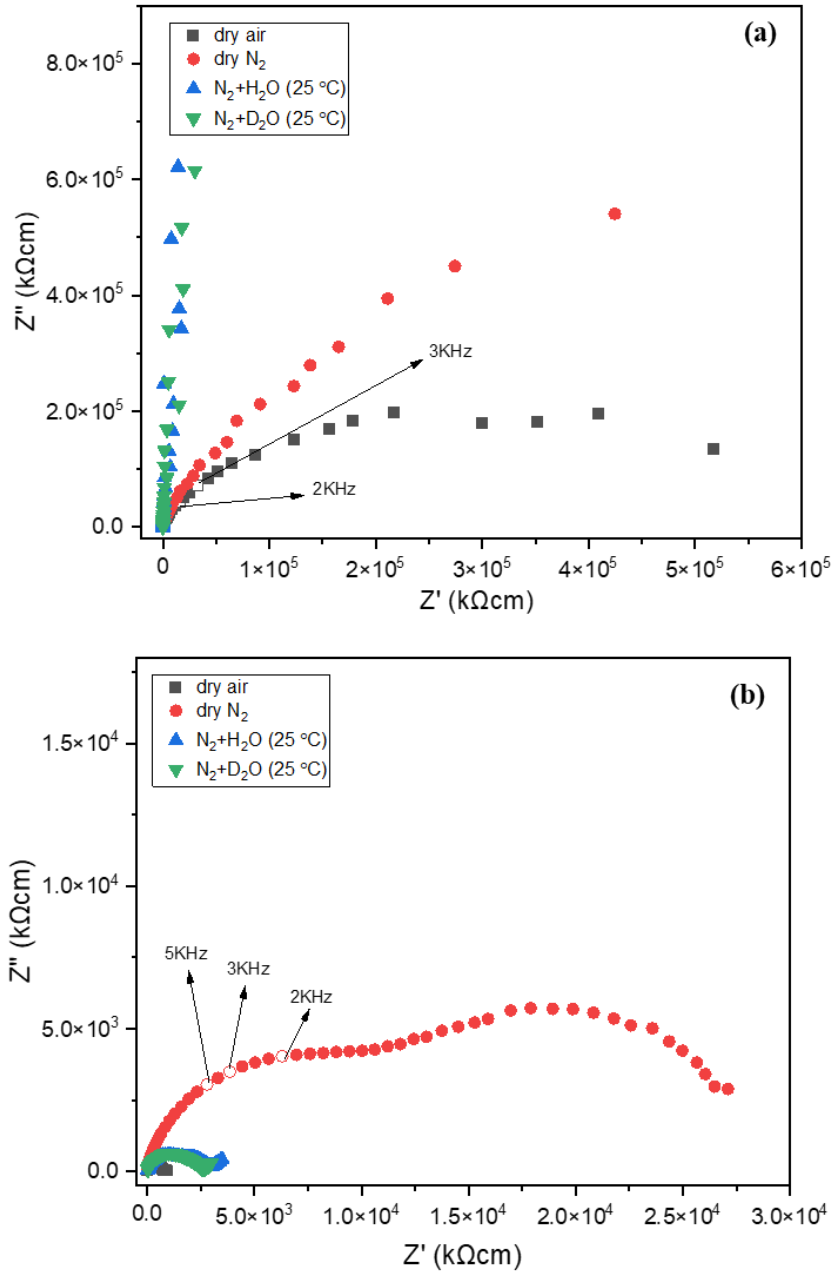

Figure 5.1 Nyquist plots of (a) $Ba_2Ca_{0.67}Nb_{1.33}O_6$ and (b) $Ba_2Ca_{0.67}Nb_{1.28}Cu_{0.05}O_{6-\delta}$ at 600 ˚C, in air, dry N_2, N_2+H_2O (25 ˚C) and N_2+D_2O (25 ˚C), over the frequency range of 10^6 – 10^{-1} Hz and amplitude of 100 mV.

Substitution of Cu_x decreases the grain-boundary contribution from x = 0.05 to 0.26, compared to un-doped $Ba_2Ca_{0.67}Nb_{1.33}O_6$ (BCN). The appearance of low frequency intercept at the x-axis denotes the non-blocking nature of the electrode[183,184]. From the impedance data, the dielectric constant was calculated using the expression given in chapter 3 (**equation 3.5**) and plotted against frequency in **Figures 5.3(a) and (b)**. The scattered points at lower frequency for x = 0 (**Figures 5.3(a) and (b)**) denotes the poor contact of current collectors with the sample. The region at high and low frequency is attributed to the contribution due to bulk and grain-boundary contributions. For any material to possess alluring dielectric properties, their dielectric constant should be higher and dielectric loss should be less at any frequency. The dielectric constant increases with increase in Cu concentration, however, deviates for Cu_x = 0.26 which can be due to the presence of mixed phases. This can be related with the lowering of structural symmetry (from trigonal to cubic) on increasing Cu doping which increases the dielectric loss and decreases the dielectric constant, which is in agreement with literature[185].

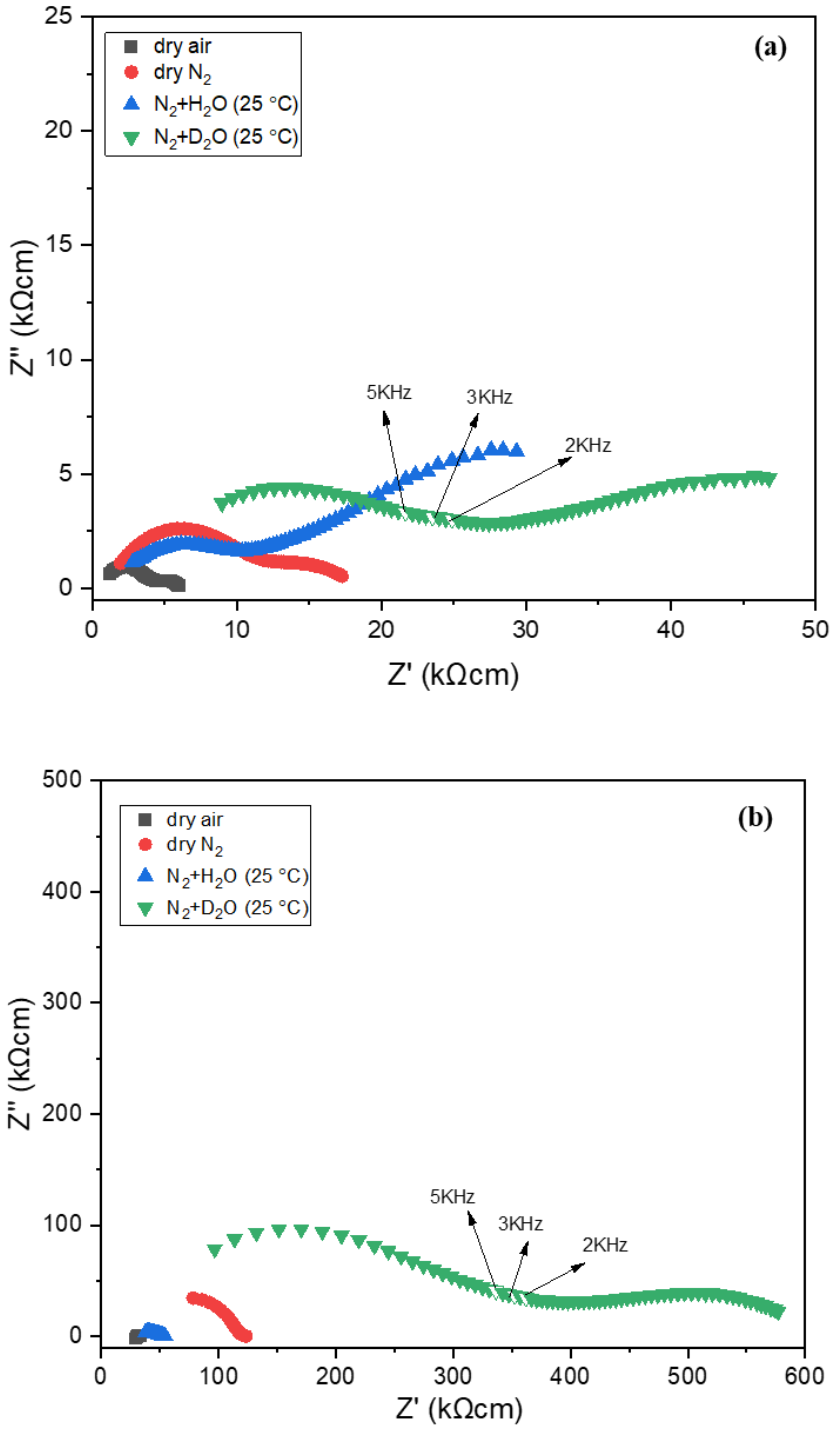

Figure 5.2 Nyquist plots of (a) $Ba_2Ca_{0.67}Nb_{1.2}Cu_{0.13}O_{6-\delta}$ and (b) $Ba_2Ca_{0.67}Nb_{1.07}Cu_{0.26}O_{6-\delta}$ at 600 ˚C, in air, dry N_2, N_2+H_2O (25 ˚C) and N_2+D_2O (25 ˚C), over the frequency range of 10^6 – 10^{-1} Hz and amplitude of 100 mV.

Figures 5.3(a) and (b), which denotes that Cux (x = 0.05 and 0.13) shows better dielectric properties (high ε′ and low tan δ) and follows the trend uniformly throughout the frequency range. It should also be noted that the presence of secondary phases at higher Cu content (x = 0.26) suppresses the dielectric properties, which stays consistent with their electrical properties. Low dielectric constant at high frequency might be due to different ion polarization reactions happening due to the distortion of the structure of the material because of the displacement of the metal ions.

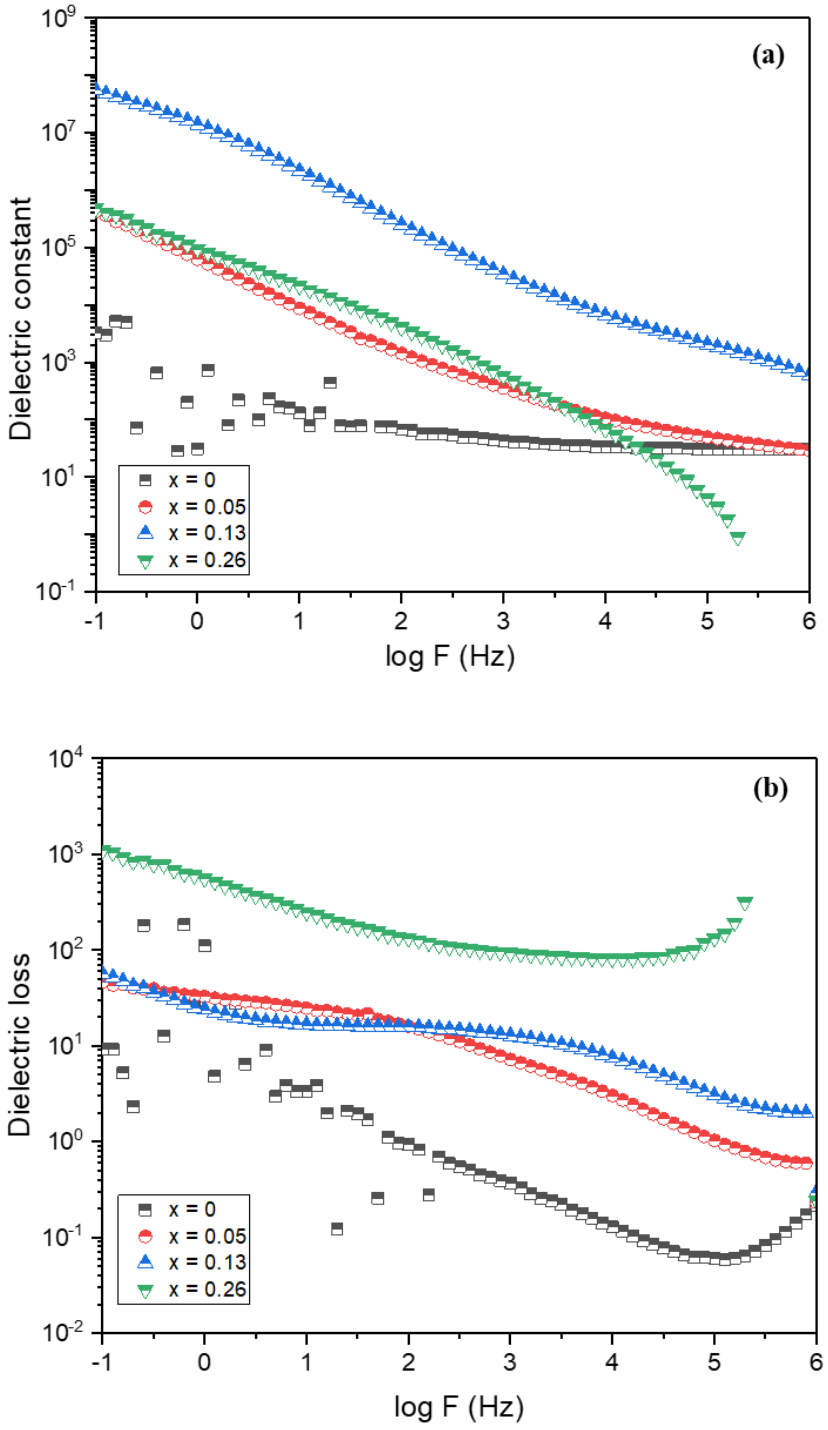

Figure 5.3 Variation of (a) dielectric constant, and (b) dielectric loss as a function of frequency for $Ba_2Ca_{0.67}Nb_{1.33}O_6$ (x = 0, black), $Ba_2Ca_{0.67}Nb_{1.28}Cu_{0.05}O_{6-\delta}$ (x = 0.05, red), $Ba_2Ca_{0.67}Nb_{1.2}Cu_{0.13}O_{6-\delta}$ (x = 0.13, blue) and $Ba_2Ca_{0.67}Nb_{1.07}Cu_{0.26}O_{6-\delta}$ (x = 0.26, green) at 500 ˚C in air.

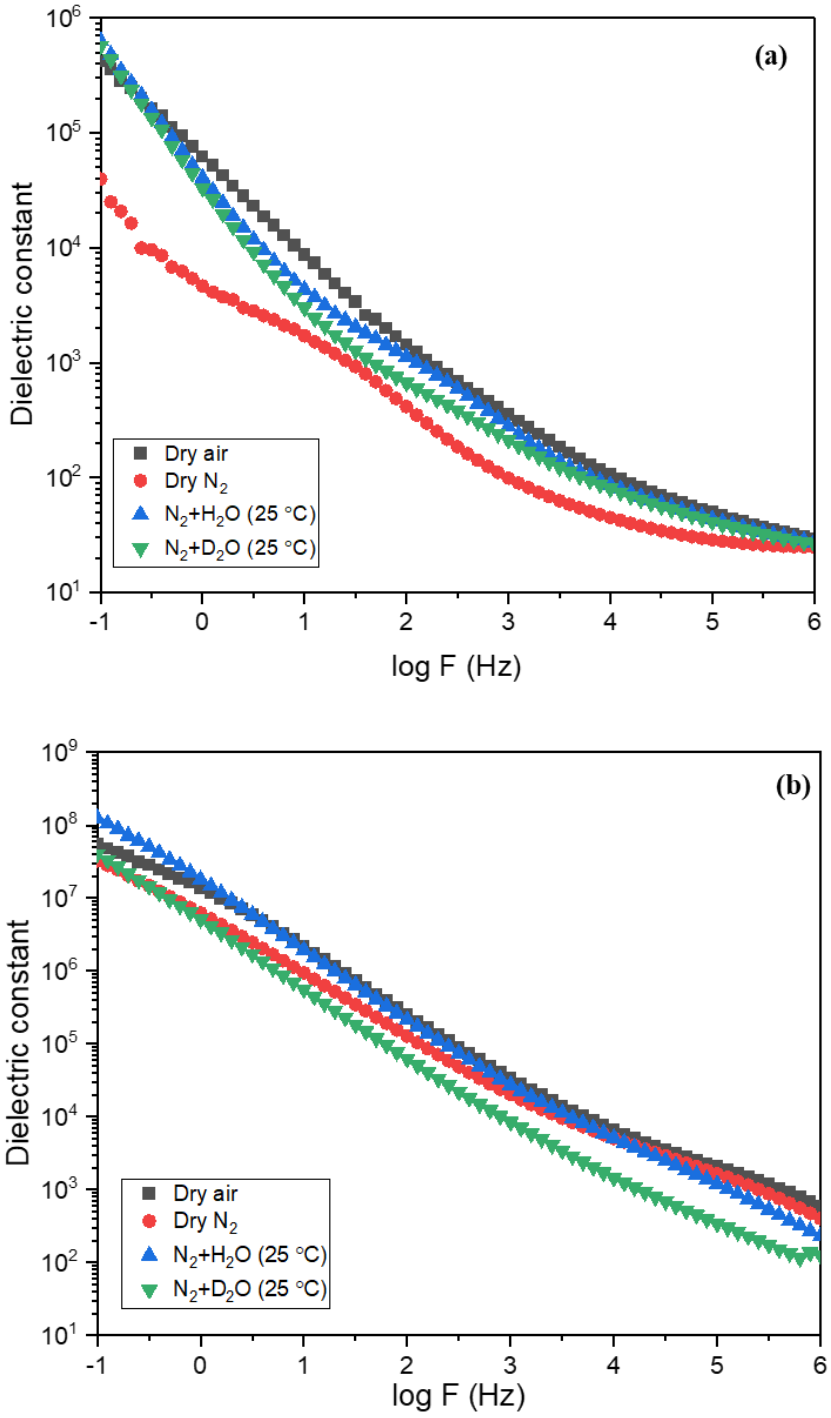

Figure 5.4 Variation of dielectric constant (ε') as a function of frequency at 500 ˚C in dry air, dry N_2, N_2+H_2O (25 ˚C) and N_2+D_2O (25 ˚C) for (a) $Ba_2Ca_{0.67}Nb_{1.28}Cu_{0.05}O_{6-\delta}$ (x = 0.05), and (b) $Ba_2Ca_{0.67}Nb_{1.2}Cu_{0.13}O_{6-\delta}$ (x = 0.13).

Similar behaviour was observed for the dielectric constant of x = 0.05 and 0.13 in different atmospheres (**Figures 5.4(a) and (b)**). The dielectric constant remains almost same irrespective of different mediums, with high dielectric constant at low frequency which is due to the accumulated charges between the grains and near the sample-electrode surface. This accumulation of charges is compared to the porous nature of these samples. Similarly, lower dielectric constant values at high frequency are attributed to the aligned vibrations (rotational frequency) of the molecules with the external signalling frequency[132,185].

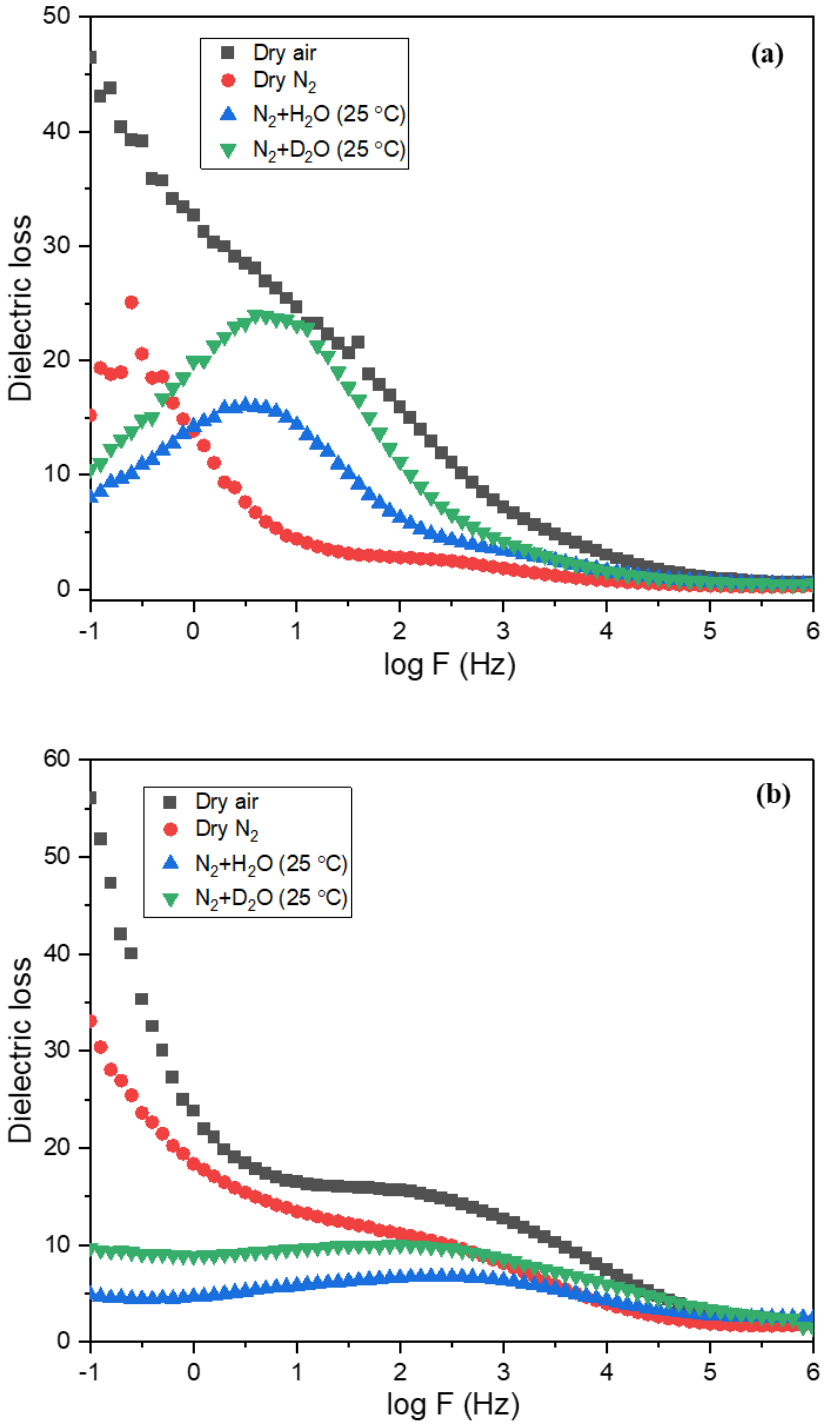

Figure 5.5 Variation of dielectric loss (tan δ) as a function of frequency at 500 ˚C in dry air, dry N_2, N_2+H_2O (25 ˚C) and N_2+D_2O (25 ˚C) for (a) $Ba_2Ca_{0.67}Nb_{1.28}Cu_{0.05}O_{6-\delta}$ (x = 0.05), and (b) $Ba_2Ca_{0.67}Nb_{1.2}Cu_{0.13}O_{6-\delta}$ (x = 0.13).

However, the high dielectric loss of the compositions (**Figures 5.5(a) and (b)**) at lower frequency is due to the reason of delay in vibration of the electronic species in these molecules that causes dielectric relaxation. When the electronic species in the molecules align with the applied electric field at high frequency, causes lowering of dielectric loss. Peak maxima were observed for certain atmospheres, at low frequency range of 10^{-1} – 10^{2} Hz for x = 0.05 (**Figure 5.5(a)**) and between 10^{2} – 10^{4} Hz for x = 0.13 (**Figure 5.5(b)**). However, the dielectric loss *vs* frequency does not provide clear peaks that makes it difficult to calculate the relaxation time and migration energy of the charges. Literature states that the peaks observed in the modulus *vs* frequency plot denotes the charge migration and hopping process that happens within the lattice[186].

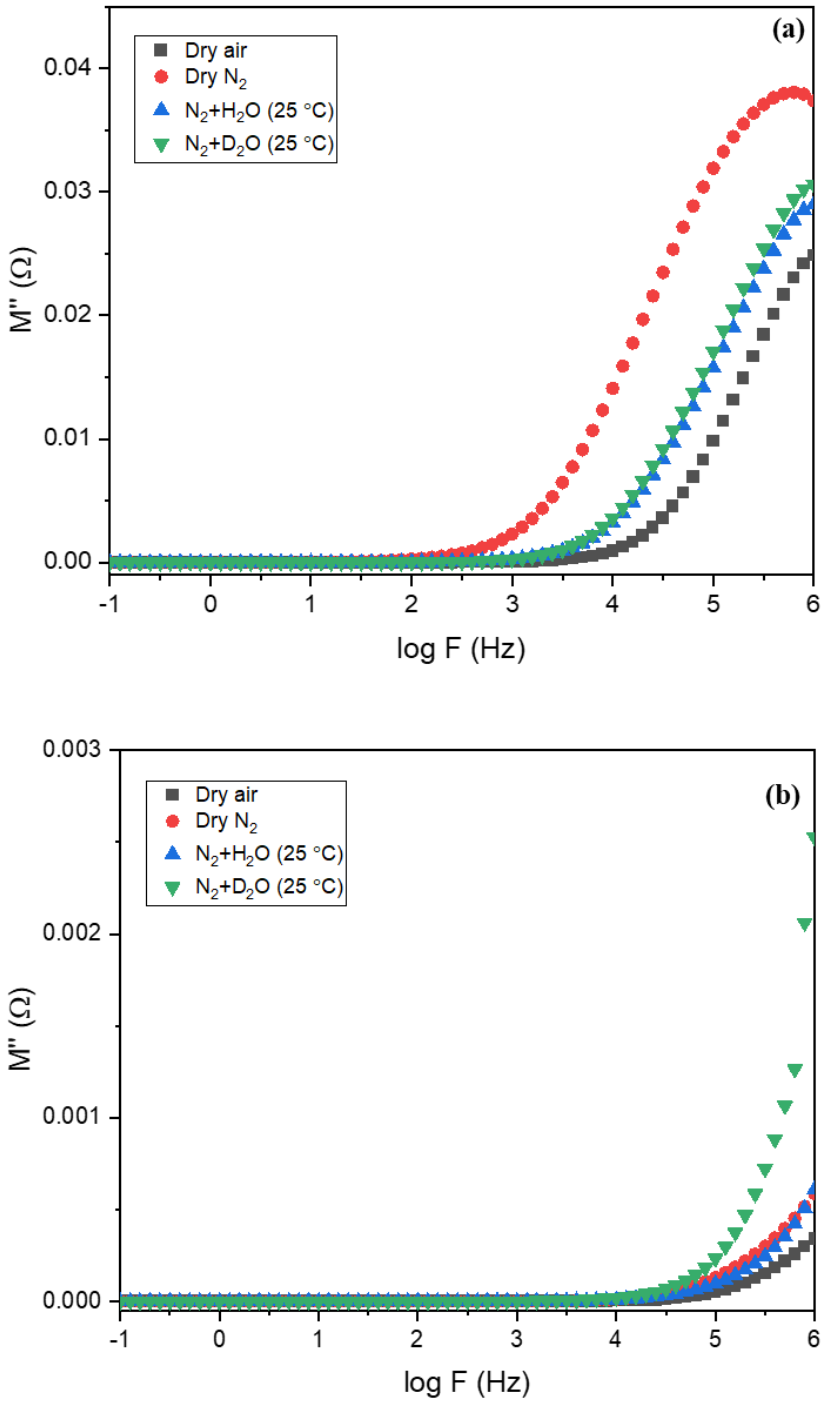

Figure 5.6 Variation of elastic modulus (M'') as a function of frequency at 500 ˚C in different medium for (a) $Ba_2Ca_{0.67}Nb_{1.28}Cu_{0.05}O_{6-\delta}$, and (b) $Ba_2Ca_{0.67}Nb_{1.2}Cu_{0.13}O_{6-\delta}$.

Further analysis includes electric modulus M" *vs* frequency, have no peak maxima over the studied frequency range (**Figures 5.6(a) and (b)**). However, at higher frequency (> 10^6 Hz) the peak maximum could be expected which is evident from the plateau in the frequency region 10^4 – 10^6 Hz. **Table 5.1** lists the dielectric properties of the investigated Cu-BCN over various atmosphere at 500 ˚C.

Table 5.1 Summary of dielectric properties of Cux-doped BCN (x = 0, 0.05, 0.13 and 0.26) at 500 ˚C in different atmospheres at 10^6 Hz.

x in Cux	***Dielectric constant***				***Dielectric loss***			
	Dry air	***Dry N_2***	***N_2+H_2O***	***N_2+D_2O***	***Dry air***	***Dry N_2***	***N_2+H_2O***	***N_2+D_2O***
0	31	33	31	30	0.22	0.23	0.08	0.21
0.05	29	25	27	26	0.61	0.29	0.51	0.48
0.13	587	402	231	126	2.0	1.80	2.47	1.46
0.26	4	8	3	7	13.67	2.28	10.39	1.23

Figures 5.7(a) and (b) shows the temperature dependence of $Ba_2Ca_{0.67}Nb_{1.28}Cu_{0.05}O_{6-\delta}$ (x = 0.05) and $Ba_2Ca_{0.67}Nb_{1.2}Cu_{0.13}O_{6-\delta}$ (x = 0.13) with conductivity, dielectric constant and dielectric loss at 10^6 Hz. The relationship between electrical conductivity and dielectric constant seems to be unrelated however, it varies with the composition, structure, temperature, and atmosphere.

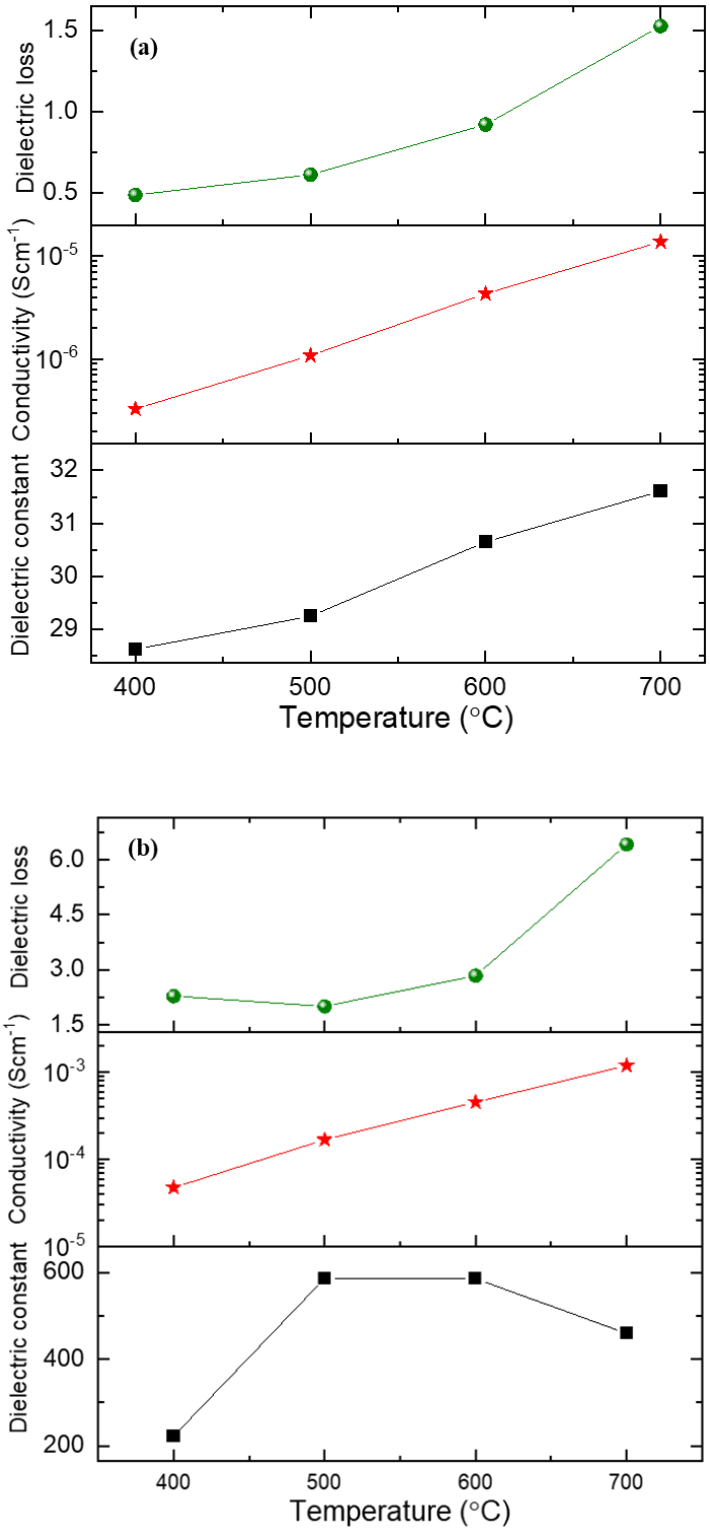

Figure 5.7 Dielectric constant, electrical conductivity, and dielectric loss of (a) $Ba_2Ca_{0.67}Nb_{1.28}Cu_{0.05}O_{6-\delta}$ (x = 0.05), and (b) $Ba_2Ca_{0.67}Nb_{1.2}Cu_{0.13}O_{6-\delta}$ (x = 0.13) in air at 400 – 700 ˚C at 10^6 Hz.

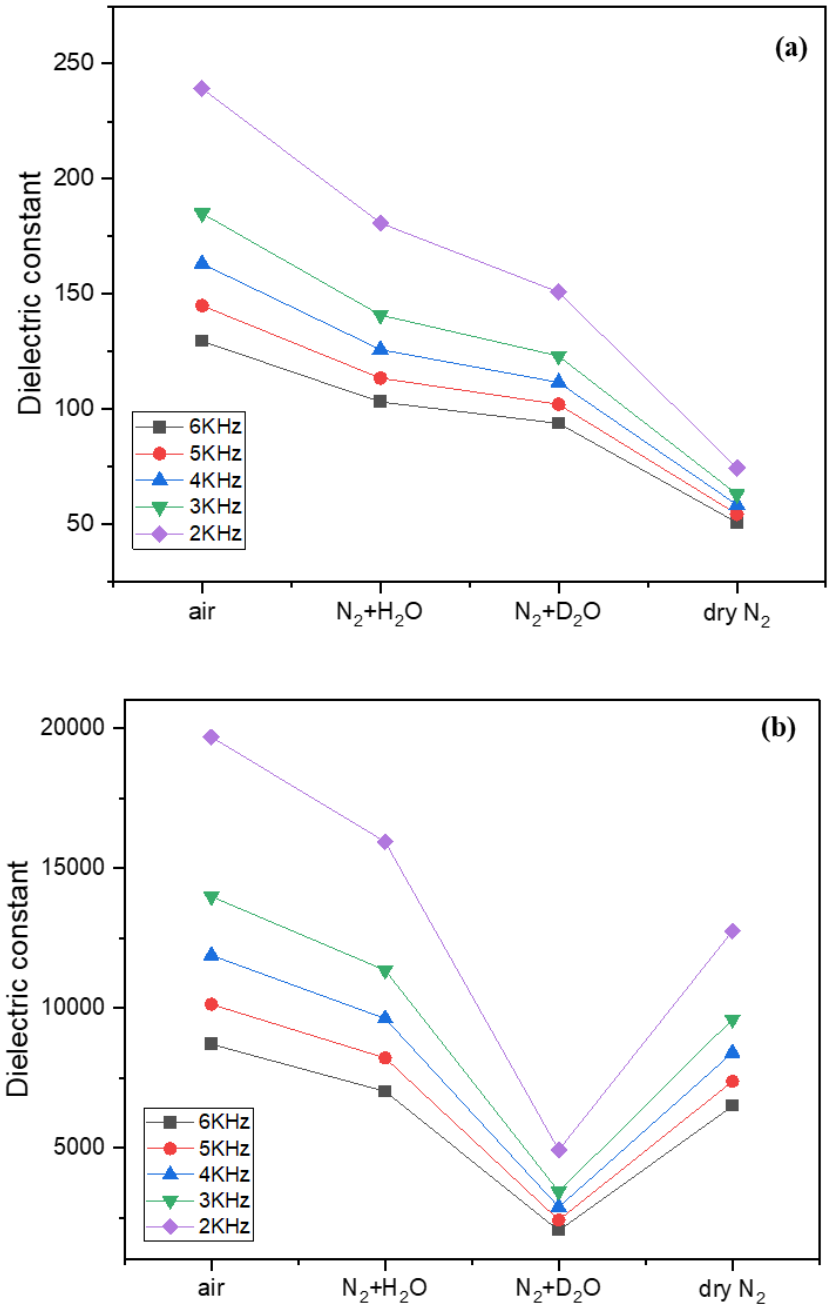

Figure 5.8 Variation of dielectric constant under different atmosphere at certain frequencies at 500 ˚C of (a) $Ba_2Ca_{0.67}Nb_{1.28}Cu_{0.05}O_{6-\delta}$ (x = 0.05), and (b) $Ba_2Ca_{0.67}Nb_{1.2}Cu_{0.13}O_{6-\delta}$ (x = 0.13).

The current work does not hold the dielectric properties due to other factors like, sintering conditions, density, and porosity, which influence the dielectrics of the BCN family as reported by several authors[184,186–188]. From **Table 5.2** and **Figures 5.8(a) and (b)**, it is observed that the

dielectric constant and dielectric loss remains the same in all medium[189] denoting that the dielectric properties are not limited by different atmospheres, especially at high frequency which is more oriented towards application in varying microwave dielectric devices. The high dielectric loss and low dielectric constant of the composition x = 0.26 is pointed towards the structural aspects of the material, which has significant amount of a secondary phase (**Figure 4.2**). The in-depth analysis of the dielectric properties is further required as future work over wider frequency range helps in understanding the migration energy and contribution of responsible mobile charge carriers.

5.3 Summary

The relationship between electrical and dielectric properties of Cux-BCN (x = 0, 0.05, 0.13 and 0.26) provides an insight into the probability of utilising these family for materials for multiple applications. AC Impedance spectroscopy method was applied in the current work to elucidate the dielectric studies for the synthesized materials. Among the investigated samples, the highest dielectric constant exhibited by $Ba_2Ca_{0.67}Nb_{1.2}Cu_{0.13}O_{6-\delta}$ (x = 0.13) was 587 and dielectric loss of 2 at 10^6 Hz at 500 ˚C in air. In general, $Ba_2Ca_{0.67}Nb_{1.2}Cu_{0.13}O_{6-\delta}$ (x = 0.13) shows highest dielectric constant values in the range of ~100 – 600 and lowest dielectric loss exhibited by $Ba_2Ca_{0.67}Nb_{1.28}Cu_{0.05}O_{6-\delta}$ (x = 0.05) was ~0.3 – 0.6 at 500 ˚C in various atmospheres. The dielectric constant and electrical conductivity is independently varying at higher frequencies. The dielectric studies of the synthesized Cu-BCN opens a lot of opportunities in the field of dielectrics by fine tune the existing fixtures, however, the complex impedance spectra limit the further analysis of the materials into determining the relaxation time, migration energy of the charge carriers present in the material.

Chapter 6 Structural and electrical properties of multi-element doped $Ba(Y_{1/2}Nb_{1/2})O_3$ perovskite oxides.

6.1 Introduction

Recent years witnessed the use of lead-free ternary perovskite type $Ba(Y_{1/2}Nb_{1/2})O_3$ for application in various electronic and microelectronic devices, after first reported by Brixner *et al*[190]. These materials are well known for their application in Since then, several attempts have been made to understand the dopants, structural and electrical properties of these classes of materials[191–193]. Several literatures have reported the cation ordering and microwave dielectric properties of $Ba(M_{1/2}Nb_{1/2})O_3$ (M = Co, Y, Yb, Nd)[138,194–197]. The disordering of these perovskites crystallizing in primitive cubic system makes them an appealing candidate for further studies of the influence of dopant strategy in structural and electrical properties. It is important to know the transport properties and the charge-carrier mechanism to understand the electrical conductivity associated with its wide-spread application in fuel cell devices. Introducing aliovalent dopants in the A- and B-site of these perovskites are quite interesting that introduces vacancies in the crystal structure and favours conductivity in these materials[195,198]. The present work focuses on multi-element doping in the A- and B-site of $Ba(Y_{1/2}Nb_{1/2})O_3$, on their structural, morphology and electrical properties. Doping of alkaline earth metals (Ca^{2+}, Sr^{2+}) in the A-site reduces the volatility of Ba atoms from the A-site causing structural distortions and is said to improve the structural stability of these perovskites. For B-site doping, transition metal Ni was used that acts as sintering aid in improving the sintering condition of these perovskite oxides.

6.2 Results and discussion

6.2.1 Structural and morphology characterization

The solid-state synthesis of simple perovskite oxides $(Ba_{1-x}A'_x)(Y_{1/2}Nb_{1/2-y-z}M'_yM''_z)O_{3-\delta}$ (A' = Sr, Ca; M' = Mg and M'' = Ni) (x = 0, 0.5; y = 0, 0.1; z = 0, 0.05, 0.1) was carried out as per procedure discussed in **section 3.1.2**. The current work focuses on developing multi-component doping in the A- and B-sites of $BaY_{0.5}Nb_{0.5}O_3$, with better physical properties and high entropy oxides. As a first step, non-stoichiometry compositions of $BaY_{0.5}Nb_{0.5}O_3$ (BYN) (x = y = z = 0), were synthesized to introduce vacancies in the system.

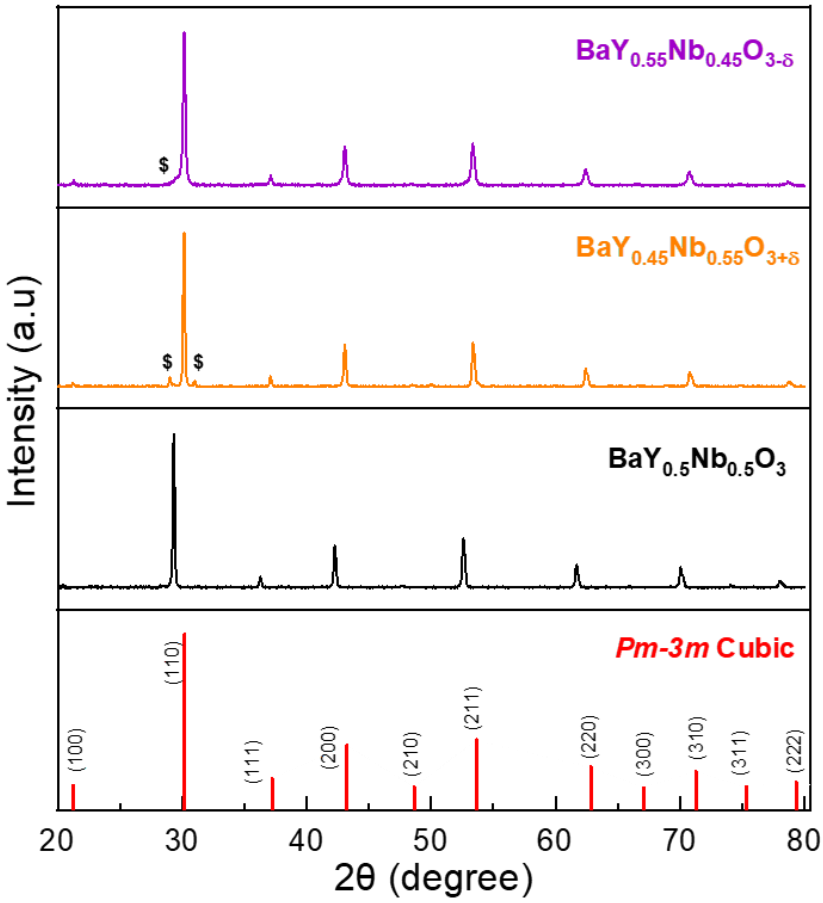

*Figure 6.1 PXRD patterns of $BaY_{0.5}Nb_{0.5}O_3$, $BaY_{0.45}Nb_{0.55}O_{3+\delta}$, and $BaY_{0.55}Nb_{0.45}O_{3-\delta}$ sintered at 1350 ˚C for 20 h in air. These patterns were indexed to $Pm\bar{3}m$ space group in a cubic crystal system. The symbol "**$**" denotes an unidentified impurity phase.*

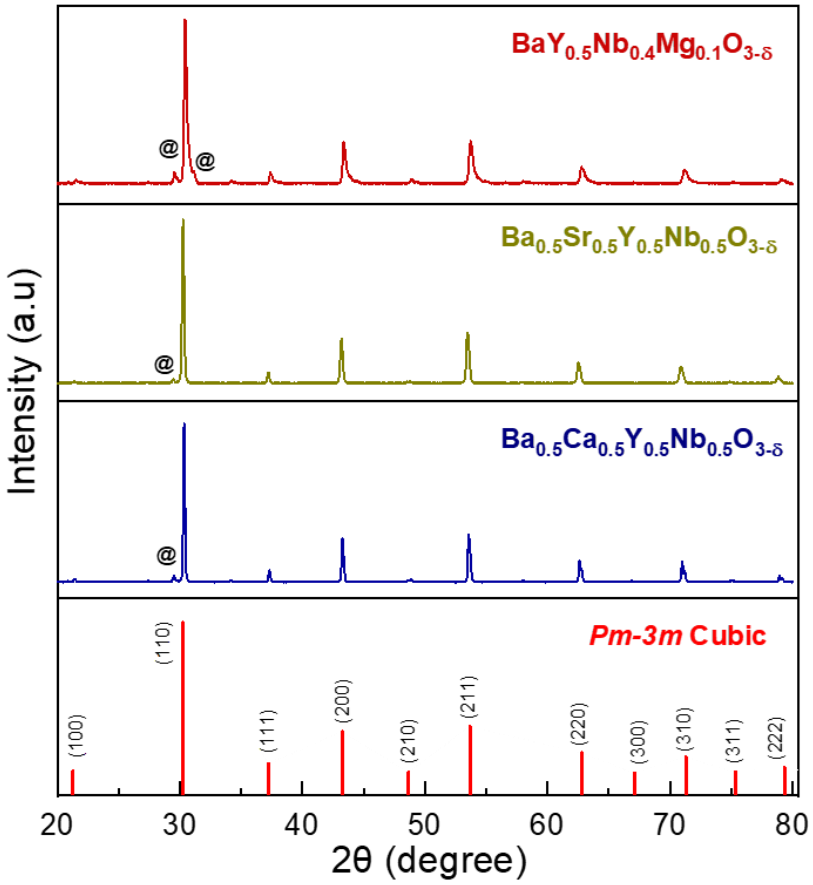

Figure 6.2 PXRD patterns of $Ba_{0.5}Ca_{0.5}Y_{0.5}Nb_{0.5}O_{3-\delta}$, $Ba_{0.5}Sr_{0.5}Y_{0.5}Nb_{0.5}O_{3-\delta}$, and $BaY_{0.5}Nb_{0.4}Mg_{0.1}O_{3-\delta}$ sintered at 1350 ˚C for 20 h in air, indexed to $Pm\bar{3}m$ space group in a cubic crystal system. The symbol "@" denotes an unidentified impurity phase.

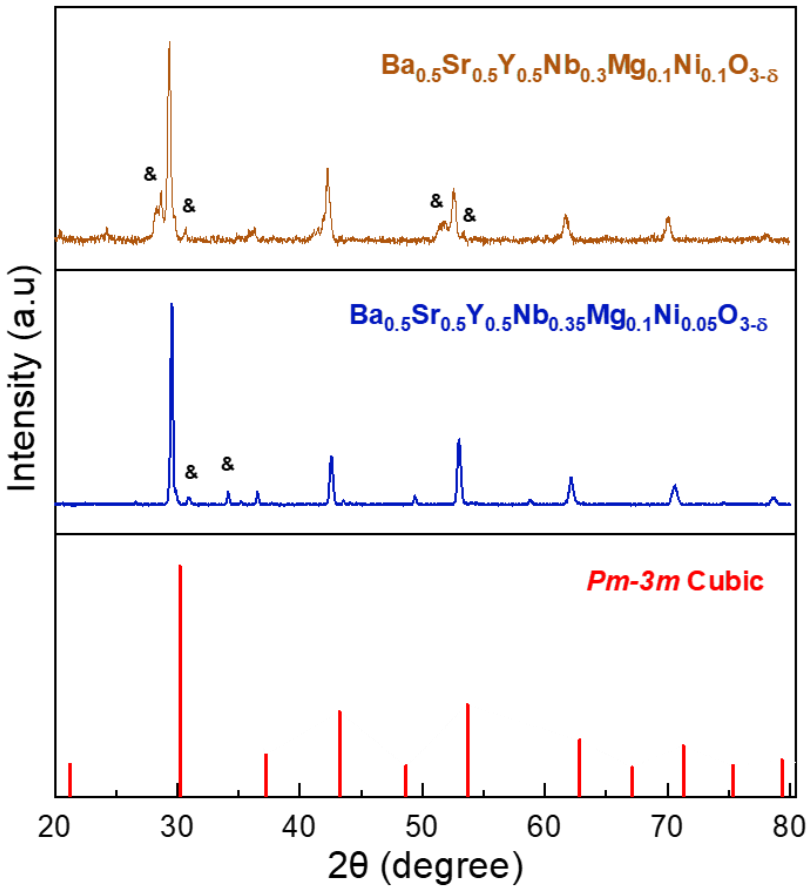

Figure 6.3 PXRD patterns of $Ba_{0.5}Ca_{0.5}Y_{0.5}Nb_{0.5}O_{3-\delta}$, $Ba_{0.5}Sr_{0.5}Y_{0.5}Nb_{0.5}O_{3-\delta}$, and $BaY_{0.5}Nb_{0.4}Mg_{0.1}O_{3-\delta}$ sintered at 1350 ˚C for 20 h in air, indexed to $Pm\bar{3}m$ space group in a cubic crystal system. The symbol "@" denotes an unidentified impurity phase.

Figure 6.1 denotes the PXRD patterns of $BaY_{0.5}Nb_{0.5}O_3$, $BaY_{0.45}Nb_{0.55}O_{3+\delta}$, and $BaY_{0.55}Nb_{0.45}O_{3-\delta}$ compositions sintered at 1350 ˚C for 20 h in air. Literature denotes that typical BYN is indexed to a cubic unit cell with $Pm\bar{3}m$ space group[199,200]; other non-stoichiometry compositions $BaY_{0.45}Nb_{0.55}O_{3+\delta}$, and $BaY_{0.55}Nb_{0.45}O_{3-\delta}$, contains few impurity peaks with small intensity due to undecomposed precursors. Further doping was explored with the compositions, $(Ba_{1-x}A'_x)(Y_{1/2}Nb_{1/2-y-z}M'_yM''_z)O_{3-\delta}$ (A' = Ca, Sr; M' = Mg; M'' = Ni) (x = 0.05; y = 0.1; z = 0). **Figure 6.2** shows the PXRD patterns of $Ba_{0.5}Ca_{0.5}Y_{0.5}Nb_{0.5}O_{3-\delta}$, $Ba_{0.5}Sr_{0.5}Y_{0.5}Nb_{0.5}O_{3-\delta}$, and $BaY_{0.5}Nb_{0.4}Mg_{0.1}O_{3-\delta}$ powders sintered at 1350 ˚C for 20 h in air. Among these, the composition

$Ba_{0.5}Sr_{0.5}Y_{0.5}Nb_{0.5}O_{3-\delta}$ consists of a less intensity impurity peak denoted by "@" compared to that of other dopants. However, all these compositions yielded brittle pellet samples which made it difficult to prepare for further electrical conductivity measurements. Thus, Mg and Ni were also doped to the B-site of $Ba_{0.5}Sr_{0.5}Y_{0.5}Nb_{0.5-y-z}Mg_yNi_zO_{3-\delta}$ (y = 0.1; z = 0.05, 0.1) whose PXRD patterns are depicted in **Figure 6.3** that shows peaks due to unidentified impurity peaks. From all the above compositions, $BaY_{0.5}Nb_{0.5}O_3$ (BYN), $Ba_{0.5}Sr_{0.5}Y_{0.5}Nb_{0.4}Mg_{0.1}O_{3-\delta}$ (BSYNM), and $Ba_{0.5}Sr_{0.5}Y_{0.5}Nb_{0.3}Mg_{0.1}Ni_{0.1}O_{3-\delta}$ (BSYNMNi0.1) were considered whose sintering conditions (temperature, duration, heating and cooling rate) and choice of precursors were modified to yield pure single phase compositions to be examined for their electrical properties.

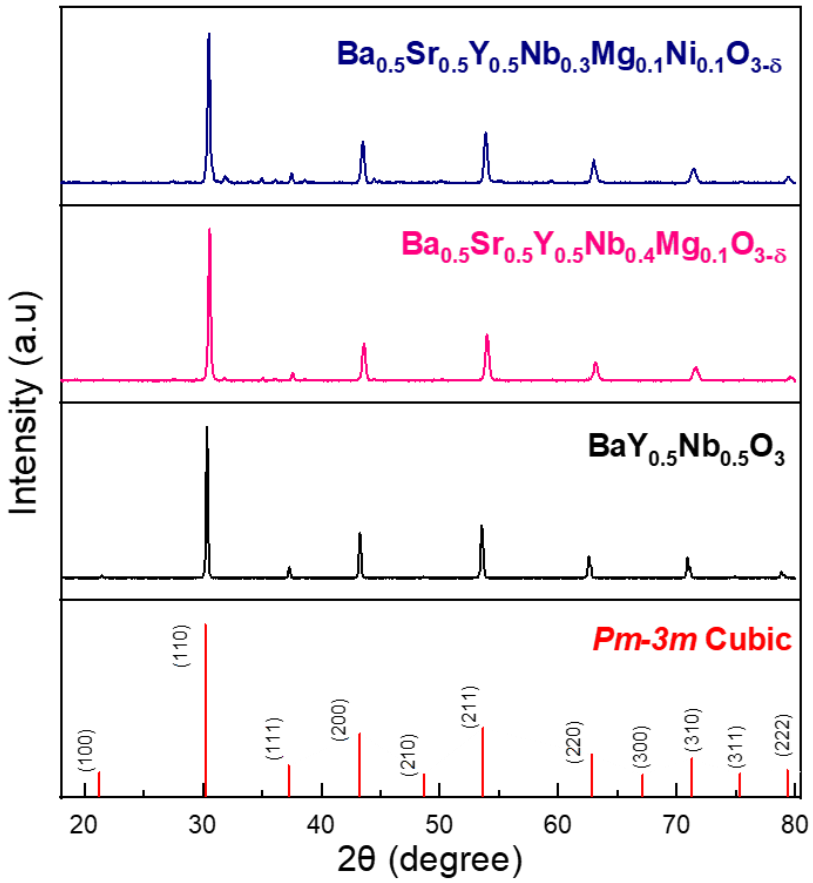

Figure 6.4 PXRD patterns of $BaY_{0.5}Nb_{0.5}O_3$, $Ba_{0.5}Sr_{0.5}Y_{0.5}Nb_{0.4}Mg_{0.1}O_{3-\delta}$ and $Ba_{0.5}Sr_{0.5}Y_{0.5}Nb_{0.3}Mg_{0.1}Ni_{0.1}O_{3-\delta}$ sintered at 1400 ˚C for 22 h in air.

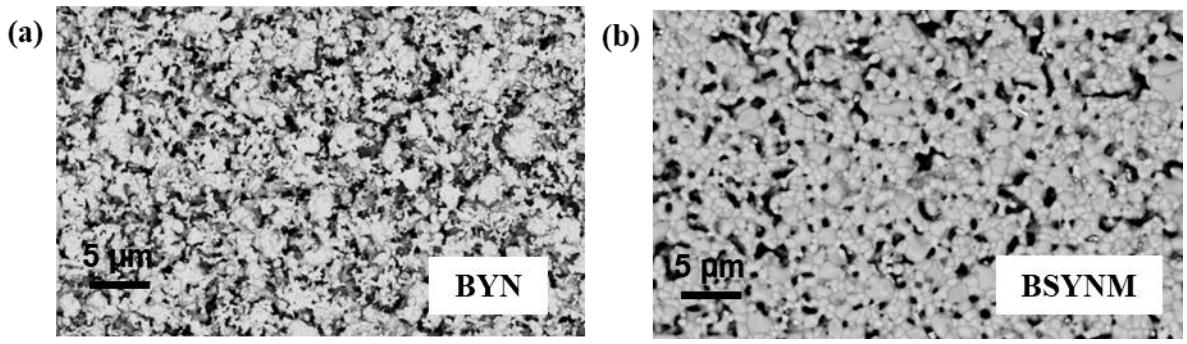

Figure 6.5 SEM images of as-prepared (a) $BaY_{0.5}Nb_{0.5}O_3$ (BYN), and (b) $Ba_{0.5}Sr_{0.5}Y_{0.5}Nb_{0.4}Mg_{0.1}O_{3-\delta}$ (BSYNM) pellets sintered at 1350 ˚C for 20 h in air. (a) shows porous morphology with high grain boundaries, and (b) shows less porosity, with lesser grain boundaries.

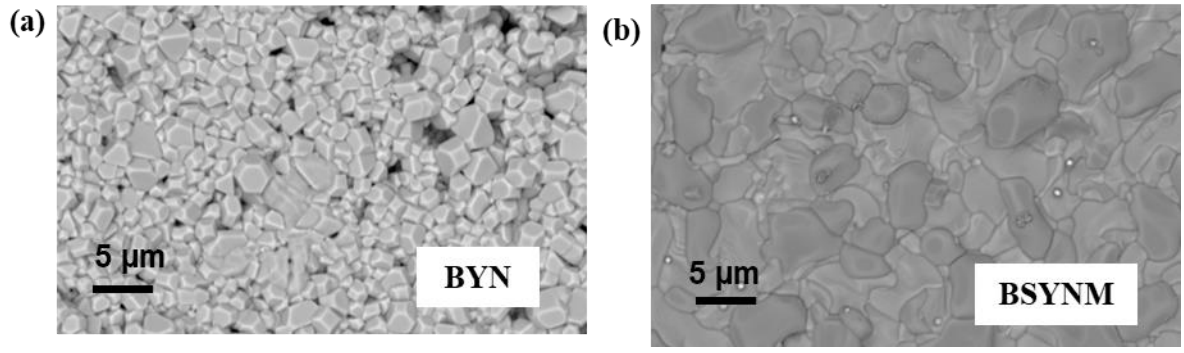

Figure 6.6 SEM images of as-prepared (a) $BaY_{0.5}Nb_{0.5}O_3$ (BYN), and (b) $Ba_{0.5}Sr_{0.5}Y_{0.5}Nb_{0.4}Mg_{0.1}O_{3-\delta}$ (BSYNM) pellets sintered at 1400 ˚C for 22 h in air. (a) shows cube-like particles with defined less grain-boundary, and (b) shows well-sintered denser particles with less/no grain boundaries.

Figure 6.4 shows the PXRD patterns of $BaY_{0.5}Nb_{0.5}O_3$, $Ba_{0.5}Sr_{0.5}Y_{0.5}Nb_{0.4}Mg_{0.1}O_{3-\delta}$ and $Ba_{0.5}Sr_{0.5}Y_{0.5}Nb_{0.3}Mg_{0.1}Ni_{0.1}O_{3-\delta}$ sintered at 1400 ˚C for 22 h in air, with purer single phase observed. To further emphasize why a higher sintering temperature is preferred, surface morphology characterization was done for pellet samples sintered between 1350 – 1400 ˚C for 20 – 22 h in air. The SEM images of pellet samples sintered at 1350 ˚C for 20 h in the air are shown in **Figure 6.5(a)** for BYN with porous morphology with high grain boundary, and **Figure 6.5(b)** for BSYNM shows less porosity, with lesser grain boundary. In comparison, **Figures 6.6(a) and**

(b) shows SEM images of BYN and BSYNM samples sintered at 1400 ˚C for 22 h in air with more cube-like particles with defined less grain-boundary and well-sintered denser particles with less/no grain boundary. The Rietveld refinement for these compositions was not carried out, which lacks information about the lattice parameters and density of these materials.

6.2.2 Chemical stability

The chemical stability of the prepared samples was studied in pure CO_2 at 600 ˚C for 72 h and in moisture (~ 90 ˚C) for 72 h. PXRD patterns shows no significant structural changes in the pattern after CO_2- and moisture treatment (**Figures 6.7(a) and (b)**) for both the samples, which denotes that the samples are not reactive in the above environment.

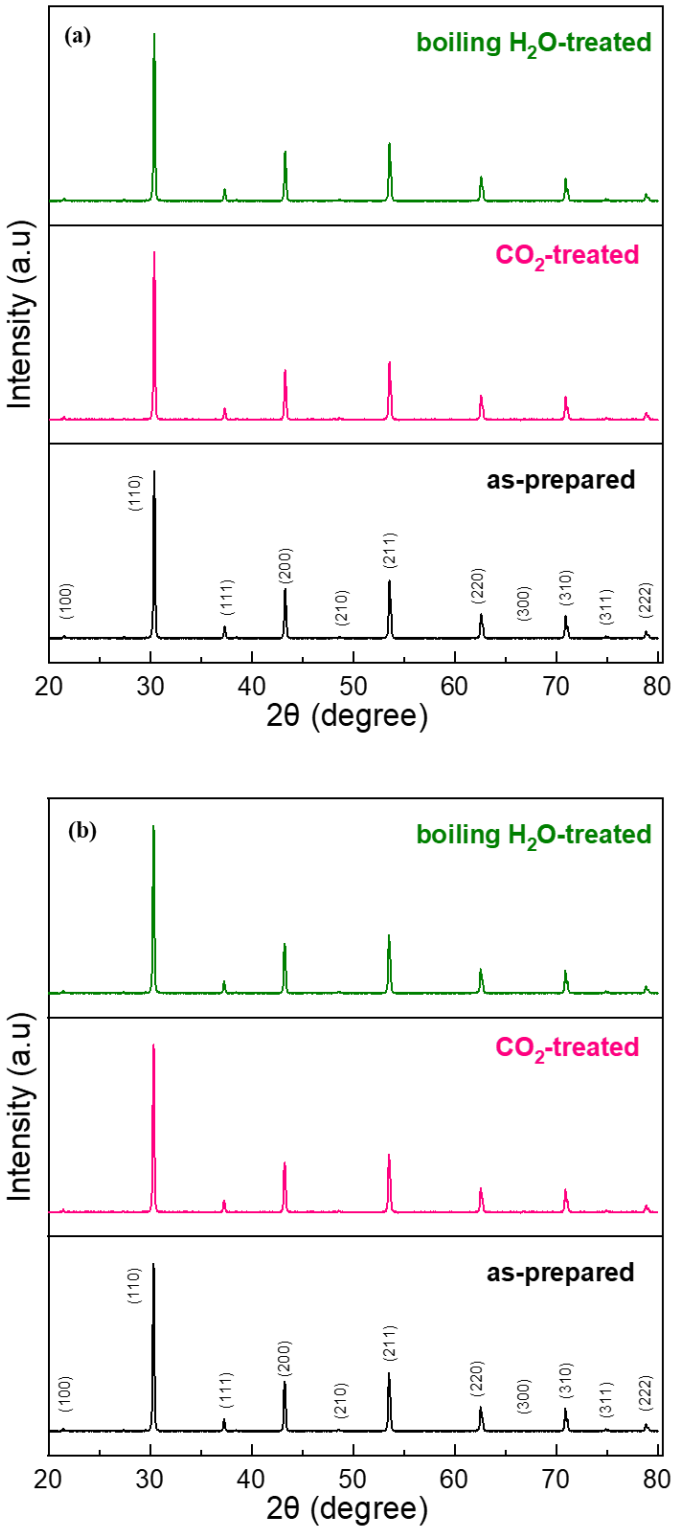

Figure 6.7 PXRD patterns of as-prepared, treated in pure CO_2 at 600 ˚C for 72 h, and moisture (~ 90 ˚C) for 72 h of (a) $BaY_{0.5}Nb_{0.5}O_3$ (BYN), and (b) $Ba_{0.5}Sr_{0.5}Y_{0.5}Nb_{0.4}Mg_{0.1}O_{3-\delta}$ (BSYNM).

Further analyses involve the identification of the respective peaks due to carbonates and hydroxyl groups from the FTIR spectra. **Figure 6.7** shows the FTIR spectra of $BaY_{0.5}Nb_{0.5}O_3$ and $Ba_{0.5}Sr_{0.5}Y_{0.5}Nb_{0.4}Mg_{0.1}O_{3-\delta}$ with no significant peaks near ~1500 cm^{-1} frequency related to the carbonate group no peak due to hydroxyl group at ~3500 cm^{-1}.

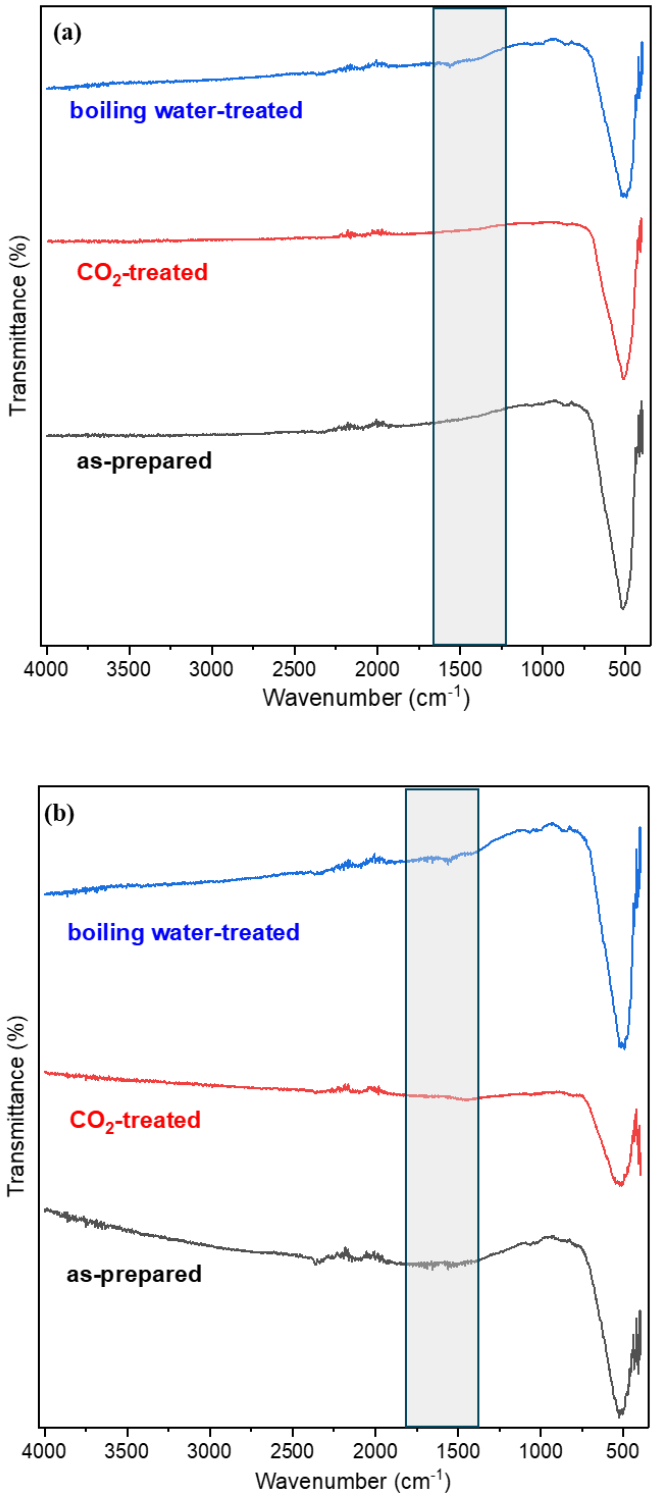

Figure 6.8 FTIR spectra of as-prepared, treated in pure CO_2 at 600 ˚C for 72 h, and in moisture (~ 90 ˚C) for 72 h of (a) $BaY_{0.5}Nb_{0.5}O_3$ (BYN), and (b) $Ba_{0.5}Sr_{0.5}Y_{0.5}Nb_{0.4}Mg_{0.1}O_{3-\delta}$ (BSYNM). The region marked in grey box shows the absence of peak due to carbonate at ~1500 cm^{-1} and hydroxyl at ~3500 cm^{-1}.

The literature survey, to the best of our knowledge, shows that no attempts were made to study the chemical stability of BYN parent compound in CO_2- and moisture-containing environments.

6.2.3 Electrical properties

The AC conductivity studies of $BaY_{0.5}Nb_{0.5}O_3$ (BYN), and $Ba_{0.5}Sr_{0.5}Y_{0.5}Nb_{0.4}Mg_{0.1}O_{3-\delta}$ (BSYNM) perovskites are discussed in this section. The schematic shown in **Figure 4.7** is adopted for these pellet samples used in electrical measurements.

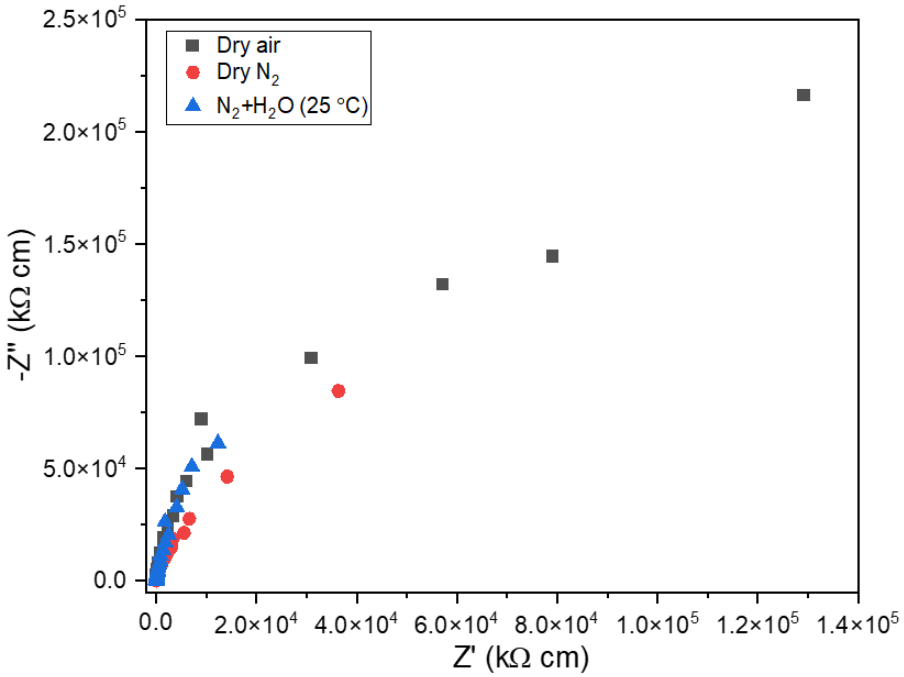

Figure 6.9 Nyquist plots of $BaY_{0.5}Nb_{0.5}O_3$ (BYN) at 400 ˚C in dry air, dry N_2 and N_2+H_2O (25 ˚C), over frequency range of 10^6 – 10^{-1} Hz and amplitude of 100 mV.

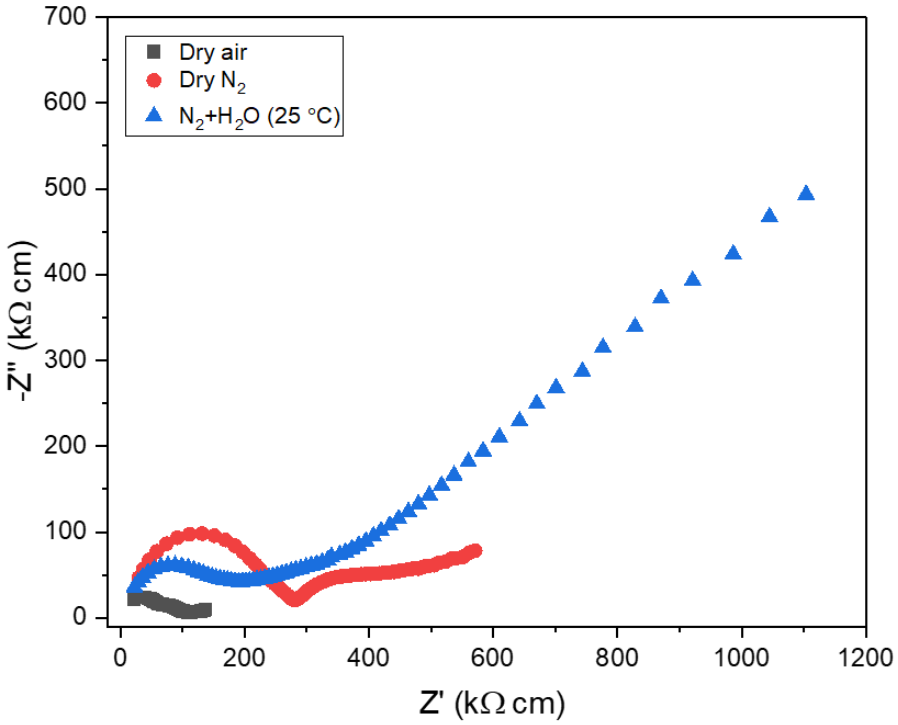

Figure 6.10 Nyquist plots of $Ba_{0.5}Sr_{0.5}Y_{0.5}Nb_{0.4}Mg_{0.1}O_{3-\delta}$ (BSYNM) at 400 ˚C in dry air, dry N_2 and N_2+H_2O (25 ˚C), over frequency range of 10^6 – 10^{-1} Hz and amplitude of 100 mV.

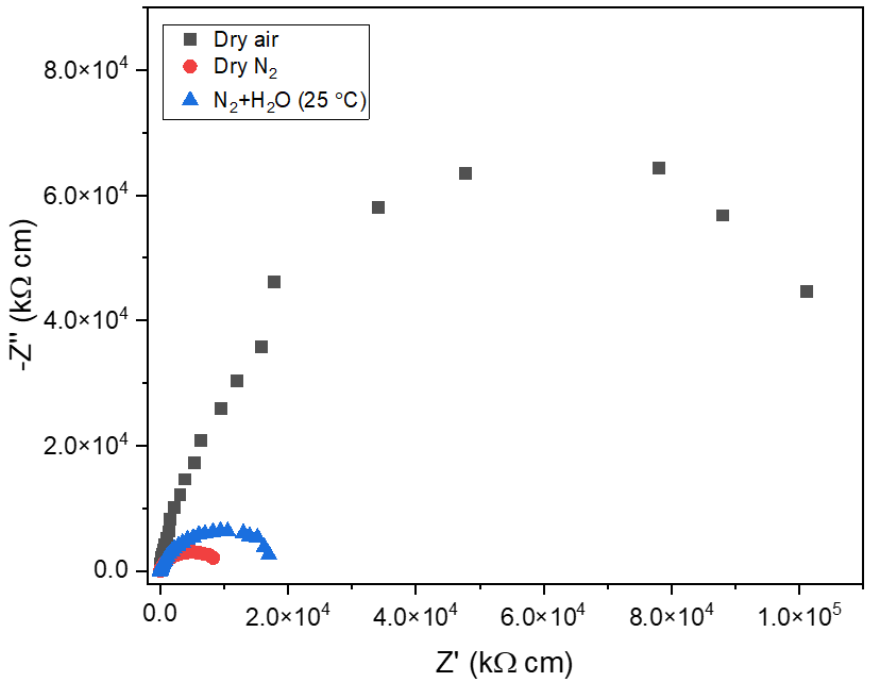

Figure 6.11 Nyquist plots of $BaY_{0.5}Nb_{0.5}O_3$ (BYN) at 600 ˚C in dry air, dry N_2 and N_2+H_2O (25 ˚C), over frequency range of 10^6 – 10^{-1} Hz and amplitude of 100 mV.

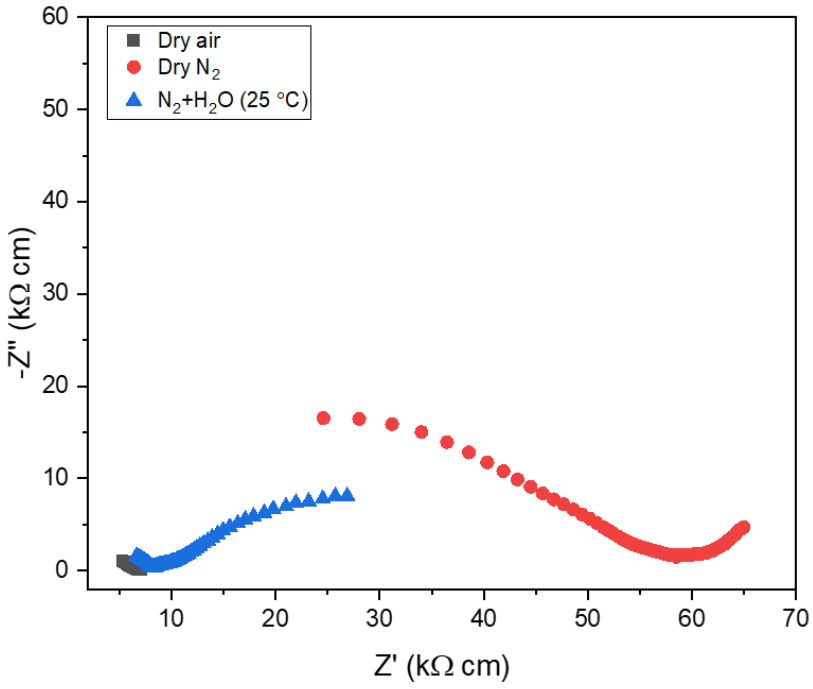

Figure 6.12 Nyquist plots of $Ba_{0.5}Sr_{0.5}Y_{0.5}Nb_{0.4}Mg_{0.1}O_{3-\delta}$ (BSYNM) at 600 ˚C in dry air, dry N_2 and N_2+H_2O (25 ˚C), over frequency range of 10^6 – 10^{-1} Hz and amplitude of 100 mV.

Figures 6.10 – 6.13 represent the Nyquist plots of $BaY_{0.5}Nb_{0.5}O_3$ and $Ba_{0.5}Sr_{0.5}Y_{0.5}Nb_{0.4}Mg_{0.1}O_{3-\delta}$ in different atmospheres. Irrespective of the atmosphere in which the impedance measurements were carried out the AC impedance spectra of $BaY_{0.5}Nb_{0.5}O_3$ (**Figure 6.10**) at 400 ˚C shows the absence of distinct semicircles between the frequency range 10^{-1}Hz to 10^6Hz which denotes their respective contributions due to bulk, grain-boundary, and electrode effects. However, the Nyquist plot at 600 ˚C (**Figure 6.12**) although it has a semicircle, the plot is scattered at a low frequency range (10 – 10^{-1} Hz) making it complex to evaluate the contributions due to different processes. This can be related to the morphology of this sample in **Figure 6.6(a)** which shows particles with the presence of grain-boundary. Conversely, the AC impedance of $Ba_{0.5}Sr_{0.5}Y_{0.5}Nb_{0.4}Mg_{0.1}O_{3-\delta}$ (**Figures 6.12 and 6.13**) at 400 ˚C and 600 ˚C shows different curves in different atmospheres, which makes it complex to elucidate the equivalent circuit and the respective bulk, grain-boundary,

and electrode effects. Furthermore, the Nyquist plot summarizes that multi-element doping has clear effects on reducing the impedance (resistance) of BYN by a magnitude of 10^{-3} kΩ cm.

6.3 Summary

The chapter summarizes the structural optimizations of multi-element doped in the A- and B-site of $BaY_{0.5}Nb_{0.5}O_3$ (BYN). The PXRD pattern reveals the crystallization of $BaY_{0.5}Nb_{0.5}O_3$ and $Ba_{0.5}Sr_{0.5}Y_{0.5}Nb_{0.4}Mg_{0.1}O_{3-\delta}$ in a simple cubic crystal system with a $Pm\bar{3}m$ space group. Although, the crystal formation was successful for these compositions, several attempts were made to modify and optimize the synthesis and sintering conditions. The surface morphology of the pellet samples shows $BaY_{0.5}Nb_{0.5}O_3$ containing more pores and grain boundaries than that of $Ba_{0.5}Sr_{0.5}Y_{0.5}Nb_{0.4}Mg_{0.1}O_{3-\delta}$, emphasizing better particles formed in doped BYN. The chemical stability of these compositions in CO_2 and moisture containing environments shows their potential to be used in devices for energy applications that are present in such operating conditions.

Chapter 7 Conclusion and future work

7.1 Conclusions

This chapter summarizes the major findings and results of the work presented in the previous three chapters.

7.1.1 Transition metal-doped double perovskite-type electrolyte $Ba_2Ca_{0.67}Nb_{1.33-x}M_xO_{6-\delta}$ (x = 0, 0.05, 0.13 and 0.26) and $Ba_2Ca_{0.67-x}M_xNb_{1.33}O_{6-\delta}$ (x = 0 and 0.13)

In this chapter, transition metal-doped double perovskite-type $Ba_2Ca_{0.67}Nb_{1.33-x}Cu_xO_{6-\delta}$ (x = 0, 0.05, 0.13 and 0.26) and $Ba_2Ca_{0.67-x}Cu_xNb_{1.33}O_{6-\delta}$ (x = 0.13) oxides have been synthesized by solid-state ball milling method. The structural and electrical properties of these materials were evaluated based on increasing Cu-doping in the B-site of the perovskite. The solid-state synthesis yields double perovskite oxides with space group $Pm\bar{3}m$ which was confirmed by the PXRD analysis. However, for high Cu- concentration fractional amount of a secondary phase in $Fm\bar{3}m$ space group was also observed. These materials also exhibited good chemical stability in CO_2- and moisture-containing mediums. The surface morphology showed the uniform distribution of particles with presence of grain-boundary that supported the conductivity values observed during impedance measurements. Among all the compositions studied, $Ba_2Ca_{0.67}Nb_{1.2}Cu_{0.13}O_{6-\delta}$ showed highest conductivity of 4.6×10^{-4} Scm^{-1} in dry air at 600 ˚C, with activation energy of 0.72 eV (500 – 750 ˚C). The conductivity seems to decrease with decreasing oxygen partial pressure and the trend in conductivity observed was in the order of air > wet N_2 > dry N_2, demonstrating that these samples mixed ionic and electronic conduction at intermediate temperature. Furthermore, the same composition had comparable conductivity in humid medium (8.8×10^{-5} Scm^{-1} in wet N_2 at 600 ˚C) is comparable to that with literature $Ba_3Ca_{1.18}Nb_{1.57}Ti_{0.15}O_{9-\delta}$, and $Ba_2(Ca_{0.79}Nb_{0.66}Ta_{0.55})O_{6-\delta}$.

7.1.2 Dielectric studies of transition metal-doped double perovskite-type $Ba_2Ca_{0.67}Nb_{1.33-x}Cu_xO_6$ (x = 0, 0.05, 0.13 and 0.26) oxides

In this chapter, the relationship between electrical and dielectric properties of Cux-BCN (x = 0, 0.05, 0.13 and 0.26) is discussed to investigate the use of these perovskites in dielectric applications. The dielectric properties were evaluated using AC Impedance spectroscopy method, over the frequency range 10^6 – 10^{-1} Hz, between 500 – 750 ˚C. Among the investigated samples, the highest dielectric constant exhibited by $Ba_2Ca_{0.67}Nb_{1.2}Cu_{0.13}O_{6-\delta}$ (x = 0.13) was 587 and dielectric loss of 2 at 10^6 Hz at 500 ˚C in air. In general, $Ba_2Ca_{0.67}Nb_{1.2}Cu_{0.13}O_{6-\delta}$ (x = 0.13) shows highest dielectric constant values in the range of ~100 – 600 and lowest dielectric loss exhibited by $Ba_2Ca_{0.67}Nb_{1.28}Cu_{0.05}O_{6-\delta}$ (x = 0.05) was ~0.3 – 0.6 at 500 ˚C in various atmospheres. The dielectric constant and dielectric loss is almost same for these compositions among various atmosphere, which is the ideal property for any dielectric material. The dielectric constant and electrical conductivity is independently varying at higher frequencies. The dielectric studies of the synthesized Cu-BCN opens a lot of opportunities in the field of dielectrics by fine tune the existing fixtures, however, the complex impedance spectra limit the further analysis of the materials into determining the relaxation time and migration energy of the charge carriers present in the material.

7.1.3 Structural and electrical properties of $Ba(Y_{1/2}Nb_{1/2})O_3$ perovskite oxides

In this chapter, we synthesized multi-element doped $BaY_{0.5}Nb_{0.5}O_3$ (BYN) perovskite oxides, where alkaline earth and rare earth elements were doped in the A- and B-site of BYN. Synthesis and structural optimizations were also carried out to come up with pure single-phase materials. Out of all the compositions synthesized, $(Ba_{1-x}A'_x)(Y_{1/2}Nb_{1/2-y-z}M'_yM''_z)O_{3-\delta}$ (A' = Sr, Ca; M' = Mg and M'' = Ni) (x = 0, 0.5; y = 0, 0.1; z = 0, 0.05, 0.1), the PXRD pattern reveals the crystallization of only $BaY_{0.5}Nb_{0.5}O_3$ and $Ba_{0.5}Sr_{0.5}Y_{0.5}Nb_{0.4}Mg_{0.1}O_{3-\delta}$ in a cubic crystal system with $Pm\bar{3}m$ space

group. Although, the crystal formation was successful for these compositions, several attempts were made to modify and optimize the synthesis and sintering conditions. The surface morphology of the pellet samples shows $BaY_{0.5}Nb_{0.5}O_3$ containing more pores and grain boundaries than that of $Ba_{0.5}Sr_{0.5}Y_{0.5}Nb_{0.4}Mg_{0.1}O_{3-\delta}$, emphasizing better particles formed in doped BYN. The chemical stability of these compositions in CO_2- and moisture-containing environment shows their potential to be used in devices for energy applications that are present in such operating conditions. However, improving the conductivity of these materials remains a challenge due to complex impedance spectra at different environments.

7.2 Future work

Based on the above results and analysis in this thesis work, following are the suggestions for future work:

- The proton conducting behaviour of the double perovskite $Ba_2Ca_{0.67}Nb_{1.33}O_6$ (BCN) was quenched/ supressed by doping transition metal Cu in the B-site of BCN. However, the highest conductivity was in the range of 10^{-3} – 10^{-4} S/cm in air at 600 ˚C, which was lesser than other transition metal-doped BCN from literature. Different transition metal ions can be doped to eliminate the presence of secondary phase for higher dopant concentration and studied for improving the proton conductivity in wet medium. Furthermore, in-situ structural analysis could be considered as future work for in-depth analysis to debate on the influence of major and minor phases on the conductivity.
- In dielectric studies of Cu-BCN, the absence of low frequency intercepts/ curves in AC impedance Nyquist plot failed in determining the relaxation time and migration energy of the charge carriers in the crystal lattice. This was due to the absence of electrode response in low frequency region which can be improved by using a different electrode (like Pt, Pd).

- The presence of secondary phases in multiple elements doped $BaY_{0.5}Nb_{0.5}O_3$ has made them unable to study their electrical properties. Trial and error methods on sintering conditions, can be adopted to improve their structural and electrical properties.

References

(1) Schoenung, J. M.; Olivetti, E. A.; Editors, G. Sustainable Development of Materials: Broadening Stakeholder Engagement. *MRS Bull.* **2023**, *48* (4), 362–367. https://doi.org/10.1557/s43577-023-00521-8.

(2) Liu, Y.; Chen, H.; Gao, J.; Li, Y.; Dave, K.; Chen, J.; Federici, M.; Perricone, G. Comparative Analysis of Non-Exhaust Airborne Particles from Electric and Internal Combustion Engine Vehicles. *J. Hazard. Mater.* **2021**, *420*, 126626. https://doi.org/10.1016/j.jhazmat.2021.126626.

(3) *Electric vehicle*. https://www.npr.org/2023/01/11/1148483758/ntsb-heavy-electric-vehicles-safety-risks.

(4) Lim, S.-R.; Kang, D.; Ogunseitan, O. A.; Schoenung, J. M. Potential Environmental Impacts from the Metals in Incandescent, Compact Fluorescent Lamp (CFL), and Light-Emitting Diode (LED) Bulbs. *Environ. Sci. Technol.* **2013**, *47* (2), 1040–1047. https://doi.org/10.1021/es302886m.

(5) Ye, Y. F.; Wang, Q.; Lu, J.; Liu, C. T.; Yang, Y. High-Entropy Alloy: Challenges and Prospects. *Mater. Today* **2016**, *19* (6), 349–362. https://doi.org/10.1016/j.mattod.2015.11.026.

(6) Miracle, D. B.; Senkov, O. N. A Critical Review of High Entropy Alloys and Related Concepts. *Acta Mater.* **2017**, *122*, 448–511. https://doi.org/10.1016/j.actamat.2016.08.081.

(7) Fu, X.; Schuh, C. A.; Olivetti, E. A. Materials Selection Considerations for High Entropy Alloys. *Scr. Mater.* **2017**, *138*, 145–150. https://doi.org/10.1016/j.scriptamat.2017.03.014.

(8) Ogunseitan, O. A. Chemicals Management Approach to Sustainable Development of Materials. *MRS Bull.* **2023**, *48* (4), 368–374. https://doi.org/10.1557/s43577-023-00518-3.

(9) Yan, Z.; Gao, Y.; Zhang, H. Materials Development and Potential Applications of Ceramics: New Opportunities and Challenges. *Appl. Sci.* **2023**, *13* (19), 10957. https://doi.org/10.3390/app131910957.

(10) Yuan, C.; Wu, H. B.; Xie, Y.; Lou, X. W. (David). Mixed Transition-Metal Oxides: Design, Synthesis, and Energy-Related Applications. *Angew. Chem. Int. Ed.* **2014**, *53* (6), 1488–1504. https://doi.org/10.1002/anie.201303971.

(11) Cao, X. Q.; Vassen, R.; Stoever, D. Ceramic Materials for Thermal Barrier Coatings. *J. Eur. Ceram. Soc.* **2004**, *24* (1), 1–10. https://doi.org/10.1016/s0955-2219(03)00129-8.

(12) Fu, Y.-P.; Chen, S.-H.; Huang, J.-J. Preparation and Characterization of Ce0.8M0.2O2−δ (M=Y, Gd, Sm, Nd, La) Solid Electrolyte Materials for Solid Oxide Fuel Cells. *Int. J. Hydrogen Energy* **2010**, *35* (2), 745–752. https://doi.org/10.1016/j.ijhydene.2009.10.093.

(13) Gild, J.; Samiee, M.; Braun, J. L.; Harrington, T.; Vega, H.; Hopkins, P. E.; Vecchio, K.; Luo, J. High-Entropy Fluorite Oxides. *J. Eur. Ceram. Soc.* **2018**, *38* (10), 3578–3584. https://doi.org/10.1016/j.jeurceramsoc.2018.04.010.

(14) Monama, G. R.; Ramohlola, K. E.; Iwuoha, E. I.; Modibane, K. D. Progress on Perovskite Materials for Energy Application. *Results Chem.* **2022**, *4*, 100321. https://doi.org/10.1016/j.rechem.2022.100321.

(15) Cramer, C. L.; Ionescu, E.; Graczyk-Zajac, M.; Nelson, A. T.; Katoh, Y.; Haslam, J. J.; Wondraczek, L.; Aguirre, T. G.; LeBlanc, S.; Wang, H.; Masoudi, M.; Tegeler, E.; Riedel, R.; Colombo, P.; Minary-Jolandan, M. Additive Manufacturing of Ceramic Materials for Energy Applications: Road Map and Opportunities. *J. Eur. Ceram. Soc.* **2022**, *42* (7), 3049–3088. https://doi.org/10.1016/j.jeurceramsoc.2022.01.058.

(16) Sun, C.; Alonso, J. A.; Bian, J. Recent Advances in Perovskite-Type Oxides for Energy Conversion and Storage Applications. *Adv. Energy Mater.* **2021**, *11* (2). https://doi.org/10.1002/aenm.202000459.

(17) Tsunoda, Y.; Sugimoto, W.; Sugahara, Y. Intercalation Behavior of N-Alkylamines into a Protonated Form of a Layered Perovskite Derived from Aurivillius Phase Bi2SrTa2O9. *Chem. Mater.* **2003**, *15* (3), 632–635. https://doi.org/10.1021/cm0200893.

(18) Bhalla, A. S.; Guo, R.; Roy, R. The Perovskite Structure – a Review of Its Role in Ceramic Science and Technology. *Mater. Res. Innov.* **2000**, *4* (1), 3–26. https://doi.org/10.1007/s100190000062.

(19) Holtmann, D.; Hannappel, A.; Schrader, J. Encyclopedia of Applied Electrochemistry. **2014**, 1268–1275. https://doi.org/10.1007/978-1-4419-6996-5_526.

(20) Atta, N. F.; Ali, S. M.; El-Ads, E. H.; Galal, A. The Electrochemistry and Determination of Some Neurotransmitters at SrPdO3 Modified Graphite Electrode. *J. Electrochem. Soc.* **2013**, *160* (7), G3144–G3151. https://doi.org/10.1149/2.022307jes.

(21) Deka, B.; Ravi, S.; Perumal, A.; Pamu, D. Ferromagnetism and Ferroelectricity in Fe Doped BaTiO3. *Phys. B: Condens. Matter* **2014**, *448*, 204–206. https://doi.org/10.1016/j.physb.2014.03.069.

(22) Perovskite Oxide for Solid Oxide Fuel Cells. *Fuel Cells Hydrogen Energy* **2009**. https://doi.org/10.1007/978-0-387-77708-5.

(23) Kreisel, J.; Glazer, A. M.; Jones, G.; Thomas, P. A.; Abello, L.; Lucazeau, G. An X-Ray Diffraction and Raman Spectroscopy Investigation of A-Site Substituted Perovskite Compounds: The (Na1-XKx)0.5Bi0.5TiO3 (0le Xle1) Solid Solution. *J. Phys.: Condens. Matter* **2000**, *12* (14), 3267. https://doi.org/10.1088/0953-8984/12/14/305.

(24) Zhu, K.; Meng, X.; Pang, P.; Qian, J.; Shen, M.; Hu, B.; Shan, H. Gastric Varices in Patients With Portal Hypertension. *J. Clin. Gastroenterol.* **2010**, *44* (5), e108–e115. https://doi.org/10.1097/mcg.0b013e3181c115c6.

(25) Liu, Y.; Nagra, A. S.; Erker, E. G.; Periaswamy, P.; Taylor, T. R.; Speck, J.; York, R. A. BaSrTiO/Sub 3/ Interdigitated Capacitors for Distributed Phase Shifter Applications. *IEEE Microw. Guid. Wave Lett.* **2000**, *10* (11), 448–450. https://doi.org/10.1109/75.888828.

(26) Haines, J.; Rouquette, J.; Bornand, V.; Pintard, M.; Papet, Ph.; Gorelli, F. A. Raman Scattering Studies at High Pressure and Low Temperature: Technique and Application to the Piezoelectric Material PbZr0.52Ti0.48O3. *J. Raman Spectrosc.* **2003**, *34* (7-8), 519–523. https://doi.org/10.1002/jrs.1009.

(27) Madhavan, B.; Ashok, A. Review on Nanoperovskites: Materials, Synthesis, and Applications for Proton and Oxide Ion Conductivity. *Ionics* **2015**, *21* (3), 601–610. https://doi.org/10.1007/s11581-014-1340-8.

(28) Kamihara, Y.; Watanabe, T.; Hirano, M.; Hosono, H. Iron-Based Layered Superconductor La[O1- x F x]FeAs (x = 0.05−0.12) with T c = 26 K. *J. Am. Chem. Soc.* **2008**, *130* (11), 3296–3297. https://doi.org/10.1021/ja800073m.

(29) Huggins, R. A. Simple Method to Determine Electronic and Ionic Components of the Conductivity in Mixed Conductors a Review. *Ionics* **2002**, *8* (3–4), 300–313. https://doi.org/10.1007/bf02376083.

(30) Khajonrit, J.; Wongpratat, U.; Kidkhunthod, P.; Pinitsoontorn, S.; Maensiri, S. Effects of Co Doping on Magnetic and Electrochemical Properties of BiFeO3 Nanoparticles. *J. Magn. Magn. Mater.* **2018**, *449*, 423–434. https://doi.org/10.1016/j.jmmm.2017.10.092.

(31) Whitfield, P. S.; Herron, N.; Guise, W. E.; Page, K.; Cheng, Y. Q.; Milas, I.; Crawford, M. K. Structures, Phase Transitions and Tricritical Behavior of the Hybrid Perovskite Methyl Ammonium Lead Iodide. *Sci. Rep.* **2016**, *6* (1), 35685. https://doi.org/10.1038/srep35685.

(32) Kessler, V. G.; Spijksma, G. I.; Seisenbaeva, G. A.; Håkansson, S.; Blank, D. H. A.; Bouwmeester, H. J. M. New Insight in the Role of Modifying Ligands in the Sol-Gel Processing of Metal Alkoxide Precursors: A Possibility to Approach New Classes of Materials. *J. Sol-Gel Sci. Technol.* **2006**, *40* (2–3), 163–179. https://doi.org/10.1007/s10971-006-9209-6.

(33) Wang, B.; Gu, S.; Ding, Y.; Chu, Y.; Zhang, Z.; Ba, X.; Zhang, Q.; Li, X. A Novel Route to Prepare LaNiO 3 Perovskite-Type Oxide Nanofibers by Electrospinning for Glucose and Hydrogen Peroxide Sensing. *Analyst* **2012**, *138* (1), 362–367. https://doi.org/10.1039/c2an35989h.

(34) Esposito, S. “Traditional” Sol-Gel Chemistry as a Powerful Tool for the Preparation of Supported Metal and Metal Oxide Catalysts. *Materials* **2019**, *12* (4), 668. https://doi.org/10.3390/ma12040668.

(35) Feinle, A.; Elsaesser, M. S.; Hüsing, N. Sol–Gel Synthesis of Monolithic Materials with Hierarchical Porosity. *Chem. Soc. Rev.* **2015**, *45* (12), 3377–3399. https://doi.org/10.1039/c5cs00710k.

(36) Shandilya, M.; Rai, R.; Singh, J. Review: Hydrothermal Technology for Smart Materials. *Adv. Appl. Ceram.* **2016**, *115* (6), 354–376. https://doi.org/10.1080/17436753.2016.1157131.

(37) Danks, A. E.; Hall, S. R.; Schnepp, Z. The Evolution of 'Sol–Gel' Chemistry as a Technique for Materials Synthesis. *Mater. Horiz.* **2015**, *3* (2), 91–112. https://doi.org/10.1039/c5mh00260e.

(38) Alammar, T.; Hamm, I.; Grasmik, V.; Wark, M.; Mudring, A.-V. Microwave-Assisted Synthesis of Perovskite SrSnO3 Nanocrystals in Ionic Liquids for Photocatalytic Applications. *Inorg. Chem.* **2017**, *56* (12), 6920–6932. https://doi.org/10.1021/acs.inorgchem.7b00279.

(39) Xia, Y.; Liu, J.; Xia, L.; Lu, Q.; Bao, D. Synthesis and Catalytic Performance for Toluene Combustion of High Surface Area Mesoporous Nickel Oxide. *Sci. Sin. Chim.* **2016**, *46* (2), 215–221. https://doi.org/10.1360/n032015-00090.

(40) YU, L.; CHEN, Y.; GU, Q.; TIAN, D.; LU, X.; MENG, G.; LIN, B. Layered Perovskite Oxide Y0.8Ca0.2BaCoFeO5+δ as a Novel Cathode Material for Intermediate-Temperature Solid Oxide Fuel Cells. *J. Rare Earths* **2015**, *33* (5), 519–523. https://doi.org/10.1016/s1002-0721(14)60450-6.

(41) Thirumalairajan, S.; Girija, K.; Ganesh, V.; Mangalaraj, D.; Viswanathan, C.; Ponpandian, N. Novel Synthesis of LaFeO3 Nanostructure Dendrites: A Systematic Investigation of Growth Mechanism, Properties, and Biosensing for Highly Selective Determination of Neurotransmitter Compounds. *Cryst. Growth Des.* **2013**, *13* (1), 291–302. https://doi.org/10.1021/cg3014305.

(42) Kumar, P.; Chand, P. Structural, Electric Transport Response and Electro -Strain - Polarization Effect in La and Ni Modified Bismuth Ferrite Nanostructures. *J. Alloy. Compd.* **2018**, *748*, 504–514. https://doi.org/10.1016/j.jallcom.2018.03.210.

(43) Li, Q.; Thangadurai, V. Synthesis, Structure and Electrical Properties of Mo-doped CeO2– Materials for SOFCs. *Fuel Cells* **2009**, *9* (5), 684–698. https://doi.org/10.1002/fuce.200900044.

(44) Taylor, J.; Zhang, K.; Wang, D. Sorghum and Millets. **2019**, 393–420. https://doi.org/10.1016/b978-0-12-811527-5.00013-7.

(45) Jia, F.-F.; Zhong, H.; Zhang, W.-G.; Li, X.-R.; Wang, G.-Y.; Song, J.; Cheng, Z.-P.; Yin, J.-Z.; Guo, L.-P. A Novel Nonenzymatic ECL Glucose Sensor Based on Perovskite LaTiO3-Ag0.1 Nanomaterials. *Sens. Actuators B: Chem.* **2015**, *212*, 174–182. https://doi.org/10.1016/j.snb.2015.02.011.

(46) Jin, C.; Cao, X.; Lu, F.; Yang, Z.; Yang, R. Electrochemical Study of Ba0.5Sr0.5Co0.8Fe0.2O3 Perovskite as Bifunctional Catalyst in Alkaline Media. *Int. J. Hydrogen Energy* **2013**, *38* (25), 10389–10393. https://doi.org/10.1016/j.ijhydene.2013.06.047.

(47) Bao, X.; Wang, Y.; Zhu, Q.; Wang, N.; Zhu, D.; Wang, J.; Yang, A.; Yang, R. Efficient Planar Perovskite Solar Cells with Large Fill Factor and Excellent Stability. *J. Power Sources* **2015**, *297*, 53–58. https://doi.org/10.1016/j.jpowsour.2015.07.081.

(48) Assirey, E. A. R. Perovskite Synthesis, Properties and Their Related Biochemical and Industrial Application. *Saudi Pharm. J.* **2019**, *27* (6), 817–829. https://doi.org/10.1016/j.jsps.2019.05.003.

(49) King, G.; Woodward, P. M. Cation Ordering in Perovskites. *J. Mater. Chem.* **2010**, *20* (28), 5785–5796. https://doi.org/10.1039/b926757c.

(50) Goldschmidt, V. M. Die Gesetze Der Krystallochemie. *Naturwissenschaften* **1926**, *14* (21), 477–485. https://doi.org/10.1007/bf01507527.

(51) Woodward, P. M. Octahedral Tilting in Perovskites. I. Geometrical Considerations. *Acta Crystallogr. Sect. B* **1997**, *53* (1), 32–43. https://doi.org/10.1107/s0108768196010713.

(52) Howard, C. J.; Stokes, H. T. Group-Theoretical Analysis of Octahedral Tilting in Perovskites. *Acta Crystallogr. Sect. B* **1998**, *54* (6), 782–789. https://doi.org/10.1107/s0108768198004200.

(53) Glazer, A. M. The Classification of Tilted Octahedra in Perovskites. *Acta Crystallogr. Sect. B* **1972**, *28* (11), 3384–3392. https://doi.org/10.1107/s0567740872007976.

(54) *Goldschmidt's tolerance factor*. http://www.ccp14.ac.uk/ccp/web-mirrors/pki/uni/pki/members/schinzer/stru_chem/perov/di_gold.html.

(55) Ramadass, N. ABO3-Type Oxides—Their Structure and Properties—A Bird's Eye View. *Mater. Sci. Eng.* **1978**, *36* (2), 231–239. https://doi.org/10.1016/0025-5416(78)90076-9.

(56) Anderson, M. T.; Greenwood, K. B.; Taylor, G. A.; Poeppelmeier, K. R. B-Cation Arrangements in Double Perovskites. *Prog. Solid State Chem.* **1993**, *22* (3), 197–233. https://doi.org/10.1016/0079-6786(93)90004-b.

(57) Lufaso, M. W.; Barnes, P. W.; Woodward, P. M. Structure Prediction of Ordered and Disordered Multiple Octahedral Cation Perovskites Using SPuDS. *Acta Crystallogr. Sect. B* **2006**, *62* (3), 397–410. https://doi.org/10.1107/s010876810600262x.

(58) King, G.; Woodward, P. M. Cation Ordering in Perovskites. *J. Mater. Chem.* **2010**, *20* (28), 5785–5796. https://doi.org/10.1039/b926757c.

(59) Karuppiah, K.; Ashok, A. Review on Proton and Oxide Ion Conducting Perovskite Materials for SOFC Applications. *Nanomater. Energy* **2019**, *8* (1), 1–8. https://doi.org/10.1680/jnaen.18.00004.

(60) Sun, C.; Alonso, J. A.; Bian, J. Recent Advances in Perovskite-Type Oxides for Energy Conversion and Storage Applications. *Adv. Energy Mater.* **2021**, *11* (2). https://doi.org/10.1002/aenm.202000459.

(61) Steele, B. C. H. Oxygen Ion Conductors and Their Technological Applications. *Mater. Sci. Eng.: B* **1992**, *13* (2), 79–87. https://doi.org/10.1016/0921-5107(92)90146-z.

(62) Cosimo, R. D.; Burrington, J. D.; Grasselli, R. K. Oxidative Dehydrodimerization of Propylene over a Bi2O3□La2O2 Oxide Ion-Conductive Catalyst. *J. Catal.* **1986**, *102* (1), 234–239. https://doi.org/10.1016/0021-9517(86)90157-0.

(63) Kendall, K. R.; Navas, C.; Thomas, J. K.; Loye, H.-C. zur. Recent Developments in Perovskite-Based Oxide Ion Conductors. *Solid State Ion.* **1995**, *82* (3–4), 215–223. https://doi.org/10.1016/0167-2738(95)00207-4.

(64) Coates, R. V.; McMillan, J. W. Oxygen Deficiency in Perovskite-type Compounds of Calcium. *J. Appl. Chem.* **1964**, *14* (8), 346–350. https://doi.org/10.1002/jctb.5010140806.

(65) Iwahara, H.; Esaka, T.; Mangahara, T. Mixed Conduction and Oxygen Permeation in the Substituted Oxides for CaTiO3. *J. Appl. Electrochem.* **1988**, *18* (2), 173–177. https://doi.org/10.1007/bf01009258.

(66) Betz, G.; Tributsch, H. Energy Conversion and Storage Using Insertion Materials. *Prog. Solid State Chem.* **1985**, *16* (4), 195–290. https://doi.org/10.1016/0079-6786(85)90005-6.

(67) Yang, L.; Wang, S.; Blinn, K.; Liu, M.; Liu, Z.; Cheng, Z.; Liu, M. Enhanced Sulfur and Coking Tolerance of a Mixed Ion Conductor for SOFCs: BaZr0.1Ce0.7Y0.2–XYbxO3–δ. *Science* **2009**, *326* (5949), 126–129. https://doi.org/10.1126/science.1174811.

(68) Lee, D.; Lee, I.; Jeon, Y.; Song, R. Characterization of Scandia Stabilized Zirconia Prepared by Glycine Nitrate Process and Its Performance as the Electrolyte for IT-SOFC. *Solid State Ion.* **2005**, *176* (11–12), 1021–1025. https://doi.org/10.1016/j.ssi.2005.01.004.

(69) Pelosato, R.; Cristiani, C.; Dotelli, G.; Latorrata, S.; Ruffo, R.; Zampori, L. Co-Precipitation in Aqueous Medium of La0.8Sr0.2Ga0.8Mg0.2O3−δ via Inorganic Precursors. *J. Power Sources* **2010**, *195* (24), 8116–8123. https://doi.org/10.1016/j.jpowsour.2010.07.046.

(70) Fabbri, E.; Pergolesi, D.; Traversa, E. Materials Challenges toward Proton -Conducting Oxide Fuel Cells : A Critical Review. *Chem. Soc. Rev.* **2010**, *39* (11), 4355–4369. https://doi.org/10.1039/b902343g.

(71) Souza, E. C. C. de; Muccillo, R. Properties and Applications of Perovskite Proton Conductors. *Mater. Res.* **2010**, *13* (3), 385–394. https://doi.org/10.1590/s1516-14392010000300018.

(72) Iwahara, H.; Esaka, T.; Uchida, H.; Maeda, N. Proton Conduction in Sintered Oxides and Its Application to Steam Electrolysis for Hydrogen Production. *Solid State Ion.* **1981**, *3*, 359–363. https://doi.org/10.1016/0167-2738(81)90113-2.

(73) Slade, R. C. T.; Singh, N. The Perovskite-Type Proton-Conducting Solid Electrolyte BaCe0.90Y0.10O3−α in High Temperature Electrochemical Cells. *Solid State Ion.* **1993**, *61* (1–3), 111–114. https://doi.org/10.1016/0167-2738(93)90342-z.

(74) Feng, M.; Goodenough, J. B. Ionic Conduction of Ba3Y4O9. *Solid State Ion.* **1994**, *68* (3–4), 269–277. https://doi.org/10.1016/0167-2738(94)90185-6.

(75) Yajima, T.; Kazeoka, H.; Yogo, T.; Iwahara, H. Proton Conduction in Sintered Oxides Based on CaZrO3. *Solid State Ion.* **1991**, *47* (3–4), 271–275. https://doi.org/10.1016/0167-2738(91)90249-b.

(76) Iwahara, H.; Yajima, T.; Hibino, T.; Ozaki, K.; Suzuki, H. Protonic Conduction in Calcium, Strontium and Barium Zirconates. *Solid State Ion.* **1993**, *61* (1–3), 65–69. https://doi.org/10.1016/0167-2738(93)90335-z.

(77) Bonano, N.; Ellis, B.; Mahmood, M. N. Construction and Operation of Fuel Cells Based on the Solid Electrolyte BaCeO3:Gd. *Solid State Ion.* **1991**, *44* (3–4), 305–311. https://doi.org/10.1016/0167-2738(91)90023-5.

(78) Taniguchi, N.; Hatoh, K.; Niikura, J.; Gamo, T.; Iwahara, H. Proton Conductive Properties of Gadolinium-Doped Barium Cerates at High Temperatures. *Solid State Ion.* **1992**, *53*, 998–1003. https://doi.org/10.1016/0167-2738(92)90283-u.

(79) Reichmann, M.; Geffroy, P.-M.; Fouletier, J.; Richet, N.; Chartier, T. Effect of Cation Substitution in the A Site on the Oxygen Semi-Permeation Flux in La0.5A0.5Fe0.7Ga0.3O3−δ and La0.5A0.5Fe0.7Co0.3O3−δ Dense Perovskite Membranes with A = Ca, Sr and Ba (Part I). *J. Power Sources* **2014**, *261*, 175–183. https://doi.org/10.1016/j.jpowsour.2014.03.074.

(80) Nowick, A. S.; Du, Y.; Liang, K. C. Some Factors That Determine Proton Conductivity in Nonstoichiometric Complex Perovskites. *Solid State Ion.* **1999**, *125* (1–4), 303–311. https://doi.org/10.1016/s0167-2738(99)00189-7.

(81) Liang, K. C.; Du, Y.; Nowick, A. S. Fast High-Temperature Proton Transport in Nonstoichiometric Mixed Perovskites. *Solid State Ion.* **1994**, *69* (2), 117–120. https://doi.org/10.1016/0167-2738(94)90399-9.

(82) Oikawa, I.; Takamura, H. Correlation among Oxygen Vacancies, Protonic Defects, and the Acceptor Dopant in Sc-Doped BaZrO3 Studied by 45Sc Nuclear Magnetic Resonance. *Chem. Mater.* **2015**, *27* (19), 6660–6667. https://doi.org/10.1021/acs.chemmater.5b02441.

(83) Tuller, H. L. Semiconduction and Mixed Ionic-Electronic Conduction in Nonstoichiometric Oxides: Impact and Control. *Solid State Ion.* **1997**, *94* (1–4), 63–74. https://doi.org/10.1016/s0167-2738(96)00585-1.

(84) Yokota, I. On the Theory of Mixed Conduction with Special Reference to Conduction in Silver Sulfide Group Semiconductors. *J. Phys. Soc. Jpn.* **1961**, *16* (11), 2213–2223. https://doi.org/10.1143/jpsj.16.2213.

(85) Nilges, T.; Lange, S.; Bawohl, M.; Deckwart, J. M.; Janssen, M.; Wiemhöfer, H.-D.; Decourt, R.; Chevalier, B.; Vannahme, J.; Eckert, H.; Weihrich, R. Reversible Switching between P- and n-Type Conduction in the Semiconductor Ag10Te4Br3. *Nat. Mater.* **2009**, *8* (2), 101–108. https://doi.org/10.1038/nmat2358.

(86) Schmalzried, H. Point Defects in Ternary Ionic Crystals. *Prog. Solid State Chem.* **1965**, *2*, 265–303. https://doi.org/10.1016/0079-6786(65)90009-9.

(87) Weppner, W. Electrochemical Transient Investigations of the Diffusion and Concentration of Electrons in Yttria Stabilized Zirconia-Solid Electrolytes. *Z. für Naturforsch. A* **1976**, *31* (11), 1336–1343. https://doi.org/10.1515/zna-1976-1112.

(88) Teraoka, Y.; Zhang, H.-M.; Furukawa, S.; Yamazoe, N. OXYGEN PERMEATION THROUGH PEROVSKITE-TYPE OXIDES. *Chem. Lett.* **2006**, *14* (11), 1743–1746. https://doi.org/10.1246/cl.1985.1743.

(89) Iwahara, H. Oxide-Ionic and Protonic Conductors Based on Perovskite-Type Oxides and Their Possible Applications. *Solid State Ion.* **1992**, *52* (1–3), 99–104. https://doi.org/10.1016/0167-2738(92)90095-7.

(90) Tarutina, L. R.; Vdovin, G. K.; Lyagaeva, J. G.; Medvedev, D. A. BaCe0.7–XZr0.2Y0.1FexO3–δ Derived from Proton-Conducting Electrolytes: A Way of Designing Chemically Compatible Cathodes for Solid Oxide Fuel Cells. *J. Alloy. Compd.* **2020**, *831*, 154895. https://doi.org/10.1016/j.jallcom.2020.154895.

(91) Amsif, M.; Marrero-Lopez, D.; Ruiz-Morales, J. C.; Savvin, S. N.; Gabás, M.; Nunez, P. Influence of Rare-Earth Doping on the Microstructure and Conductivity of BaCe0.9Ln0.1O3−δ Proton Conductors. *J. Power Sources* **2011**, *196* (7), 3461–3469. https://doi.org/10.1016/j.jpowsour.2010.11.120.

(92) Azad, A. K.; Irvine, J. T. S. Synthesis, Chemical Stability and Proton Conductivity of the Perovksites Ba(Ce,Zr)1−x Scx O3−δ. *Solid State Ion.* **2007**, *178* (7–10), 635–640. https://doi.org/10.1016/j.ssi.2007.02.004.

(93) Barison, S.; Battagliarin, M.; Cavallin, T.; Doubova, L.; Fabrizio, M.; Mortalò, C.; Boldrini, S.; Malavasi, L.; Gerbasi, R. High Conductivity and Chemical Stability of BaCe1−x−yZrxYyO3−δ Proton Conductors Prepared by a Sol–Gel Method. *J Mater Chem* **2008**, *18* (42), 5120–5128. https://doi.org/10.1039/b808344d.

(94) Nowick, A. S.; Du, Y. High-Temperature Protonic Conductors with Perovskite-Related Structures. *Solid State Ion.* **1995**, *77*, 137–146. https://doi.org/10.1016/0167-2738(94)00230-p.

(95) Yajima, T.; Iwahara, H. Studies on Behavior and Mobility of Protons in Doped Perovskite-Type Oxides: (I) in Situ Measurement of Hydrogen Concentration in SrCe0.95Yb0.05O3−α at High Temperature. *Solid State Ion.* **1992**, *50* (3–4), 281–286. https://doi.org/10.1016/0167-2738(92)90230-m.

(96) Stevenson, D. A.; Jiang, N.; Buchanan, R. M.; Henn, F. E. G. Characterization of Gd, Yb and Nd Doped Barium Cerates as Proton Conductors. *Solid State Ion.* **1993**, *62* (3–4), 279–285. https://doi.org/10.1016/0167-2738(93)90383-e.

(97) Harmer, M. P.; Chen, J.; Peng, P.; Chan, H. M.; Smyth, D. M. Control of Microchemical Ordering in Relaxor Ferroelectrics and Related Compounds. *Ferroelectrics* **1989**, *97* (1), 263–274. https://doi.org/10.1080/00150198908018100.

(98) Tamura, H.; Konoike, T.; Sakabe, Y.; Wakino, K. Improved High-Q Dielectric Resonator with Complex Perovskite Structure. *J. Am. Ceram. Soc.* **1984**, *67* (4), c59–c61. https://doi.org/10.1111/j.1151-2916.1984.tb18828.x.

(99) Bi, L.; Traversa, E. Electrical Properties of Ba3Ca1.18Nb1.82O9-δ Proton-Conducting Electrolyte Prepared by a Combustion Method. *Electrochem. Soc. Trans.* **2013**, *57* (1), 1069–1075. https://doi.org/10.1149/05701.1069ecst.

(100) Karuppiah, K.; Ashok, A. Review on Proton and Oxide Ion Conducting Perovskite Materials for SOFC Applications. *Nanomater. Energy* **2019**, *8* (1), 1–8. https://doi.org/10.1680/jnaen.18.00004.

(101) Bhella, S. S.; Thangadurai, V. Synthesis and Characterization of Carbon Dioxide and Boiling Water Stable Proton Conducting Double Perovskite-Type Metal Oxides. *J. Power Sources* **2009**, *186* (2), 311–319. https://doi.org/10.1016/j.jpowsour.2008.09.110.

(102) Bhella, S. S.; Thangadurai, V. Investigations on the Thermo-Chemical Stability and Electrical Conductivity of K-Doped Ba3−xKxCaNb2O9−δ (X=0.5, 0.75, 1, 1.25). *Solid State Ion.* **2011**, *192* (1), 229–234. https://doi.org/10.1016/j.ssi.2010.05.054.

(103) Trinh, T. T.; Thangadurai, V. Effect of Ti Substitution for Nb in Double Perovskite-Type Ba3CaNb2O9 on Chemical Stability and Electrical Conductivity. *Electrochimica Acta* **2010**, *56* (1), 227–234. https://doi.org/10.1016/j.electacta.2010.08.094.

(104) Kan, W. H.; Roushanafshar, M.; Vincent, A.; Fürstenhaupt, T.; Parvez, M.; Luo, J.; Thangadurai, V. Effect of Substitution of B-Sites by Mn, Fe and Co in Double Perovskite-Type Ba 3 CaNb 2 O 9 on Structure and Electrical Properties. *RSC Adv.* **2013**, *3* (45), 23824–23832. https://doi.org/10.1039/c3ra44429e.

(105) Wang, S.; Chen, Y.; Fang, S.; Zhang, L.; Tang, M.; An, K.; Brinkman, K. S.; Chen, F. Novel Chemically Stable Ba3Ca1.18Nb1.82–x Y x O9−δ Proton Conductor: Improved Proton Conductivity through Tailored Cation Ordering. *Chem. Mater.* **2014**, *26* (6), 2021–2029. https://doi.org/10.1021/cm403684b.

(106) Brixner, L. Preparation and Crystallographic Study of Some New Rare Earth Compounds. *J. Inorg. Nucl. Chem.* **1960**, *15* (3–4), 352–355. https://doi.org/10.1016/0022-1902(60)80064-4.

(107) Brixner, L. Preparation and Crystallographic Study of Some New Rare Earth Compounds. *J. Inorg. Nucl. Chem.* **1960**, *15* (3–4), 352–355. https://doi.org/10.1016/0022-1902(60)80064-4.

(108) Reaney, I. M.; Petzelt, J.; Voitsekhovskii, V. V.; Chu, F.; Setter, N. B -Site Order and Infrared Reflectivity in A (B ′ B ″)O3 Complex Perovskite Ceramics. *J. Appl. Phys.* **1994**, *76* (4), 2086–2092. https://doi.org/10.1063/1.357618.

(109) Saha, S.; Sinha, T. P. Structural and Dielectric Studies of BaFe0.5Nb0.5O3. *J. Phys.: Condens. Matter* **2002**, *14* (2), 249. https://doi.org/10.1088/0953-8984/14/2/311.

(110) Raevski, I. P.; Prosandeev, S. A.; Bogatin, A. S.; Malitskaya, M. A.; Jastrabik, L. High Dielectric Permittivity in AFe1/2B1/2O3 Nonferroelectric Perovskite Ceramics (A=Ba, Sr, Ca; B=Nb, Ta, Sb). *J. Appl. Phys.* **2003**, *93* (7), 4130–4136. https://doi.org/10.1063/1.1558205.

(111) Chung, C.-Y.; Chang, Y.-H.; Chen, G.-J. Effects of Lanthanum Doping on the Dielectric Properties of Ba(Fe0.5Nb0.5)O3 Ceramic. *J. Appl. Phys.* **2004**, *96* (11), 6624–6628. https://doi.org/10.1063/1.1804243.

(112) Dutta, A.; Sinha, T. P.; Pahari, B.; Sarkar, R.; Ghoshray, K.; Shannigrahi, S. Dielectric Relaxation and Electronic Structure of BaAl1/2Nb1/2O3: X-Ray Photoemission and Nuclear Magnetic Resonance Studies. *J. Phys.: Condens. Matter* **2008**, *20* (44), 445206. https://doi.org/10.1088/0953-8984/20/44/445206.

(113) Dutta, A.; Sinha, T. P. Dielectric Relaxation in Perovskite BaAl1/2Nb1/2O3. *J. Phys. Chem. Solids* **2006**, *67* (7), 1484–1491. https://doi.org/10.1016/j.jpcs.2006.02.002.

(114) Yin, J.; Zou, Z.; Ye, J. Photophysical and Photocatalytic Properties of MIn0.5Nb0.5O3 (M = Ca, Sr, and Ba). *J. Phys. Chem. B* **2003**, *107* (1), 61–65. https://doi.org/10.1021/jp026403y.

(115) Raibagkar, L. J.; Bajaj, S. B. Poling Effect on the Dielectric, Pyroelectric and Electrical Conductivity of Ferroelectric Ordered–Disordered Ba(Ni0.5Nb0.5)O3. *Solid State Ion.* **1998**, *108* (1–4), 105–108. https://doi.org/10.1016/s0167-2738(98)00026-5.

(116) Jones, F. G.; Randall, C. A.; Jang, S. J.; Shrout, T. R. Preparation and Characterization of Indium Based Complex Perovskites-Pb(In1/2Nb1/2)O3 (PIN), Ba Ba(In1/2Nb1/2)O3 (BIN), and Ba(In1/2Nb1/2)O3 (BIT). *Ferroelectr. Lett. Sect.* **1990**, *12* (3), 55–62. https://doi.org/10.1080/07315179008201117.

(117) Khalam, L. A.; Sreemoolanathan, H.; Ratheesh, R.; Mohanan, P.; Sebastian, M. T. Preparation, Characterization and Microwave Dielectric Properties of Ba(B1/2′Nb1/2)O3 [B′ = La, Pr, Nd, Sm, Eu, Gd, Tb, Dy, Ho, Y, Yb and In] Ceramics. *Mater. Sci. Eng.: B* **2004**, *107* (3), 264–270. https://doi.org/10.1016/j.mseb.2003.11.019.

(118) Dias, A.; Khalam, L. A.; Sebastian, M. T.; Paschoal, C. W. A.; Moreira, R. L. Chemical Substitution in Ba(RE1/2Nb1/2)O3 (RE = La, Nd, Sm, Gd, Tb, and Y) Microwave Ceramics and Its Influence on the Crystal Structure and Phonon Modes. *Chem. Mater.* **2006**, *18* (1), 214–220. https://doi.org/10.1021/cm051982f.

(119) Kumashiro, Y. Electric Refractory Materials. **2005**, 1–760. https://doi.org/10.1201/9780203908181-1.

(120) Dias, A.; Sá, R. G.; Moreira, R. L. Disorder-induced Symmetry Lowering in Ba(Y1/2Nb1/2)O3 Ceramics Probed by Raman Spectroscopy. *J. Raman Spectrosc.* **2008**, *39* (12), 1805–1810. https://doi.org/10.1002/jrs.2043.

(121) Dias, A.; Khalam, L. A.; Sebastian, M. T.; Paschoal, C. W. A.; Moreira, R. L. Chemical Substitution in Ba(RE1/2Nb1/2)O3 (RE = La, Nd, Sm, Gd, Tb, and Y) Microwave Ceramics and Its Influence on the Crystal Structure and Phonon Modes. *Chem. Mater.* **2006**, *18* (1), 214–220. https://doi.org/10.1021/cm051982f.

(122) Bednorz, J. G.; Müller, K. A. Possible HighTc Superconductivity in the Ba−La−Cu−O System. *Z. für Phys. B Condens. Matter* **1986**, *64* (2), 189–193. https://doi.org/10.1007/bf01303701.

(123) Rao, C. N. R. Solid-State Chemistry of High-Temperature Oxide Superconductors: The Experimental Situation. *J. Solid State Chem.* **1988**, *74* (1), 147–162. https://doi.org/10.1016/0022-4596(88)90341-6.

(124) Han, J.-T.; Zhou, J.-S.; Cheng, J.-G.; Goodenough, J. B. A New Pnictide Superconductor without Iron. *J. Am. Chem. Soc.* **2010**, *132* (3), 908–909. https://doi.org/10.1021/ja906883q.

(125) Reaney, I. M.; Iddles, D. Microwave Dielectric Ceramics for Resonators and Filters in Mobile Phone Networks. *J. Am. Ceram. Soc.* **2006**, *89* (7), 2063–2072. https://doi.org/10.1111/j.1551-2916.2006.01025.x.

(126) Bokov, A. A.; Ye, Z.-G. Recent Progress in Relaxor Ferroelectrics with Perovskite Structure. *J. Mater. Sci.* **2006**, *41* (1), 31–52. https://doi.org/10.1007/s10853-005-5915-7.

(127) Samara, G. A. The Relaxational Properties of Compositionally Disordered ABO3 Perovskites. *J. Phys.: Condens. Matter* **2003**, *15* (9), R367. https://doi.org/10.1088/0953-8984/15/9/202.

(128) Horiuchi, S.; Tokura, Y. Organic Ferroelectrics. *Nat. Mater.* **2008**, *7* (5), 357–366. https://doi.org/10.1038/nmat2137.

(129) Yang, L.; Kong, X.; Li, F.; Hao, H.; Cheng, Z.; Liu, H.; Li, J.-F.; Zhang, S. Perovskite Lead-Free Dielectrics for Energy Storage Applications. *Prog. Mater. Sci.* **2019**, *102*, 72–108. https://doi.org/10.1016/j.pmatsci.2018.12.005.

(130) *Dielectric constant values of different materials*. http://www.ydic.co.jp/english/technology/table_E.html.

(131) Bednorz, J. G.; Müller, K. A. Possible HighTc Superconductivity in the Ba−La−Cu−O System. *Z. für Phys. B Condens. Matter* **1986**, *64* (2), 189–193. https://doi.org/10.1007/bf01303701.

(132) Atamanik, E.; Thangadurai, V. Study of the Dielectric Properties in the NaNbO3 – KNbO3–In2O3 System Using AC Impedance Spectroscopy. *Mater. Res. Bull.* **2009**, *44* (4), 931–936. https://doi.org/10.1016/j.materresbull.2008.08.010.

(133) Irvine, J. T. S.; Sinclair, D. C.; West, A. R. Electroceramics: Characterization by Impedance Spectroscopy. *Adv. Mater.* **1990**, *2* (3), 132–138. https://doi.org/10.1002/adma.19900020304.

(134) Jonscher, A. K. Analysis of the Alternating Current Properties of Ionic Conductors. *J. Mater. Sci.* **1978**, *13* (3), 553–562. https://doi.org/10.1007/bf00541805.

(135) Yadav, A. K.; Gautam, C. Dielectric Behavior of Perovskite Glass Ceramics. *J. Mater. Sci.: Mater. Electron.* **2014**, *25* (12), 5165–5187. https://doi.org/10.1007/s10854-014-2311-6.

(136) Han, J.-T.; Zhou, J.-S.; Cheng, J.-G.; Goodenough, J. B. A New Pnictide Superconductor without Iron. *J. Am. Chem. Soc.* **2010**, *132* (3), 908–909. https://doi.org/10.1021/ja906883q.

(137) Kim, Y.-I.; Woodward, P. M. Crystal Structures and Dielectric Properties of Ordered Double Perovskites Containing Mg2+ and Ta5+. *J. Solid State Chem.* **2007**, *180* (10), 2798–2807. https://doi.org/10.1016/j.jssc.2007.08.003.

(138) Figueiredo, D. S.; Mattos, E. F. dos S.; Araujo, R. M. Computer Modelling of Defects in Ba2YNbO6. *J. Phys.: Conf. Ser.* **2022**, *2298* (1), 012006. https://doi.org/10.1088/1742-6596/2298/1/012006.

(139) Zhao, F.; Yue, Z.; Gui, Z.; Li, L. Preparation, Characterization and Microwave Dielectric Properties of A2BWO6 (A=Sr, Ba; B=Co, Ni, Zn) Double Perovskite Ceramics. *Jpn. J. Appl. Phys.* **2005**, *44* (11R), 8066. https://doi.org/10.1143/jjap.44.8066.

(140) Toby, B. H.; Dreele, R. B. V. GSAS-II: The Genesis of a Modern Open-Source All Purpose Crystallography Software Package. *J. Appl. Crystallogr.* **2013**, *46* (2), 544–549. https://doi.org/10.1107/s0021889813003531.

(141) Irvine, J. T. S.; Sinclair, D. C.; West, A. R. Electroceramics: Characterization by Impedance Spectroscopy. *Adv. Mater.* **1990**, *2* (3), 132–138. https://doi.org/10.1002/adma.19900020304.

(142) Norby, T. Solid-State Protonic Conductors: Principles, Properties, Progress and Prospects. *Solid State Ion.* **1999**, *125* (1–4), 1–11. https://doi.org/10.1016/s0167-2738(99)00152-6.

(143) Kreuer, K. D. Aspects of the Formation and Mobility of Protonic Charge Carriers and the Stability of Perovskite-Type Oxides. *Solid State Ion.* **1999**, *125* (1–4), 285–302. https://doi.org/10.1016/s0167-2738(99)00188-5.

(144) Brandon, N. P.; Skinner, S.; Steele, B. C. H. RECENT ADVANCES IN MATERIALS FOR FUEL CELLS. *Mater. Res.* **2003**, *33* (1), 183–213. https://doi.org/10.1146/annurev.matsci.33.022802.094122.

(145) Haile, S. M. Fuel Cell Materials and Components☆☆☆The Golden Jubilee Issue—Selected Topics in Materials Science and Engineering: Past, Present and Future, Edited by S. Suresh. *Acta Mater.* **2003**, *51* (19), 5981–6000. https://doi.org/10.1016/j.actamat.2003.08.004.

(146) Brett, D. J. L.; Atkinson, A.; Brandon, N. P.; Skinner, S. J. Intermediate Temperature Solid Oxide Fuel Cells. *Chem. Soc. Rev.* **2008**, *37* (8), 1568–1578. https://doi.org/10.1039/b612060c.

(147) Wu, Z.; Liu, M. Stability of BaCe0.8Gd0.2 O 3 in a H 2 O -Containing Atmosphere at Intermediate Temperatures. *J. Electrochem. Soc.* **1997**, *144* (6), 2170–2175. https://doi.org/10.1149/1.1837759.

(148) Matsumoto, H.; Kawasaki, Y.; Ito, N.; Enoki, M.; Ishihara, T. Relation Between Electrical Conductivity and Chemical Stability of BaCeO[Sub 3]-Based Proton Conductors with Different Trivalent Dopants. *Electrochem. Solid-State Lett.* **2007**, *10* (4), B77. https://doi.org/10.1149/1.2458743.

(149) Animitsa, I.; Norby, T.; Marion, S.; Glöckner, R.; Neiman, A. Incorporation of Water in Strontium Tantalates with Perovskite-Related Structure. *Solid State Ion.* **2001**, *145* (1–4), 357–364. https://doi.org/10.1016/s0167-2738(01)00931-6.

(150) Azad, A. K.; Irvine, J. T. S. Synthesis, Chemical Stability and Proton Conductivity of the Perovksites Ba(Ce,Zr)1−x Scx O3−δ. *Solid State Ion.* **2007**, *178* (7–10), 635–640. https://doi.org/10.1016/j.ssi.2007.02.004.

(151) Xie, K.; Yan, R.; Liu, X. Stable BaCe0.7Ti0.1Y0.2O3−δ Proton Conductor for Solid Oxide Fuel Cells. *J. Alloy. Compd.* **2009**, *479* (1–2), L40–L42. https://doi.org/10.1016/j.jallcom.2009.01.011.

(152) Yan, R.; Chen, G.; Wang, F.; Wang, Q.; Huang, W. A Novel Proton Conducting Ba0.95K0.05Ce0.6Zr0.2Gd0.16Zn0.04O3−δ for SOFC. *J. Alloy. Compd.* **2009**, *486* (1–2), L10–L12. https://doi.org/10.1016/j.jallcom.2009.06.166.

(153) Xie, K.; Yan, R.; Xu, X.; Liu, X.; Meng, G. The Chemical Stability and Conductivity of BaCe0.9−xYxNb0.1O3−σ Proton-Conductive Electrolyte for SOFC. *Mater. Res. Bull.* **2009**, *44* (7), 1474–1480. https://doi.org/10.1016/j.materresbull.2009.02.015.

(154) Xie, K.; Yan, R.; Liu, X. The Chemical Stability and Conductivity of BaCe0.9−xYxSn0.1O3−δ Solid Proton Conductor for SOFC. *J. Alloy. Compd.* **2009**, *479* (1–2), L36–L39. https://doi.org/10.1016/j.jallcom.2008.12.120.

(155) Bhella, S. S.; Thangadurai, V. Synthesis and Characterization of Carbon Dioxide and Boiling Water Stable Proton Conducting Double Perovskite-Type Metal Oxides. *J. Power Sources* **2009**, *186* (2), 311–319. https://doi.org/10.1016/j.jpowsour.2008.09.110.

(156) Trinh, T. T.; Thangadurai, V. Effect of Ti Substitution for Nb in Double Perovskite-Type Ba3CaNb2O9 on Chemical Stability and Electrical Conductivity. *Electrochimica Acta* **2010**, *56* (1), 227–234. https://doi.org/10.1016/j.electacta.2010.08.094.

(157) Kan, W. H.; Trinh, T. T.; Fürstenhaupt, T.; Thangadurai, V. Synthesis, Rietveld Refinement of Crystal Structure, Electron Diffraction, and Electrical Transport Properties of Ba2(Ca1–x–YFexNby)(Nb1–ZFez)O6–δ Double Perovskites. *Can. J. Chem.* **2011**, *89* (6), 688–696. https://doi.org/10.1139/v11-058.

(158) Kan, W. H.; Roushanafshar, M.; Vincent, A.; Fürstenhaupt, T.; Parvez, M.; Luo, J.; Thangadurai, V. Effect of Substitution of B-Sites by Mn, Fe and Co in Double Perovskite-Type Ba 3 CaNb 2 O 9 on Structure and Electrical Properties. *RSC Adv.* **2013**, *3* (45), 23824–23832. https://doi.org/10.1039/c3ra44429e.

(159) Singh, K.; Kan, W. H.; Patton, B.; Huq, A.; Thangadurai, V. Insights into B-Site Ordering in Double Perovskite-Type Ba3Ca1+x Nb2–x O9-δ ($0 \leq x \leq 0.45$): Combined Synchrotron and Neutron Diffraction and Electrical Transport Analyses. *Inorg. Chem.* **2018**, *57* (5), 2609–2619. https://doi.org/10.1021/acs.inorgchem.7b02984.

(160) Liang, K. C.; Nowick, A. S. High-Temperature Protonic Conduction in Mixed Perovskite Ceramics. *Solid State Ion.* **1993**, *61* (1–3), 77–81. https://doi.org/10.1016/0167-2738(93)90337-3.

(161) Liang, K. C.; Du, Y.; Nowick, A. S. Fast High-Temperature Proton Transport in Nonstoichiometric Mixed Perovskites. *Solid State Ion.* **1994**, *69* (2), 117–120. https://doi.org/10.1016/0167-2738(94)90399-9.

(162) Nowick, A. S.; Du, Y.; Liang, K. C. Some Factors That Determine Proton Conductivity in Nonstoichiometric Complex Perovskites. *Solid State Ion.* **1999**, *125* (1–4), 303–311. https://doi.org/10.1016/s0167-2738(99)00189-7.

(163) Krug, F.; Schober, T. The High-Temperature Proton Conductor Ba3(Ca1.18Nb1.82)O9−gd: Thermogravimetry of the Water Uptake. *Solid State Ion.* **1996**, *92* (3–4), 297–302. https://doi.org/10.1016/s0167-2738(96)00484-5.

(164) Schober, T.; Krug, F.; Schilling, W. Criteria for the Application of High Temperature Proton Conductors in SOFCs. *Solid State Ion.* **1997**, *97* (1–4), 369–373. https://doi.org/10.1016/s0167-2738(97)00028-3.

(165) Valkenberg, S.; Bohn, H. G.; Schilling, W. The Electrical Conductivity of the High Temperature Proton Conductor Ba3Ca1.18Nb1.82O9−δ. *Solid State Ion.* **1997**, *97* (1–4), 511–515. https://doi.org/10.1016/s0167-2738(97)00051-9.

(166) Irvine, J. T. S.; Corcoran, D. J. D.; Canales-Vazquez, J. Structural Studies of the Distorted Perovskite Proton Conductors Sr3Ca1+xNb2−xO9−δ. *Solid State Ion.* **2002**, *152*, 749–757. https://doi.org/10.1016/s0167-2738(02)00321-1.

(167) Schober, T.; Friedrich, J. The Mixed Perovskites BaCa(1+x)/3Nb(2−x)/3O3−x/2 (X=0…0.18): Proton Uptake. *Solid State Ion.* **2000**, *136* (1–2), 161–165. https://doi.org/10.1016/s0167-2738(00)00302-7.

(168) Wang, W.; Virkar, A. V. Estimation of the Chemical Diffusion Coefficient of H 2 O in Ba3Ca1.18Nb1.82 O (9 − δ) from Conductivity Measurements. *J. Electrochem. Soc.* **2003**, *150* (1), A92–A97. https://doi.org/10.1149/1.1526109.

(169) GALASSO, F. S. Structure, Properties and Preparation of Perovskite-Type Compounds. **1969**, 140–158. https://doi.org/10.1016/b978-0-08-012744-6.50012-4.

(170) Rodrigues, J. E. F. S.; Costa, R. C.; Pizani, P. S.; Hernandes, A. C.; Alonso, J. A. Combining Raman Spectroscopy and Synchrotron X-ray Diffraction to Unveil the Order Types in A3CaNb2O9 (A = Ba, Sr) Complex Perovskites. *J. Raman Spectrosc.* **2022**, *53* (7), 1333–1341. https://doi.org/10.1002/jrs.6366.

(171) Kan, W. H.; Lussier, J.; Bieringer, M.; Thangadurai, V. Studies on Polymorphic Sequence during the Formation of the 1:1 Ordered Perovskite-Type BaCa0.335M0.165Nb0.5O3-δ (M = Mn, Fe, Co) Using in Situ and Ex Situ Powder X-ray Diffraction. *Inorg. Chem.* **2014**, *53* (19), 10085–10093. https://doi.org/10.1021/ic501270k.

(172) Rodrigues, J. E. F. S.; Costa, R. C.; Pizani, P. S.; Hernandes, A. C.; Alonso, J. A. Combining Raman Spectroscopy and Synchrotron X-ray Diffraction to Unveil the Order Types in A3CaNb2O9 (A = Ba, Sr) Complex Perovskites. *J. Raman Spectrosc.* **2022**, *53* (7), 1333–1341. https://doi.org/10.1002/jrs.6366.

(173) Kan, W. H.; Lussier, J.; Bieringer, M.; Thangadurai, V. Studies on Polymorphic Sequence during the Formation of the 1:1 Ordered Perovskite-Type BaCa0.335M0.165Nb0.5O3-δ (M = Mn, Fe, Co) Using in Situ and Ex Situ Powder X-ray Diffraction. *Inorg. Chem.* **2014**, *53* (19), 10085–10093. https://doi.org/10.1021/ic501270k.

(174) Rodrigues, J. E. F. S.; Costa, R. C.; Pizani, P. S.; Hernandes, A. C.; Alonso, J. A. Combining Raman Spectroscopy and Synchrotron X-ray Diffraction to Unveil the Order Types in A3CaNb2O9 (A = Ba, Sr) Complex Perovskites. *J. Raman Spectrosc.* **2022**, *53* (7), 1333–1341. https://doi.org/10.1002/jrs.6366.

(175) Kannan, R.; Singh, K.; Gill, S.; Fürstenhaupt, T.; Thangadurai, V. Chemically Stable Proton Conducting Doped BaCeO3 -No More Fear to SOFC Wastes. *Sci. Rep.* **2013**, *3* (1), 2138. https://doi.org/10.1038/srep02138.

(176) Kan, W. H.; Roushanafshar, M.; Vincent, A.; Fürstenhaupt, T.; Parvez, M.; Luo, J.; Thangadurai, V. Effect of Substitution of B-Sites by Mn, Fe and Co in Double Perovskite-Type Ba 3 CaNb 2 O 9 on Structure and Electrical Properties. *RSC Adv.* **2013**, *3* (45), 23824–23832. https://doi.org/10.1039/c3ra44429e.

(177) Chinarro, E.; Jurado, J. R.; Figueiredo, F. M.; Frade, J. R. Bulk and Grain Boundary Conductivity of Ca0.97Ti1−xFexO3−δ Materials. *Solid State Ion.* **2003**, *160* (1–2), 161–168. https://doi.org/10.1016/s0167-2738(03)00151-6.

(178) Li, Q.; Thangadurai, V. Synthesis, Structure and Electrical Properties of Mo-doped CeO2– Materials for SOFCs. *Fuel Cells* **2009**, *9* (5), 684–698. https://doi.org/10.1002/fuce.200900044.

(179) Bhella, S. S.; Thangadurai, V. Dielectric Properties of Ba3−x K x CaNb2O9−δ (0.5< x <1.25) (KBCN) Double Perovskites. *Mater. Res. Bull.* **2011**, *46* (5), 668–674. https://doi.org/10.1016/j.materresbull.2011.01.026.

(180) Kreuer, K. D. Fast Proton Conductivity: A Phenomenon between the Solid and the Liquid State? *Solid State Ion.* **1997**, *94* (1–4), 55–62. https://doi.org/10.1016/s0167-2738(96)00608-x.

(181) Lanfredi, S.; Dessemond, L.; Rodrigues, A. C. M. Effect of Porosity on the Electrical Properties of Polycrystalline Sodium Niobate: I, Electrical Conductivity. *J. Am. Ceram. Soc.* **2003**, *86* (2), 291–298. https://doi.org/10.1111/j.1151-2916.2003.tb00014.x.

(182) Zhen, Y.; Li, J. Normal Sintering of (K,Na)NbO3-Based Ceramics: Influence of Sintering Temperature on Densification, Microstructure, and Electrical Properties. *J. Am. Ceram. Soc.* **2006**, *89* (12), 3669–3675. https://doi.org/10.1111/j.1551-2916.2006.01313.x.

(183) Irvine, J. T. S.; Sinclair, D. C.; West, A. R. Electroceramics: Characterization by Impedance Spectroscopy. *Adv. Mater.* **1990**, *2* (3), 132–138. https://doi.org/10.1002/adma.19900020304.

(184) Bhella, S. S.; Thangadurai, V. Synthesis and Characterization of Carbon Dioxide and Boiling Water Stable Proton Conducting Double Perovskite-Type Metal Oxides. *J. Power Sources* **2009**, *186* (2), 311–319. https://doi.org/10.1016/j.jpowsour.2008.09.110.

(185) Qasrawi, A. F.; Sahin, E. İ.; Emek, M.; Kartal, M.; Kargin, S. Structural and Dielectric Performance of the Ba(Zn1/3Nb2/3-XSbx)O3 Perovskite Ceramics. *Mater. Res. Express* **2019**, *6* (9), 095095. https://doi.org/10.1088/2053-1591/ab32d6.

(186) Narayanan, S.; Baral, A. K.; Thangadurai, V. Dielectric Characteristics of Fast Li Ion Conducting Garnet-Type Li 5+2x La 3 Nb 2−x Y x O 12 (x = 0.25, 0.5 and 0.75). *Phys. Chem. Chem. Phys.* **2016**, *18* (22), 15418–15426. https://doi.org/10.1039/c6cp02287a.

(187) Atamanik, E.; Thangadurai, V. Dielectric Properties of Ga-Doped Na0.5K0.5NbO3. *J. Phys. Chem. C* **2009**, *113* (11), 4648–4653. https://doi.org/10.1021/jp809905u.

(188) MAHATO, D. K.; DUTTA, A.; SINHA, T. P. Dielectric Relaxation in Double Perovskite Oxide, Ho2CdTiO6. *Bull. Mater. Sci.* **2011**, *34* (3), 455–462. https://doi.org/10.1007/s12034-011-0109-1.

(189) Thangadurai, V.; Pinzaru, D.; Narayanan, S.; Baral, A. K. Fast Solid-State Li Ion Conducting Garnet-Type Structure Metal Oxides for Energy Storage. *J. Phys. Chem. Lett.* **2015**, *6* (2), 292–299. https://doi.org/10.1021/jz501828v.

(190) Brixner, L. Preparation and Crystallographic Study of Some New Rare Earth Compounds. *J. Inorg. Nucl. Chem.* **1960**, *15* (3–4), 352–355. https://doi.org/10.1016/0022-1902(60)80064-4.

(191) Barnes, P. W.; Lufaso, M. W.; Woodward, P. M. Structure Determination of A2M3+TaO6 and A2M3+NbO6 Ordered Perovskites: Octahedral Tilting and Pseudosymmetry. *Acta Crystallogr. Sect. B* **2006**, *62* (3), 384–396. https://doi.org/10.1107/s0108768106002448.

(192) Wee, S. H.; Goyal, A.; Zuev, Y. L.; Cantoni, C.; Selvamanickam, V.; Specht, E. D. Formation of Self-Assembled, Double-Perovskite, Ba2YNbO6 Nanocolumns and Their Contribution to Flux-Pinning and Jc in Nb-Doped YBa2Cu3O7-δ Films. *Appl. Phys. Express* **2010**, *3* (2), 023101. https://doi.org/10.1143/apex.3.023101.

(193) Fu, A.; Pang, Q.; Yang, H.; Zhou, L. Ba2YNbO6:Mn4+-Based Red Phosphor for Warm White Light-Emitting Diodes (WLEDs): Photoluminescent and Thermal Characteristics. *Opt. Mater.* **2017**, *70*, 144–152. https://doi.org/10.1016/j.optmat.2017.05.028.

(194) Fu, A.; Pang, Q.; Yang, H.; Zhou, L. Ba2YNbO6:Mn4+-Based Red Phosphor for Warm White Light-Emitting Diodes (WLEDs): Photoluminescent and Thermal Characteristics. *Opt. Mater.* **2017**, *70*, 144–152. https://doi.org/10.1016/j.optmat.2017.05.028.

(195) Nath, K. A.; Prasad, K.; Chandra, K. P.; Kulkarni, A. R. Structural and Electrical Properties of Lead Free Ceramic: Ba(Nd 1/2 Nb 1/2)O 3. *Adv. Mater. Res.* **2013**, *2* (2), 119–131. https://doi.org/10.12989/amr.2013.2.2.119.

(196) Barón-González, A. J.; Frontera, C.; García-Muñoz, J. L.; Rivas-Murias, B.; Blasco, J. Effect of Cation Disorder on Structural, Magnetic and Dielectric Properties of La2MnCoO6

Double Perovskite. *J. Phys.: Condens. Matter* **2011**, *23* (49), 496003. https://doi.org/10.1088/0953-8984/23/49/496003.

(197) Prasad, K.; Bhagat, S.; Priyanka; AmarNath, K.; Chandra, K. P.; Kulkarni, A. R. Electrical Properties of BaY0.5Nb0.5O3 Ceramic: Impedance Spectroscopy Analysis. *Phys. B: Condens. Matter* **2010**, *405* (17), 3564–3571. https://doi.org/10.1016/j.physb.2010.05.041.

(198) Fu, W. T.; IJdo, D. J. W. New Insight into the Symmetry and the Structure of the Double Perovskites Ba2LnNbO6 (Ln=lanthanides and Y). *J. Solid State Chem.* **2006**, *179* (4), 1022–1028. https://doi.org/10.1016/j.jssc.2005.12.031.

(199) Prasad, K.; Bhagat, S.; Priyanka; AmarNath, K.; Chandra, K. P.; Kulkarni, A. R. Electrical Properties of BaY0.5Nb0.5O3 Ceramic: Impedance Spectroscopy Analysis. *Phys. B: Condens. Matter* **2010**, *405* (17), 3564–3571. https://doi.org/10.1016/j.physb.2010.05.041.

(200) Nath, K. A.; Prasad, K.; Chandra, K. P.; Kulkarni, A. R. Structural and Electrical Properties of Lead Free Ceramic: Ba(Nd 1/2 Nb 1/2)O 3. *Adv. Mater. Res.* **2013**, *2* (2), 119–131. https://doi.org/10.12989/amr.2013.2.2.119.